INFORMATION TO USERS

This material was produced from a microfilm copy of the original document. While the most advanced technological means to photograph and reproduce this document have been used, the quality is heavily dependent upon the quality of the original submitted.

The following explanation of techniques is provided to help you understand markings or patterns which may appear on this reproduction.

1. The sign or "target" for pages apparently lacking from the document photographed is "Missing Page(s)". If it was possible to obtain the missing page(s) or section, they are spliced into the film along with adjacent pages. This may have necessitated cutting thru an image and duplicating adjacent pages to insure you complete continuity.

2. When an image on the film is obliterated with a large round black mark, it is an indication that the photographer suspected that the copy may have moved during exposure and thus cause a blurred image. You will find a good image of the page in the adjacent frame.

3. When a map, drawing or chart, etc., was part of the material being photographed the photographer followed a definite method in "sectioning" the material. It is customary to begin photoing at the upper left hand corner of a large sheet and to continue photoing from left to right in equal sections with a small overlap. If necessary, sectioning is continued again – beginning below the first row and continuing on until complete.

4. The majority of users indicate that the textual content is of greatest value, however, a somewhat higher quality reproduction could be made from "photographs" if essential to the understanding of the dissertation. Silver prints of "photographs" may be ordered at additional charge by writing the Order Department, giving the catalog number, title, author and specific pages you wish reproduced.

5. PLEASE NOTE: Some pages may have indistinct print. Filmed as received.

Xerox University Microfilms
300 North Zeeb Road
Ann Arbor, Michigan 48106

Reproduced with permission of the copyright owner. Further reproduction prohibited without permission.

76-6652

MATHER, John Cromwell, 1946-
FAR INFRARED SPECTROMETRY OF THE COSMIC BACKGROUND RADIATION.

University of California, Berkeley, Ph.D., 1974
Physics, astronomy & astrophysics

Xerox University Microfilms, Ann Arbor, Michigan 48106

Reproduced with permission of the copyright owner. Further reproduction prohibited without permission.

Far Infrared Spectrometry of the Cosmic Background Radiation

By

John Cromwell Mather

A.B. (Swarthmore College) 1968

DISSERTATION

Submitted in partial satisfaction of the requirements for the degree of

DOCTOR OF PHILOSOPHY

in

Physics

in the

GRADUATE DIVISION

of the

UNIVERSITY OF CALIFORNIA, BERKELEY

Approved: Paul L. Richards

.....

John C. Lawson

Committee in Charge

.....

Reproduced with permission of the copyright owner. Further reproduction prohibited without permission.

FAR INFRARED SPECTROMETRY OF THE COSMIC BACKGROUND RADIATION

John Cromwell Mather

Inorganic Materials Research Division, Lawrence Berkeley Laboratory
and Department of Physics; University of California
Berkeley, California 94720

ABSTRACT

I describe two experiments to measure the cosmic background radiation near 1 mm wavelength. The first was a ground-based search for spectral lines, made with a Fabry-Perot interferometer and an InSb detector. The second is a measurement of the spectrum from 3 to 18 cm^{-1}, made with a balloon-borne Fourier transform spectrometer. It is a polarizing Michelson interferometer, cooled in liquid helium, and operated with a germanium bolometer. I give the theory of operation, construction details, and experimental results. The first experiment was successfully completed but the second suffered equipment malfunction on its first flight.

I describe the theory of Fourier transformations and give a new understanding of convolutional phase correction computations.

I discuss far infrared bolometer calibration procedures, and tabulate test results on nine detectors. I describe methods of improving bolometer sensitivity with immersion optics and with conductive film blackening.

Reproduced with permission of the copyright owner. Further reproduction prohibited without permission.

FAR INFRARED SPECTROMETRY OF THE
COSMIC BACKGROUND RADIATION

Contents

Abstract ii

I. Introduction 1

A. Theory of the Background Radiation 2

1. Big Bang Theory 2

2. Primeval Perturbations 3

3. Later Perturbations 5

4. Recent Perturbations 5

B. Observations 6

1. Long Wavelength Direct Observations 7

2. Short Wavelength Indirect Measurements 8

3. Short Wavelength Direct Observations 10

C. Organization of the Thesis 15

II. Ground Based Observations with a Fabry-Perot Interferometer 17

A. The Problem 17

B. Experimental Design 18

1. Theory of Fabry-Perot Interferometers 21

2. Properties of 1-d Grids 23

3. Construction and Operation of the Fabry-Perot Plates 25

4. Aligning and Testing the Etalons 29

5. Low Pass Filters 33

6. Geometrical Optics: Lenses 35

7. Conical Light Condensers 38

8. Detector Optimization 42

Reproduced with permission of the copyright owner. Further reproduction prohibited without permission.

C. Results 48

D. Conclusions from Ground-Based Observations 54

III. Balloon-Borne Spectrometry of the Cosmic Background Radiation 57

A. The Problem 57

B. Description of the Apparatus 59

1. The Instrument 59

2. Balloon-Gondola and Electronics 82

C. Spectrometer Operation 84

1. Aligning the Interferometer 85

2. Galibration 90

3. Observational Strategy 94

D. Models for Emissions into the Radiometer 97

1. Atmospheric Emissions 98

2. Measurement of Antenna Pattern 106

3. Diffraction Calculations 112

4. Emission Estimates 121

5. Window Emissions 123

6. Horn Emissions 126

7. Cone Optics and Emissions 132

E. Flight and Results 135

1. Balloon and Rigging 135

2. Launch and Trajectory of the Balloon 137

3. Instrumental Performance During Flight 138

Reproduced with permission of the copyright owner. Further reproduction prohibited without permission.

IV. Fourier Transformations 142

A. Definitions and Inversion Formulas 142

B. Sampling and Resolution 146

C. Phase Correction 150

D. Noise on Interferograms and Optimal Observing 155

V. Submillimeter Bolometers 159

A. Detector Calibration Methods 161

1. Calibrating Light Sources 161

2. Filters, Pipes and Windows 167

3. Effective Throughput 168

4. Measurement of Bolometer Characteristics 176

B. Bolometers Tested 185

1. Detectors 185

2. Methods of Observation 190

3. Discussion of Results 194

VI. Conclusions 200

Acknowledgements 201

References 202

Reproduced with permission of the copyright owner. Further reproduction prohibited without permission.

List of Figures

1. Submillimeter Fabry-Perot spectrometer 19
2. Fabry-Perot plates 26
3. Fabry-Perot alignment 30
4. Aspheric lens by Fermat's Principle 37
5. Focal length measurement 39
6. Light cone and image ball 40
7. InSb detector circuit 43
8. Observed 7.5-13 cm^{-1} sky emission 49
9. 10-14 cm^{-1} sky emission spectrum 51
10. Sky emission in the 6-9 cm^{-1} region 55
11. Balloon-borne spectrometer 60
12. Far infrared spectrometer schematic 61
13. Polarizing Michelson interferometer 68
14. Immersion optics mounting for Ge bolometer 75
15. Balloon gondola 81
16. Corner mirror alignment 86
17. Alignment of the polarizing Michelson interferometer 88
18. Spectrometer calibration 93
19. Emission of water, ozone, and a 2.7K black body 99
20. Emission of continuum sources into radiometer 100
21. Antenna measuring system 108
22. Antenna pattern 111
23. Diffraction at an edge 118
24. Horn emission simulator 129

Reproduced with permission of the copyright owner. Further reproduction prohibited without permission.

25. Horn emission simulation results 131

26. Brightness of laboratory Michelson interferometer 164

27. Detector throughput calibration 173

28. Angular response of source and detectors 175

29. Bolometer definitions 180

30. Jones' bolometer bridge 182

31. Immersion optics efficiency 193

List of Tables

I. InSb Bolometer 44

II. Transformer for Bolometer 45

III. Limits on width of Sub-Millimeter feature 53

IV. Balloon-borne system performance 62

V. Germanium bolometer 74

VI. Estimated noise in data fitting 96

VII. Fourier transforms, phase correction, and noise 143

VIII. Apodizing functions and corresponding resolution functions 149

IX. Bolometer material heat capacities at $1^{o}K$ 186

XI. Detector efficiency estimates 187

X. Detector test results 188

Reproduced with permission of the copyright owner. Further reproduction prohibited without permission.

I. INTRODUCTION

The Cosmic Background Radiation is one of the few clues we have towards understanding the early universe. This is electromagnetic radiation with a spectrum characteristic of a 2.7K black body, coming to the earth from all directions. No clear deviation from this spectrum or from perfect isotropy has yet been proven, despite many searches and some suggestive results. In this thesis, I describe two experiments undertaken to measure the background radiation in the submillimeter region, one made from the ground and one from a balloon. The former was a search for spectral features in the background, made from a mountain top with a Fabry-Perot interferometer. It was successfully completed and gave a null result, showing no features not explained by atmospheric emissions (Mather, Werner, and Richards, 1971). The second experiment is still an ongoing project; a balloon-borne measurement of the entire spectrum of the background over the range from 3 to 18 cm^{-1}. The project was initiated by Dr. Paul L. Richards in 1971. David P. Woody and I joined the project later that year and built an apparatus which we flew on its first flight on October 26, 1973. The development of this apparatus is discussed in this thesis, along with preliminary results from the unsuccessful first flight. The apparatus is being readied for a second flight by David Woody. The thesis also describes developments in detectors, detector calibration methods, and investigations in Fourier transform computation.

Reproduced with permission of the copyright owner. Further reproduction prohibited without permission.

A. Theory of the Background Radiation

1. Big Bang Theory

The Cosmic Background Radiation was predicted on very general grounds by Gamow (1948) from the Big Bang Theory of the universe. This theory is discussed at length in several introductory cosmology texts, inasmuch as it is now the only widely held theory. The books by Peebles (1971) and Sciama (1971) are physically oriented introductions, while the book by Misner, Thorne, and Wheeler (1973) is a monumental effort to clarify the mathematics of gravitation for modern students. According to this theory, the universe was once in a very hot, dense, and homogeneous state, and it has been expanding and cooling ever since. The original dense state may have had a temperature of 10^{12}K, which is hot enough that particles such as muons, pions, positrons, and neutrinos were present in great numbers. As expansion proceeded, these unstable particles decayed and some helium nuclei formed from protons and neutrons. At such a temperature, the energy density of electromagnetic radiation was much greater than that of matter. When the expansion reached a point where the temperature was about 3000K, the matter and radiation had about the same energy density. At about the same time, by coincidence, the temperature became low enough that the radiation could not keep the matter ionized. In the simplest theory, it then abruptly formed neutral atoms and the universe became transparent for thermal electromagnetic radiation. Before that time, the universe was opaque due to Thomson scattering by free electrons, so that a photon was scattered on a time scale short compared with the age of the universe. Neutral atoms, being uncharged on the whole, can only

Reproduced with permission of the copyright owner. Further reproduction prohibited without permission.

interact with photons at certain resonant frequencies, or photons energetic enough to ionize them.

The electromagnetic radiation which existed then has been preserved almost unchanged. All the photons present then are still present, but their energies have been reduced by the general expansion of the universe. At present, we observe a spectrum characteristic of a black body of only 3K instead of 3000K. All photons have their frequencies reduced by the same factor, so the black body nature of the spectrum is preserved.

To the extent to which this radiation is black body and isotropic, it is completely nonspecific as to the mechanism which produced it. Nevertheless, its very existence seems to rule out the Steady State theory of the universe, which has no obvious and natural mechanism for producing the background radiation. No other simple mechanism has yet been proposed which seens to explain the observed spectrum and isotropy except on an ad hoc basis.

The logical next step for observers is to refine the observations so that deviations from the ideal spectrum appear, or to show that the spectrum is very precisely black body. When deviations appear, they will be clues to the detailed processes which occurred in the early universe.

2. Primeval Perturbations

Many proposals have been made for processes which would distort the spectrum or produce anisotropy in the background radiation. Most would produce small variations and cannot easily be ruled out by present day observations. By the same token, they cannot produce large

Reproduced with permission of the copyright owner. Further reproduction prohibited without permission.

fluxes in narrow bandwidths. At one time, as will be described later, direct measurements from rockets and balloons seemed to require vast fluxes of submillimeter radiation. Several theoretical attempts were made to understand the measurements (Setti and Woltjer, 1970; Caroff and Petrosian, 1971; and Harrison and Kapitzky, 1972).

One especially interesting idea concerns perturbation of the primeval fireball itself, away from perfect homogeneity and isotropy. It has been proposed, for instance, that there were many Little Bangs insteady of one Big Bang, and that these occurred at different times and different places. As a variation on this idea, it is suggested that the universe contains or contained matter and antimatter in equal amounts, which have for some reason fractionated. More ordinary turbulence might have existed as well.

Peebles discusses the question of turbulence on p. 222 of his book. The analysis of galaxy formation is exceptionally difficult, and there is no consensus on whether galaxies could form from a homogeneous medium without pre-existing turbulent eddies. Peebles argues that turbulence is plausible and could lead to formation of galaxies with the presently observed masses. According to his calculations, turbulence could keep matter ionized long after radiation was insufficient to do so. Until the radiation temperature falls to 600K, Compton scattering produces a drag force on moving ionized matter which amounts to a viscosity, and which, therefore, greatly influences galaxy formation. The release of turbulent energy would be expected to perturb the radiation spectrum away from a pure blackbody, even though there could be enough electrons to maintain the isotropy of the radiation.

Reproduced with permission of the copyright owner. Further reproduction prohibited without permission.

3. Later Perturbations

Several other mechanisms proposed occur at later times. As galaxies themselves form, gravitational energy is released into optical radiation, and some may be emitted at appropriate frequencies to perturb the background radiation field. Or, as Harrison and Kapitzky show, some of the original radiation could be simply trapped in protogalaxies and not released until later. There might also be a burst of star formation, with rapid nuclear burning and great release of energy. Or quasars might have formed in great numbers, releasing huge amounts of radiation in the infrared and far infrared. Some of these objects might have been very dusty and this dust might have helped to make the radiation isotropic.

4. Recent Perturbations

Ideas concerning recent major perturbations of the background radiation are less tenable. The observed isotropy of the background radiation rules out presently visible objects as sources of any major perturbation. Our own galaxy emits copiously at wavelengths longer than 50 cm by the synchrotron emission process, but this radiation is distinctly non-isotropic. At shorter wavelengths, our galaxy could produce thermal emissions from dust particles, but the dust would have to have special properties to be invisible at other wavelengths. If dust were in the form of long needles or flat plates, or if impurity atoms in dielectric particles had appropriate resonances, then dust might emit in the millimeter region without absorbing strongly in the visible. This question is explored by Caroff, et al. (1972).

Reproduced with permission of the copyright owner. Further reproduction prohibited without permission.

Certain atomic and ionic species are also expected to radiate in the submillimeter region. Some are expected to be widespread and to emit large amounts of power. Ionized hydrogen (HII) clouds cool rapidly by their own emissions to about 10,000K, but at lower temperatures cooling is dominated by impurity atoms. This question is reviewed by Dalgarno and McCray (1972). The lowest frequency transitions are hyperfine transitions of CI at 610 and 369 microns, CII at 156, and NII at 204 microns. Higher frequency lines would be important if the sources were far away and doppler-shifted.

B. Observations

The observational situation has been summarized by several authors, including Ipavich and Lenchek (1970), Peebles (1971), Chapter V, and Thaddeus (1972). These are two classes of observations, direct and indirect. Direct observations are made with microwave radiometers, broad-band detectors, and spectrometers, operating on the ground, in airplanes, suspended from balloons, or carried in rockets or in the future in satellites. Indirect observations are made of interstellar thermometers, which to date include molecules in equilibrium with the radiation field at some frequency, and free cosmic ray electrons. The molecules have yielded a precise measurement at 2.64 mm and upper bounds at several shorter wavelengths. Cosmic ray electrons interact with the background radiation to produce X and gamma radiation. We have estimates of the intensities of both the electrons and the high energy photons, so we can deduce upper limits to the flux of background radiation photons. These constraints are discussed by R. Cowsik (1972).

Reproduced with permission of the copyright owner. Further reproduction prohibited without permission.

1. Long Wavelength Direct Observations

Direct observations of the background radiation were first made by Penzias and Wilson (1965) at a wavelength of 7.35 cm. What they saw was an excess noise contribution in their low-noise antenna, built for Telstar communications and for studying galactic synchrotron emission. This excess noise was immediately interpreted as the cosmic background radiation predicted by Gamow, by the team of Dicke, Peebles, Roll, and Wilkinson (1965). Roll and Wilkinson were at that time constructing an apparatus to search for it.

Many further measurements have been made in the eight years since the discovery. The observations are statistically analyzed by Peebles (1972). His result is that the spectrum from 21.2 cm to 8.2 mm is a black body spectrum, with a temperature of 2.69K. Even over this limited range, the spectrum deviates by 2.7 standard deviations from a straight Rayleigh-Jeans ν^2 power law, but is consistent with a black body spectrum. Ground-based observations have also been made at 3.3 mm. These results agree with the 2.69K black body and deviate by eight standard deviations from the Rayleigh-Jeans law.

The background has also been carefully analyzed for isotropy. No evidence for anistropy of the radiation field has been proven, although Conklin (1969) and Henry (1971) have measured a small effect that may be explained by the motion of the earth relative to the center of mass of the local supercluster of galaxies. This effect amounts to about one part in a thousand.

Reproduced with permission of the copyright owner. Further reproduction prohibited without permission.

2. Short Wavelength Indirect Measurements

The first observation to be made after the initial discovery of the radiation was indirect. In fact the data necessary had been observed two decades previously. It was quickly understood that the optical observations of interstellar cyanogen (CN) could be understood in terms of the background radiation. These observations were high-resolution spectra of several stars which are situated behind dust and gas clouds. The excitation temperature of CN was calculated by McKellar (1941) to be about 2.3K, from the ratio of populations of the ground state and the first rotational excited state. This temperature is, within observational precision, equal to the temperature measured by Penzias and Wilson. Calculations showed that it should be simply the radiation brightness temperature at 2.64 mm wavelength, since all other excitation processes are negligible. This idea is supported by the fact that the same temperature is observed for all clouds of CN. These transitions have been observed by several groups in succeeding years. Thaddeus (1972) has reviewed the data then existing, with the result that the radiation brightness temperature at 2.64 mm is 2.78±0.10K. The best data have been obtained by signal averaging techniques with high resolution Coudé spectrograms of ζ Ophiuchi made on the 120 in. telescope (Thaddeus, 1972). They have been further refined by even higher resolution spectra obtained with a Fabry-Perot interferometer (Hegyi, Traub, and Carleton, 1972), and by estimates of corrections for electron collisional excitation (Thaddeus, 1972).

Thaddeus points out that the Fabry-Perot instrument of Hegyi, et al. should be able to detect the weaker transition R(2) of CN, which will

Reproduced with permission of the copyright owner. Further reproduction prohibited without permission.

constitute a measurement of the microwave background at 1.32 mm. At present we have only upper limits derived from the non-observation with less sensitive devices.

It is possible to look at interstellar CN with a radio telescope as well. If the CN is in equilibrium with the radiation field at 2.64 mm, then it will be invisible at that frequency, even in directions in which it is abundant as evidenced by optical observations. Penzias, Jefferts, and Wilson (1972) have searched for this emission and found none, establishing that CN is a good interstellar thermometer.

Another interstellar molecule is H_2CO, formaldehyde. The ground rotational state of this molecule is a doublet, separated by a 6 cm transition which has been widely observed in molecular clouds. In most clouds not lying in front of hot bodies, the transition is observed in absorption against the cosmic background radiation. The molecule is being refrigerated by some mechanism. Both collisional and radiative pumping schemes have been proposed. If the brightness temperature of the background radiation has even slight irregularities, of the order of 0.2K, near 2 mm wavelength, then major effects should be seen in the 6 cm transition of formaldehyde. Such a small perturbation will be difficult to detect directly.

It is furthermore possible to measure transitions at 2 cm wavelength within the first rotational excited state of formaldehyde, separated by the 2 mm transitions from the ground level. Observations at 2 cm by Evans, Cheung, and Sloanaker (1970) on the cloud W51 imply that at 2 mm the background temperature is between 2 and 5K.

Reproduced with permission of the copyright owner. Further reproduction prohibited without permission.

Finally, there are other molecular species observed optically which are thermometers at other wavelengths. The interstellar species CN, CH and CH^+ have been observed in optical transitions from the ground state, but no transitions from higher rotational levels have been seen. The nonobservation of these transitions sets limits on the brightness temperatures at the wavelengths of 1.32, 0.559, and 0.359 mm, respectively, which are 3.38, 5.23, and 7.35K (Thaddeus, 1972).

3. Short Wavelength Direct Observations

Direct observations at short wavelengths, less than 3 mm, have been very difficult. The shortest wavelength at which ground-based measurements of the brightness temperature have been made is 3.3 mm, and even then the correction for atmospheric emission was an order of magnitude larger than the signal. Nevertheless, the spectrum at short wavelengths has the greatest theoretical interest, since it is there that deviations from a black body curve should be most pronounced. The previously suggested perturbations of the spectrum almost all involve emission of radiation from hot bodies at times after the condensation of the primeval plasma into neutral gas. At long wavelengths where the Rayleigh-Jeans limit applies, all gray or black bodies have the same frequency dependence. Only at short wavelengths can they be distinguished.

a. Early Rocket and Balloon Results. It was a very important result when the first direct measurements of the short-wavelength spectrum from 1.3 to 0.4 mm (7.7 to 24 cm^{-1}) showed a flux of 2.5×10^{-9} W/cm^2 sr, which is 40 times larger than expected from a 2.8K black body. This result was obtained in 1968 by Shivanandan, Houck and Harwit, of the Naval Research Laboratory and Cornell University,

Reproduced with permission of the copyright owner. Further reproduction prohibited without permission.

using an indium antimonide detector in a liquid helium cooled, rocket-borne telescope. These authors could find no explanation for the large flux in terms of local causes.

If this large flux were spread out uniformly over the frequency band covered by the rocket, then the brightness would be much larger than the limit set by the interstellar molecule CH at 0.56 mm. If these results were both correct, then the excess flux would have to be concentrated in a narrow frequency band, avoiding the CH transition.

Moreover, if the measured flux actually existed, it would be the major form of radiant energy in the universe, having an energy density of 6.6 eV/cm^3. For comparison, we would get only 4.5 eV/cm^3 of energy if we converted all the hydrogen now existing into helium. This figure is based on a mass density of 1.9×10^{30} g/cm^3, 60% hydrogen. This is 1/10 of the mass density required to close (gravitationally bind) the universe, with an assumed Hubble expansion constant of 100 km/sec/Mpc. We would have to conclude that the major function of the universe is to produce submillimeter radiation. Theoretical attempts to explain this radiation have thus met with severe difficulties. Caroff and Petrosian (1971) have considered extragalactic sources, and Wagoner (1969) has considered galactic sources. Local galactic sources are ruled out by the observed isotropy of the excess radiation, except for very special cases.

The existence of this large flux of radiation was not immediately plausible. However, the importance of such a discovery would be great, if it were true. The Cornell telescope was flown again with various changes to investigate possible errors (Houck and Harwit, 1969;

Reproduced with permission of the copyright owner. Further reproduction prohibited without permission.

Pipher et al., 1971). In 1971 the apparent excess flux had been reduced to half the previous value, but was still above the limit set by interstellar CH.

Balloon-borne observations were initiated by Muehlner and Weiss (1970) of MIT. Their first observations supported the rocket results of large excess fluxes. They used a series of low-pass filters cutting off at 10, 12 and 20 cm^{-1}. The excess flux appeared to be localized between 10 and 12 cm^{-1}.

b. Ground Based Searches for Lines. The possibility that there might be a line emission spectrum superposed on the 2.7K black body curve stimulated several searches with ground-based spectrometers, and later with aircraft-borne devices. Beery et al. (1971) used a large telescope on Mauna Kea with a standard Block Engineering Fourier transform spectrometer, and a He^3-cooled germanium bolometer as detector. They observed the transmission of the atmosphere using the sun as a source at several zenith angles, and they also observed the emission of the sky alone. Their results showed a spectral line at 11.7 cm^{-1} of sufficient magnitude to account for the rocket and balloon observations, providing it originated at an altitude of 40 km or more.

The second ground-based search for lines was made by John C. Mather, Michael W. Werner, and Paul L. Richards of the University of California, Berkeley, and the Lawrence Berkeley Laboratory. This search is described in detail in Chapter II of this thesis. We used a Fabry-Perot interferometer with an InSb detector, and observed from Barcroft Station on White Mountain, CA (12,500 ft). Our search covered the range from 6 to 14 cm^{-1}. We saw no evidence of any spectral feature that was not

Reproduced with permission of the copyright owner. Further reproduction prohibited without permission.

expected from atmospheric water or oxygen. We concluded that the large excess flux reported by Pipher et al. (1971) could not be concentrated in a single narrow line in the 10-12 cm^{-1} region as suggested by them. However, the large flux could still exist if it were in a line wider than 0.4 cm^{-1}, if it were hidden by an atmospheric line, or if it were carried by a series of smaller narrow lines.

Subsequent observations by other groups have confirmed and extended our results. Aircraft flights reported by Nolt, et al. (1972), and by Beckman, et al. (1972) carried Michelson interferometers as spectrometers. Both saw atmospheric features and nothing else. The latter were able to see emission features from ozone and nitric acid as well as from water and oxygen.

c. Recent Rocket and Balloon Observations. Rocket and balloon observations have been continued since 1971. The first rocket-borne experiment to find agreement with the 2.7K black body curve was that of Blair, et al. (1971) of Los Alamos Scientific Laboratory. Their bandwidth was from 6 to 0.8 mm. They obtained an equivalent black body temperature of 3.1 (+0.5, -2.0)K, so that their net signal-to-noise ratio was about 2. The same group flew another rocket with three detectors and filters in 1972 (K. D. Williamson, et al., 1973). Their three wavelength bands were 6-0.8 mm, 6-0.6 mm and 6-0.3 mm. In each band they achieved a signal-to-noise ratio of about 1 and found no disagreement with a 2.7K black body.

Muehlner and Weiss continued to fly their balloon-borne apparatus with modifications and improvements. In their latest paper (April, 1973) they report results for the frequency ranges 1-11.5 cm^{-1}, 1-13.5 cm^{-1},

Reproduced with permission of the copyright owner. Further reproduction prohibited without permission.

and 1-18.5 cm^{-1}. Their results are consistent with a 2.7K black body, but their signal-to-uncertainty ratios in these bandwidths are respectively 2, 1 and <1. This uncertainty arises not directly from detector noise, but indirectly through the atmospheric corrections which must be made. They had two narrow-band filters tuned to the emissions of water and ozone, and they performed zenith-angle scans, but their corrections are still very indeterminate. In the highest frequency band, the atmosphere emits more than three times as much as the signal to be measured.

The Cornell-NRL group have continued to improve their instrument as well. Houck et al. (1973) report that they no longer observe high signal levels, and their results are consistent with a 2.7K black body over the wavelength range from 1.3 to 0.4 mm. Their net signal-to-noise ratio is also about 1.

The next step in balloon-borne observations is soon to be carried out. Chapter III of this thesis describes the design, construction, testing and flight of a liquid-helium cooled spectrometer for absolute flux measurements between 2 and 40 cm^{-1}. On its first flight it did not produce spectra due to a malfunction of a motor. We intend to make a new attempt in the coming year. The spectrometer system was initiated by Dr. Paul L. Richards, and John Mather and David Woody completed it and flew it.

Two British groups are also planning spectrometer experiments with balloons, and a French group at Meudon Observatory is preparing a broad-band radiometer for a balloon flight (Grenier, et al., 1973).

Reproduced with permission of the copyright owner. Further reproduction prohibited without permission.

C. Organization of the Thesis

This thesis contains descriptions of two experiments concerning the Cosmic Background Radiation. Chapter II concerns a ground-based search for emission lines, while Chapter III describes an instrument built to measure the entire spectrum from a balloon. Chapter IV gives the mathematics used for Fourier transformation of interferograms made with a Fourier spectrometer, and results of my computational investigations of phase correction. Chapter V discusses detectors we use and methods I developed for calibrating them.

Most of the research effort was spent on instrument design and detector development. The information presented here is, therefore, organized according to the major problems being solved, rather than by experimental technique.

To assist the reader who is interested in techniques rather than the actual instruments, I gave here the locations of the discussions of the most important techniques.

The most important subjects discussed are spectrometer design and operation. The Fabry-Perot interferometer is discussed theoretically in Sections II-B-1 and II-B-2 and the construction and operation of our submillimeter interferometer is described in Sections II-B-3 and II-B-4.

The Fourier transform spectrometer is a much more efficient instrument. In our balloon-borne radiometer, we use a Polarizing Michelson Interferometer. It is described in Section III-B-1-b, and its operation is discussed in Section III-C. Data analysis is discussed in Section III-C-3, where I introduce my least-squares fitting procedure. This process is used rather than Fourier transformation because we are studying an

Reproduced with permission of the copyright owner. Further reproduction prohibited without permission.

unresolveable series of atmospheric emission lines. These lines arise from only a few molecules, and therefore a least squares fit requires only a few parameters.

Fourier transforms themselves are the subject of Chapter IV. Phase corrections are important to us, so I made an investigation of the computations associated with them. A noise analysis is also present.

Detectors are of such major importance that they are described in three locations. Chapter V describes the methods of calibrating detectors and summarizes the results for nine detectors in various configurations. The detector used with the Fabry-Perot interferometer is described in Section II-B-8, and that used for the balloon-borne instrument is discussed in Section III-B-1-c. Immersion optics is discussed in all three locations, as an aid to improving the sensitivity of detectors.

Another subject discussed several times is the effect of light pipes and conical light condensers. Pipes are discussed in Sections III-D-7, V-A-2 and V-A-3. Cones are used in both spectrometers and with both detectors. The image ball construction for a cone is given in Section II-B-7, where I show that the construction has a simple interpretation in terms of the kinematical invariants. Cones are used with all our detectors, as they are the simplest systems which can efficiently illuminate a plane detector surface from all directions equally. Finally, we are using a conical antenna for the balloon-borne spectrometer. It is described in Section III-B-1-a, and its geometric and wave-optics properties are discussed in Section III-D. Both its emission and its diffraction are calculated.

Reproduced with permission of the copyright owner. Further reproduction prohibited without permission.

II. GROUND BASED OBSERVATIONS WITH A FABRY-PEROT INTERFEROMETER

A. The Problem

As noted in the Introduction, in 1971 there was relatively strong experimental evidence for the presence of extraterrestrial line emission in the 10-12 cm^{-1} frequency band. The apparent flux was $F_o = 1.3 \times 10^{-9}$ W/cm^2 sr, as reported by Pipher, et al. (1971), Muehlner and Weiss (1970), and by Beery, et al. (1971). Pipher had a broadband detector in a rocket, Muehlner and Weiss had a series of low-pass filters with an InSb detector in a balloon-borne radiometer, and Beery had a Michelson interferometer as a Fourier spectrometer with a large telescope on Mauna Kea.

We, therefore, set out to do a ground-based search for narrow lines. Even though the atmosphere has several strong absorption lines due to water and oxygen, there are windows in the 6-14 cm^{-1} band. These windows permit searches for narrow lines with high resolution spectrometers. With our spectrometer we easily achieved a resolution of 1%. High altitudes are still necessary to cut the amount of water vapor in the line of sight down to 1 ppt mm.

Because the excess flux F_o could not be understood theoretically, it seemed that it might be an experimental artefact. We therefore attempted to make our experiment as distinct as possible from that of Beery, et al. We chose a Fabry-Perot interferometer instead of the much more efficient Fourier spectrometers available. We frequently calibrated the instrument with a liquid nitrogen blackbody. We used signal averaging techniques with rapid scans of the spectrum to minimize the effect of atmospheric fluctuations.

Reproduced with permission of the copyright owner. Further reproduction prohibited without permission.

B. Experimental Design

Our observations were carried out with a high throughput rapid scan Fabry-Perot spectrometer, shown schematically in Fig. 1. Radiation from a 6° field of view on the sky was focused by a teflon lens and chopped at 550 Hz against an ambient temperature black body. The reflector at the front of the instrument could be rotated around the optic axis to permit spectra to be taken at any zenith angle. It could also be pointed down into a liquid nitrogen cooled black body which served as a calibration source and established a temperature scale for our spectra. A 3m long section of 7.5 cm diameter polished brass pipe transmitted the chopped beam to the interior of a laboratory building where the spectrometer (discussed below) was located. The detector was a liquid helium cooled InSb electronic bolometer, fed by a germanium cone (Vystavkin et al., 1970), A cooled transformer matched the detector to a room temperature FET preamp. Following amplification and phase sensitive detection the signal was fed to a signal averaging system which accumulated several hours of data by superposing successive spectral scans.

The spectrometer consisted of low and high finesse 3 in. diameter Fabry-Perot etalons (FP_1 and FP_2) in a series, with FP_2 operated in first order to act as an order sorter for FP_1. The reflectors in FP_2 were 125 line per inch nickel mesh, giving a finesse $N \approx 8$ at 1 mm; in FP_1, they were 300 lpi mesh having $N \approx 70$ (Ulrich, Renk and Genzel, 1963). Radiation with $\nu \geq 15$ cm^{-1} was rejected by a capacitative grid

Reproduced with permission of the copyright owner. Further reproduction prohibited without permission.

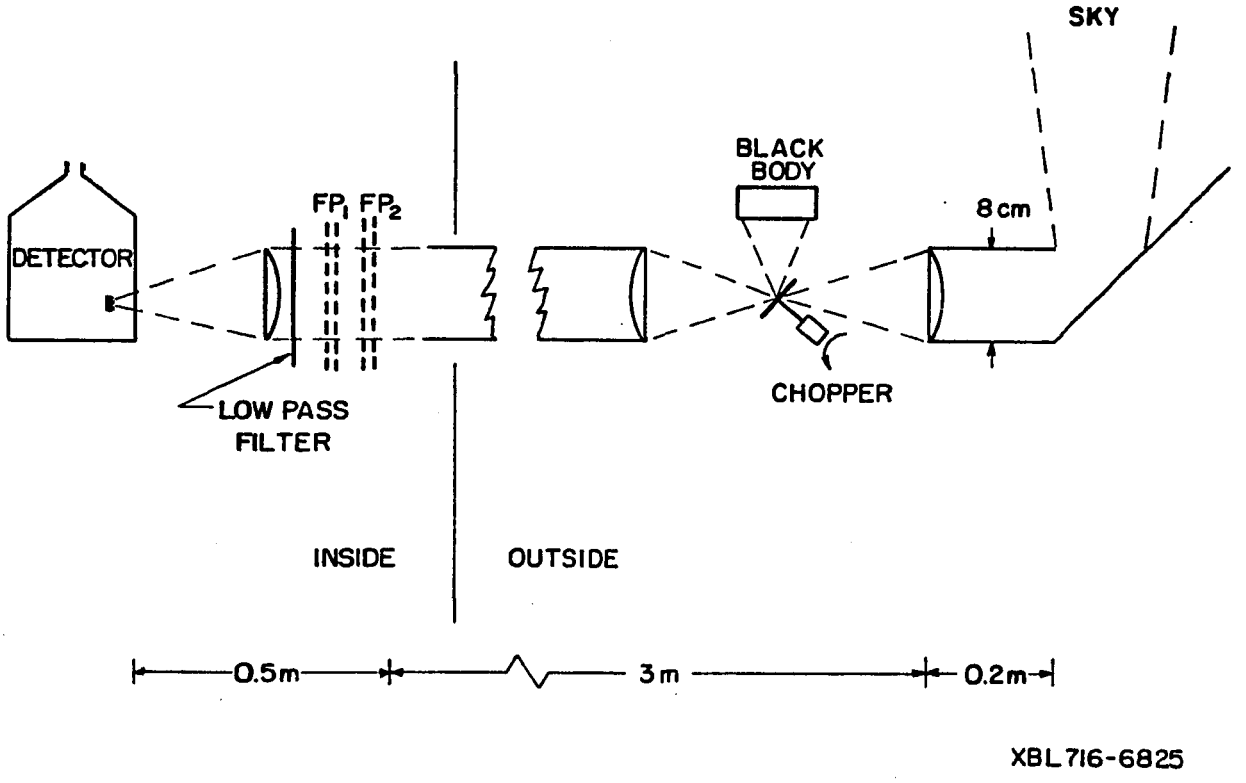

Fig. 1. Sub-millimeter Fabry-Perot spectrometer.

Reproduced with permission of the copyright owner. Further reproduction prohibited without permission.

low pass filter (Ulrich, 1967). In the 10-14 cm^{-1} region, we operated up to the third order of FP_1 and attained resolution ≈ 0.05 cm^{-1} at 10 cm^{-1}. We also carried out some observations at $\nu \geq 10$ cm^{-1}. Here the signal was so small that it was necessary to work in the first order of FP_2 or FP_1 alone, adding a polyethylene grating scatter filter to reject high orders. One of the reflectors of FP_1 was mounted on a microscope stage, which was driven by a stepping motor to scan the spectrum by varying the reflector spacing. When FP_2 was used simultaneously, its spacing was varied in such a way that the two etalons always transmitted the same frequency although they were set for different orders. The rate of scan was 0.1 cm^{-1}/sec and individual sweeps were accumulated for several hours with the signal averaging system. This rapid scanning greatly reduced the influence of slow fluctuations of the atmospheric water vapor emission on the averaged spectra. The noise temperature of our entire system was $\approx 20°K$ pk-pk for 1 sec of integration and 0.1 cm^{-1} bandwidth.

In order to be above much of the atmospheric water vapor, we carried out our observations at the University of California's Barcroft Laboratory at an altitude of 12,500 ft on White Mountain in Eastern California between April 27, 1971 and May 3, 1971. During the observing period, the atmospheric water vapor content was between 0.5 and 2 precipitable mm so that windows with greater than 50% transparency were available at frequencies up to 14 cm^{-1} (Nolt et al., 1971).

Reproduced with permission of the copyright owner. Further reproduction prohibited without permission.

1. Theory of Fabry-Perot Interferometers

My primary reference for submillimeter Fabry-Perot Interferometers (FPI's) is the paper by Ulrich, Renk and Genzel (1963). I will summarize here the basic formulas relevant to our instrument.

The Airy formula for the power transmissivity $\tau(\nu)$ of a FPI with two identical plane parallel reflectors and a normally incident plane wave of spatial frequency ν is

$$\tau = \left(\frac{T}{1 - R}\right)^2 \left(1 + \frac{4R}{(1 - R)^2} \sin^2 \delta/2\right)^{-1} , \qquad (1)$$

where

$$\delta = 4\pi n \nu d - 2(\phi - \pi) , \qquad (2)$$

and where $R^{1/2}e^{i\phi}$ is the amplitude reflection coefficient of a single reflector, T is its power transmissivity, A is its power absorptivity, and n is the refractive index of the medium between them, having thickness d.

At frequencies ν_q where $\delta = 2\pi q$, $q = 1, 2, 3, \ldots$ the FPI has maxima in transmission $\tau_o = T^2/(1 - R)^2$. For good plates this number can be near unity.

The resolving power Q is defined with $\Delta\nu$, the FWHM (full width at half maximum power points) of a given transmission maximum in order q:

$$Q = \nu_q/\Delta\nu . \qquad (3)$$

The finesse F is the resolving power in first order:

$$F = \frac{\pi}{2 \text{ arc sin } \frac{1 - R}{2\sqrt{R}}} \cong \frac{\pi\sqrt{R}}{1 - R} . \qquad (4)$$

For high resolution we need 1 - R much less than 1.

Reproduced with permission of the copyright owner. Further reproduction prohibited without permission.

In our case good mirrors were made from metal screens. Woven screens of round wires are available up to 120 lines/cm. For finer screens electroformed nickel meshes from Buckbee-Mears, Inc., work well. These are perforated sheets with square holes.

The proper electromagnetic theory of these meshes is difficult. The results are given by Ulrich, Renk and Genzel (1963). The properties seem well explained for $\lambda > g$ (where g is the grid spacing) by an approximation with superposed "one dimensional grids." A "one dimensional grid" is an array of wires like an ordinary diffraction grating or a snow fence, while a "two dimensional grid" is a screen with wires running in two perpendicular directions. For light polarized with its electric field parallel to the wires of a 1-d grid, the grid is a conductor and hence a reflector, and only a small amount leaks through. For light polarized with its electric field perpendicular to the wires, the grid has no conductivity averaged over a wavelength, and has little effect on the radiation. Hence, for a wave polarized parallel to a set of wires, there is little perturbation introduced if a second set of wires perpendicular to the first is added.

Symmetry agruments are sufficient to show that at normal incidence, the properties of a square mesh reflector are independent of polarization. Only two perpendicular polarization states are needed to specify the state of an incident wave, and the mesh treats both the same.

Reproduced with permission of the copyright owner. Further reproduction prohibited without permission.

2. Properties of 1-d Grids

A one dimensional grid in free space may be represented by an equivalent circuit of a transmission line shunted by a lumped impedance. For polarization parallel to the wires and for low frequency, the shunt impedance is small and inductive. For polarizations perpendicular to the wires, the impedance is large and capacitive. A form of Babinet's principle connects these two cases. Möller and Rothschild (1971) give multielement equivalent circuits that work over broader frequency ranges.

In the limit $\nu << g^{-1}$ with transmission line impedance Z_o, the shunt impedance is jX_o, with $X_o = Z_o wg$, where w is a constant depending only on the cross section of the wires. For $a << g$ the formulas are:

$$\text{for circular wires of radius } a\,, \qquad w = \ln(g/2\pi a)\,, \tag{5}$$

and

$$\text{for flat wires of width } 2a\,, \qquad w = \ln \sin(g/\pi a)\,.$$

Then the phase of reflection is

$$\phi = \pi - \arctan\,(2X_o/Z_o) \cong \pi - wg\nu\,, \tag{6}$$

and the transmissivity and reflectivity are

$$T = 1 - R = \sin^2\phi \cong \tan^2\phi = 4w^2g^2\nu^2\,. \tag{7}$$

For our purposes the absorption which arises from finite conductivity is negligible. An approximate formula is

$$A = (2gR/u) \cdot (c\nu/\sigma)^{1/2} \tag{8}$$

where u is the circumference of the wires, c is the velocity of light, and σ is the conductivity of the metal.

Reproduced with permission of the copyright owner. Further reproduction prohibited without permission.

Putting these formulas together gives for the transmission of a FPI in vacuum

$$\tau = \left(1 + \frac{1}{4w^4 g^4 \nu^4} \sin^2(2\pi\nu(d + wg/\pi))\right)^{-1} \quad , \tag{9}$$

which gives finesse

$$F = \pi/(4w^2 g^2 \nu^2) \quad . \tag{10}$$

Calculating the resolutions at FWHM in first order gives

$$\Delta\lambda = 4w^2 g^2/\pi\lambda \quad , \tag{11}$$

$$\Delta(\lambda^2) = 8w^2 g^2/\pi, \text{ independent of } \lambda \ , \tag{12}$$

and

$$\Delta\nu = 4w^2 g^2 \nu^3/\pi \quad . \tag{13}$$

The fact that $\Delta(\lambda^2)$ is a constant was used in data analysis to simplify the computation of simulated spectra.

It is important also to see that the effect of the phase shift on reflection is merely that the waves appear to penetrate a distance $x = wg/2\pi$ past the reflector, and that this quantity is independent of wavelength.

In the case of high finesse, it is a very good approximation to resolve the Airy formula into a sum of Lorentzian line profiles.

If the plates are not flat or parallel, it is as though we have several FPI's side by side. To avoid serious perturbation of the transmission curve, it is necessary that the flatness be better than λ/F.

If the FPI is not illuminated at normal incidence, the lowest order effect is that d is replaced in the Airy formula by $d\cos\theta$, where θ is the angle of incidence of the ray, measured from the normal. This

Reproduced with permission of the copyright owner. Further reproduction prohibited without permission.

sets a resolution limit of $Q_{max} = 2\pi/\Omega$, where Ω is the solid angle of the incident cone of light. This formula follows simply from the formula for the differential of solid angle in spherical geometry:

$$d\Omega = 2\pi \sin\theta \, d\theta = 2\pi d(\cos\theta) \ . \qquad (14)$$

If the plates of the FPI are not identical, the result is that the efficiency is reduced. According to my derivations, the change to the Airy formula is simply that R and T are replaced by the geometric means of the values for the two plates.

3. Construction and Operation of the Fabry-Perot Plates

We constructed three sets of Fabry-Perot plates. All were made of Buckbee-Mears nickel mesh, glued to aluminum rings with epoxy and then stretched over specially flattened holder rings. The holders were made of stress-relieved aluminum, and their shapes are indicated in Fig. 2. The clear apertures were 7.5 cm.

One fixed-tuned reference etalon was made with 500 lpi (≈200/cm) mesh. Both meshes were mounted on a single support ring, separated by a spacer. The spacer was a ring made from brass shim stock about 0.05 cm thick by photoetching techniques, to avoid leaving burrs on the edges. The spacer showed a tendency to be curved but this could be overcome by stretching the mesh tightly over it. The shim shock appeared to be very constant in thickness. Our major evidence for this is the finesse of the FPI as measured by a laboratory Michelson interferometer and by the lower resolution FP set described below. It was necessary to prevent dust particles from lodging under the spacer ring.

Reproduced with permission of the copyright owner. Further reproduction prohibited without permission.

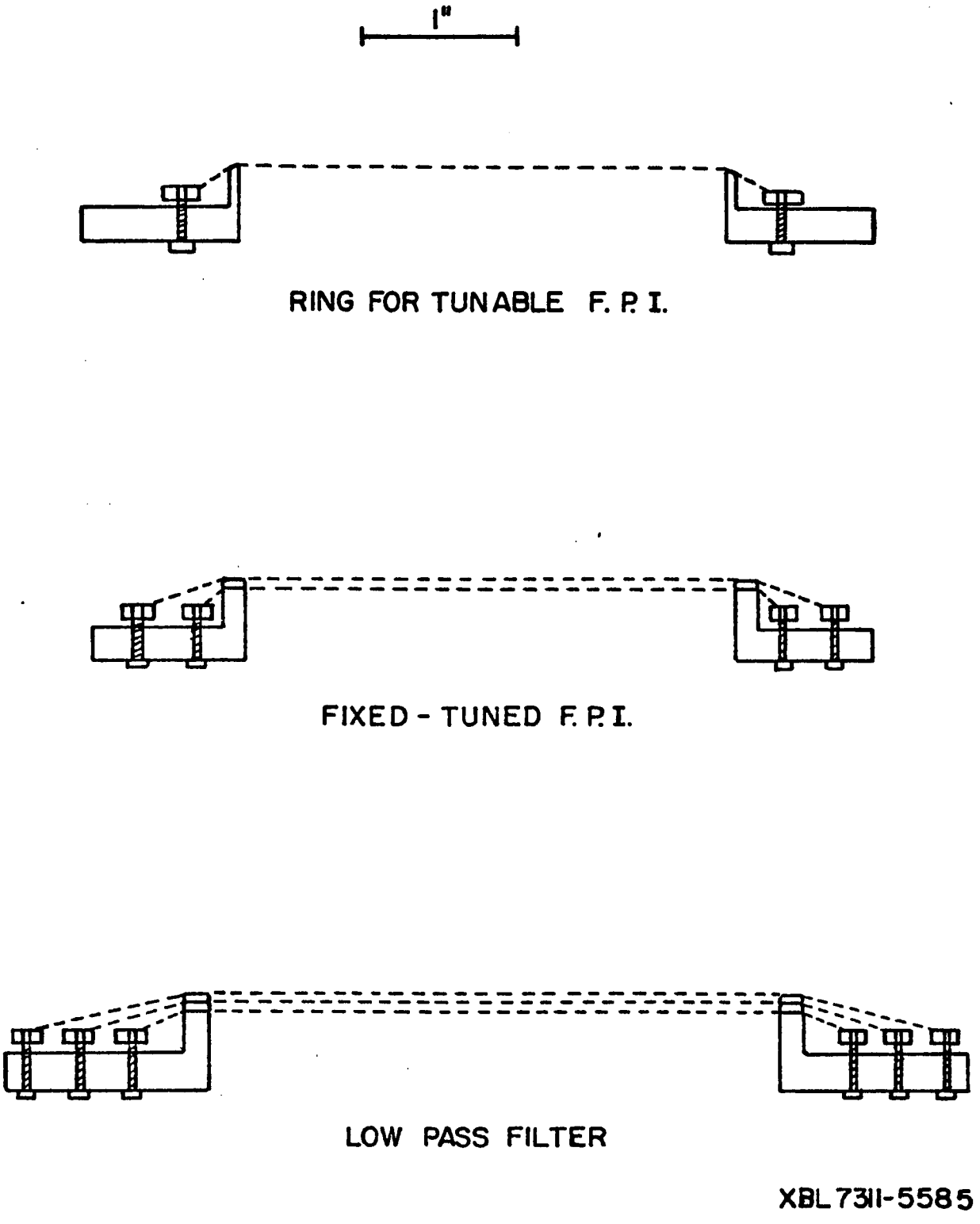

Fig. 2. Fabry-Perot Plates

Reproduced with permission of the copyright owner. Further reproduction prohibited without permission.

The second set of plates was the measuring etalon. One plate was fixed to the bed of a large (about 10×15 cm) microscope stage (Nikon) having motions in two directions. The other plate was attached to the grooved top plate. A large Starrett micrometer with a dial readable to one micron drove the stage.

The orientation of the mesh plate relative to its holder was determined by three 1/4-80 screws. One bore on a hole in the plate, another on a slot, and the third on a flat, giving a kinematic design. Two springs held the plate against the screws. This orienting system was a weak part of the design. It did not stay in alignment for more than a few hours at a time. Perhaps the springs were not strong enough, or the screws were loose in their holes. The alignment occasionally shifted by more than a milliradian. This was detectable by a loss of resolution in the spectra, or by frequent checks with a helium-neon laser, as described later.

An improved design would probably use true micrometer screws for the adjustments, or even differential screws. Keeping track of the settings would help, as the adjustments are not orthogonal, especially if it is desired to do the alignment by maximizing the signal from a monochromatic source. In addition, it would be desirable to separate the functions of angular orientation from those of lateral constraint. A third improvement would be a mount which allowed the meshes to be removed and replaced without spoiling the alignment.

A third set of plates was made to serve as an order sorter. Spectra could be usefully observed in the first through fourth orders of the main etalon. The moving plate of the order sorter was supported

Reproduced with permission of the copyright owner. Further reproduction prohibited without permission.

by three screws which rotated together, connected by a PIC toothed belt running over pulleys. Initially it was intended that the order sorter be set at a fixed position while the measuring etalon scanned the wavelength. This mode had an inconveniently short free spectral range, so we connected the toothed belt by shafts and a gearbox to the drive for the main micrometer. The pitch of the screws and the gear ratios were chosen to match the metric micrometer with English screws within 0.1%. This system worked but was touchy because of slight backlash problems. Better systems are needed.

Mounting the meshes on the rings required care. The nickel meshes are shipped sandwiched between two sheets for plastic for protection. They can be cut with scissors while still sandwiched, providing sharp new scissors are used, and the sandwich is held firmly at the edges to prevent relative motion of the layers. The meshes curl up spontaneously when free, and are very susceptible to the electrostatic fields produced by the protecting plastic sheets. It is necessary to handle the meshes in such a way that all the corners are always held down. Before gluing the meshes to our aluminum rings, we transferred them to a cardboard stretcher. Our procedure was the following: 1. Cut the mesh to size while still in its sandwich. 2. With tweezers, slightly separate the layers at one of the corners, and with scissors cut off a 1 cm triangle from each plastic sheet, leaving the corner of the mesh sticking out. Repeat for the other corners. 3. Cut a hole in a stiff card large enough to pass over the support ring to which the mesh will be glued. Be sure the edges of the hole are smooth.

Reproduced with permission of the copyright owner. Further reproduction prohibited without permission.

4. With masking tape tabs, tape down the mesh, still in its sandwich, at its four corners. 5. Lift off the top plastic sheet. 6. Lift the tape from the card at one or two corners to allow the lower plastic sheet to slide out, and then retape the corners.

4. Aligning and Testing the Etalons

We had expected to align our plates by maximizing their transmission for a monochromatic source. This turned out to be impractical because our monochromatic source was too weak, being merely our reference etalon as a filter for a black body source.

Our best method of alignment and testing was to reflect a laser beam from a small helium-neon laser from the plates, as shown in Fig. 3. The reflection showed a set of spots for each plate, arising from the diffraction of the light. For the coarse etalon (50/cm) and for the measuring etalon (120/cm) the method worked well as the nickel was sufficiently smooth to give bright reflections. It was not true of the reference etalon (200/cm) and of several other pieces of mesh similar to those used for the measuring etalon. We were fortunate in our initial choice. For the coarse etalon there were many bright spots so that a careful initial alignment with a micrometer was necessary to identify the central spot of the pattern.

To obtain full theoretical resolution, the plates of the measuring etalon had to be made parallel to within 0.1 milliradians. The laser beam was elliptical with a divergence of about 1×3 mrad, so it was very helpful to focus the beam with a lens. The method was to image the laser aperture on a screen after bouncing the light from the etalon. We used a 1 diopter lens with source and image distances of 2m. The image could be examined with a magnifier.

Reproduced with permission of the copyright owner. Further reproduction prohibited without permission.

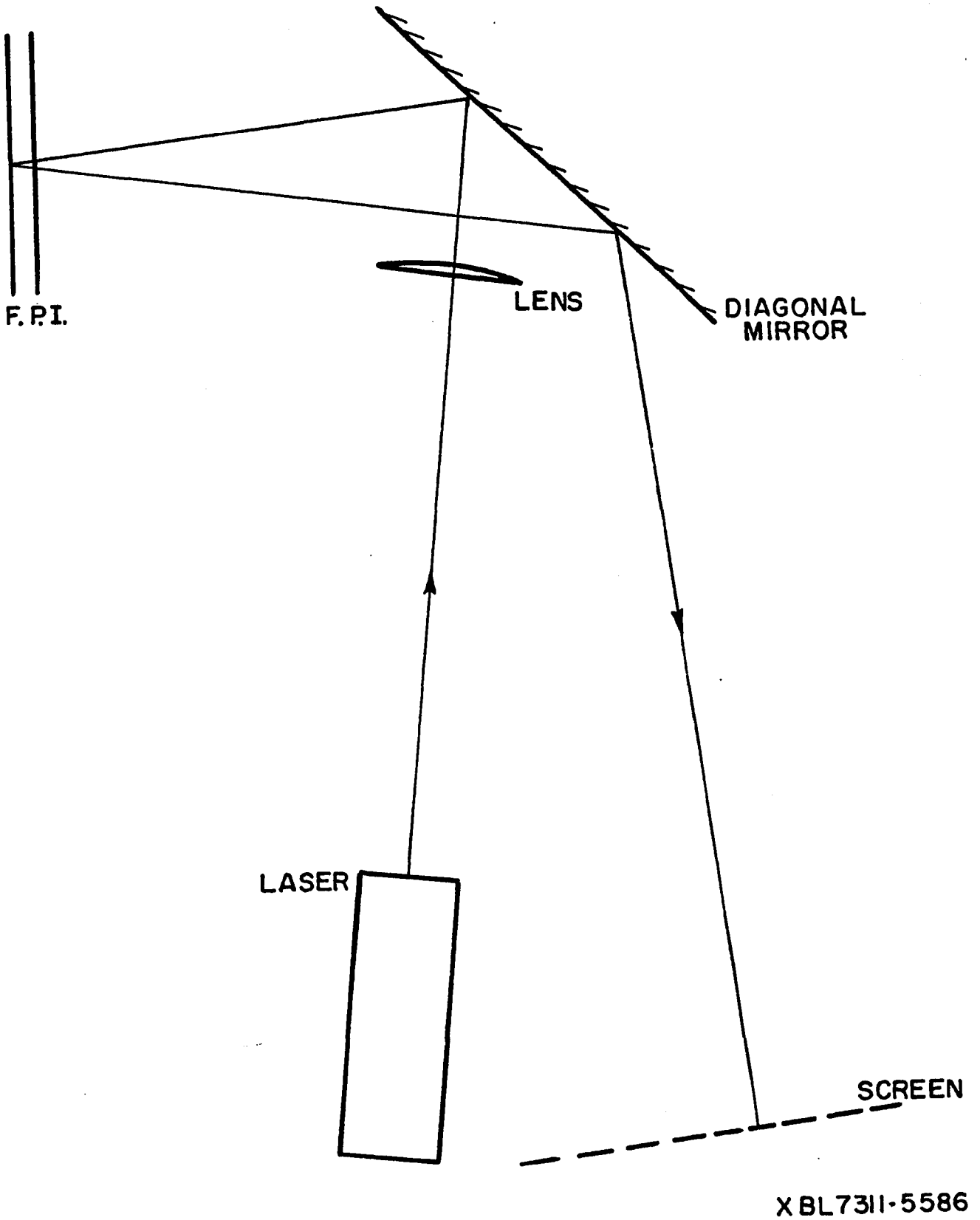

Fig. 3. Fabry-Perot Alignment

Reproduced with permission of the copyright owner. Further reproduction prohibited without permission.

The relative flatness of the plates could be determined by scanning the laser beam across the surfaces. The technique was sufficiently sensitive that deviations were always seen, especially near the edges. Some of the meshes had wrinkles in them which did not stretch out and were visible to the unaided eye. However, these did not seem to affect the large-scale flatness.

In order to achieve flatness it was necessary to lap the support rings. An aluminum block 20×25 cm was ground flat to better than 0.003 cm, and had a groove around the edge to which a vacuum pump could be attached for holding down sandpaper. A piece of 600-grit sandpaper was taped to the edges and a vacuum applied. Then the ring to be lapped was simply sanded on the surface, being held down with light finger pressure and frequently rotated to average out irregularity in the paper and the aluminum block. As measured with an electronic feeler gauge, the resulting surface was generally flat to better than 0.3 micron, quite sufficient for us, without any special effort.

We had some evidence that the springs and screws used for attaching the rings to the supports may have flexed them. One of the rings was made very thin because it was intended that it would vibrate at the chopping frequency. This idea was abandoned when it turned out that the optimum chopping frequency was around 1 kHz.

We also tested all our etalons for their infrared transmission and finesse. The reference etalon was used to test the measuring etalon and it in turn tested the order sorter. When one FPI is used to observe another, the apparent line profile is still a Lorentzian shape, whose width is the sum of the widths of the source and the

Reproduced with permission of the copyright owner. Further reproduction prohibited without permission.

instrument. This theorem may be demonstrated by direct convolution using contour integrals and residues, or equally well by looking at the Fourier transforms. In general our results agreed well with theoretical calculations when some allowance was made for residual distortions and lack of parallelism. Peak transmission of the order sorter was over 80% at 1 mm wavelength, while the measuring etalon reached at least 65% and the reference etalon 40%. These low values are due primarily to lack of flatness, but somewhat to the absorption in the metal. Copper plating has been suggested but was not attempted.

The etalons were also tested using a large laboratory Michelson interferometer having 15 cm optics and a maximum path difference of 10 cm, as described by R. R. Joyce (1970). The interferogram corresponding to a single Lorentzian peak in the transmission is an exponentially damped cosine wave. At large enough path difference, the sharpest line in the spectrum dominates the interferogram. Its width may then be ascertained from the damping factor of the exponential curve, even when there is not sufficient path difference or signal strength to fully resolve the line. In one case this equivalence was tested for a resolved peak and gave the expected answer.

The final test for resolution was the operational test. The data taken of the atmosphere were fitted to theoretical line profiles, accounting for the natural line shapes of atmospheric absorption lines and for finite resolution of the plates. The resolution was only slightly degraded from the theoretical values.

Reproduced with permission of the copyright owner. Further reproduction prohibited without permission.

5. Low Pass Filters

When metal mesh screens are used as Fabry-Perot reflectors, excellent filters are required to eliminate other orders than the one desired. For a given spacing of the plates, and when looking at a Rayleigh-Jeans black body, the total power transmitted in a given order is proportional to the fourth power of the order number. When the interferometer is to be used in lowest order, only a low-pass filter is necessary. When it is used in higher order, a bandpass filter is used, called an order sorter, and it is usually an etalon in first order together with a low pass filter.

Several types of low pass filters were used. A good summary of the available types is given by Möller and Rothschild (1971), Chapters 1 and 3.

The first low pass filter in our system was the atmosphere itself. At frequencies above 30 cm^{-1} or so, the atmosphere is opaque, even from a mountain top. The second filter was a series of three relatively thick Teflon lenses, so that each ray passed through about 3 cm of Teflon. The absorption coefficient of Teflon is approximately proportional to frequency, except for a bump around 35 cm^{-1}. The loss in our lenses was about 40% at 14 cm^{-1}.

The third low pass filter was used only for measurements at frequencies below 10 cm^{-1}. This was a pair of polyethylene transmission gratings with 45° grooves, oriented so the two sets of grooves were perpendicular. Several sets of these gratings were required, since each has a useful frequency range of less than 40% where it has both good transmission of the fundamental and good rejection of the harmonics.

Reproduced with permission of the copyright owner. Further reproduction prohibited without permission.

Our gratings were measured to have transmission curves similar to these given by Möller and McKnight (1965).

Our fourth low pass filter was a multiple layer interference filter. The theory for these filters is given by Ulrich (1967). A "capacitive grid" is the complementary structure to a screen. It is composed of small isolated spots of metal, supported on a substrate. A two element equivalent circuit that works well for wavelengths larger than the grid spacing is a series resonant circuit, resonant at $\lambda = g$, shunting a transmission line. When a filter is constructed using two of these meshes, there is a broad low pass characteristic, but there are also a series of roughly equally spaced transmission peaks, as the plates form a Fabry-Perot Interferometer. The interference effects can be used to sharpen the low-pass characteristics. We used a filter having three layers and unequal spacings to suppress the high frequency peaks. Our filter has a cutoff around 14 cm^{-1} and a small (1%) peak a few cm^{-1} wide at about 35 cm^{-1}.

Our capacitive grids were made by evaporating copper directly onto thin (4 micron) Mylar in a vacuum, using a nickel mesh as a mask. This was done at a pressure of about 10^{-6} to 10^{-5} Torr at a distance of 25 cm from a 5 cm long boat of molybdenum. The Mylar and the nickel mesh were stretched over a spherical aluminum surface of radius about 1 m, to insure close contact. We experienced difficulty obtaining good results because the heat of the filament caused the Mylar to contract unevenly. A partial solution was to put a drop of diffusion pump oil under the Mylar to insure thermal contact. This was not completely satisfactory because the oil leaked through pinholes in the

Reproduced with permission of the copyright owner. Further reproduction prohibited without permission.

Mylar. It was also necessary to shield the part of the Mylar which was not supported by the aluminum stretcher.

Our fifth filter was the immersion optics system used to illuminate the detector, as described later. This only works well when good contact is achieved between condenser and detector. High efficiency requires contact within a hundredth of a wavelength, as it turns out. For our case I estimate that the cutoff frequency is 15 cm^{-1}.

Our sixth filter was the detector itself. We used InSb in the low impedance mode, with no magnetic field. According to a simple model, this material becomes transparent and ceases to absorb radiation above the electron collision frequency. For us this frequency is also around 15 cm^{-1}, and the experimental falloff is fairly steep.

The net result of these six filters was that the apparatus worked. The contamination from higher orders could be kept down to less than 10% of the signal when working in first order and looking at a black body. The efficiency was rather low.

6. Geometrical Optics: Lenses

Fast lenses were needed for the chopper system to keep the chopped image small. The small image allowed a good chopping waveform and a high chopping frequency. Three lenses were fabricated from Teflon having a clear aperture of 8.9 cm and a focal length of 12.7 cm, based on a refractive index of 1.44. The front surface of the lens, facing the parallel rays coming in, was a sphere of radius 5.6 cm, while the back surface was approximately plane. Spherical aberration is quite serious for a lens as fast as this, so the back surface was a curve chosen to eliminate it. No attempt was made to eliminate any other

Reproduced with permission of the copyright owner. Further reproduction prohibited without permission.

aberrations. The lens is essentially achromatic in our frequency range. Our lens surfaces were generated on a lathe, the sphere by a radius cutter and the second surface by numerical steps in the coordinates. The correction surface deviated from a plane by 0.26 cm at the edge, and had a slope there of 0.23. The surface was computed from the principle that all parts of the wave front should have the same travel time to the focus.

I will now give a brief derivation of the formula used to generate the curve. Referring to Fig. 4, the principle of equal travel times becomes

$$\begin{aligned} ct &= s_1 + ns_2 + s_3 \\ &= x_o + n(x - x_o)\sec(i - r) + \sqrt{(x - f)^2 + y^2}\ , \end{aligned} \tag{15}$$

where s_1 is the path length in vacuum before striking the lens, s_2 is the path length in the lens, n is the refractive index, and s_3 is the path length between the lens and the focus. The quantities (x_o,y_o) are the coordinates of the first surface, assumed known, and (x,y) are the coordinates of the unknown second surface. The quantities i and r are the angles of incidence and refraction, measured from the normal to the surface. If we say the first surface is spherical and put its center at (R,0), then its equation is $(x_o - R)^2 + y_o^2 = R^2$, and $\sin(i) = y_o/R$. Snell's law is $\sin(i) = n \sin(r)$. Trigonometric identities can express $\tan(i - r)$ and $\sec(i - r)$ in terms of $\sin(i)$ if so desired. The equation can be solved if Snell's law is used to give the equation for the refracted ray

Reproduced with permission of the copyright owner. Further reproduction prohibited without permission.

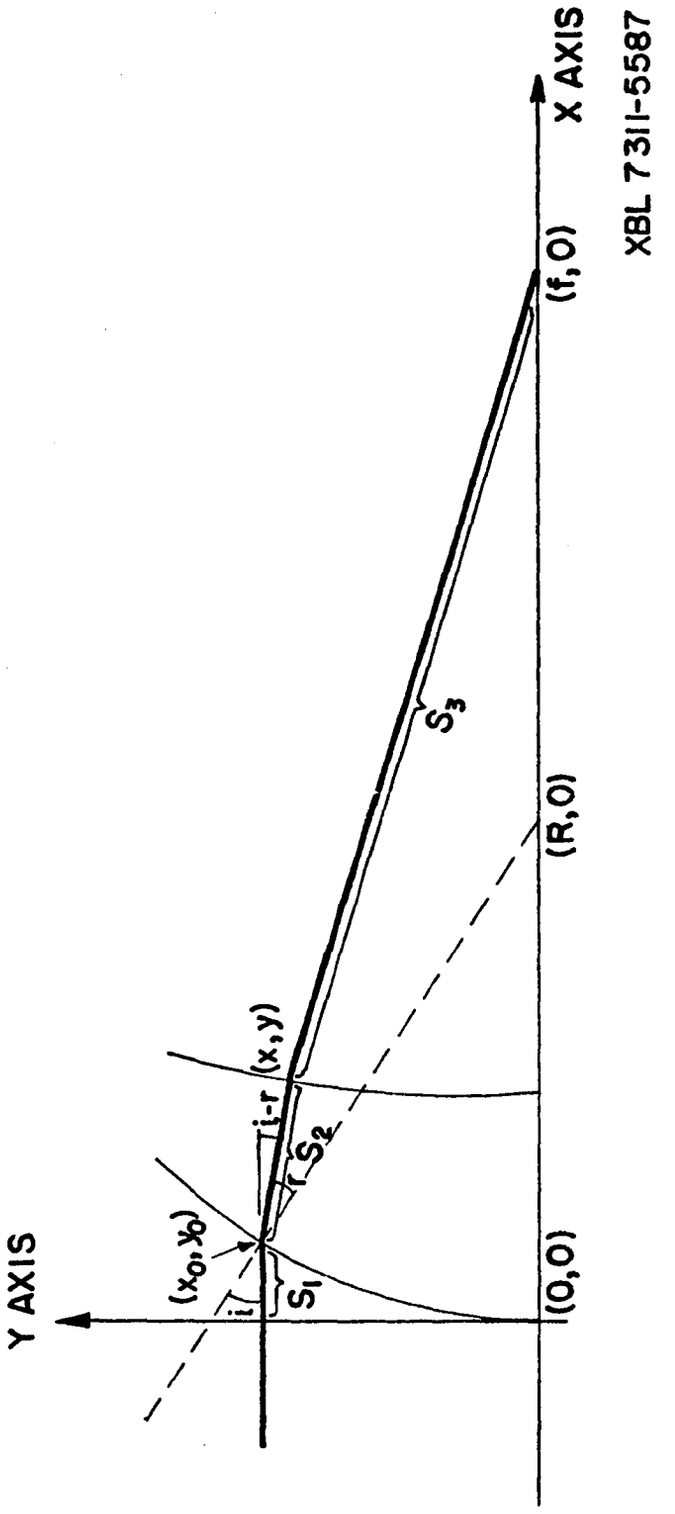

Fig. 4. Aspheric lens by Fermat's principle.

Reproduced with permission of the copyright owner. Further reproduction prohibited without permission.

$$y - y_o = -(x - x_o) \tan(i - r) \ . \qquad (16)$$

If we put in the known values of the invariant ct and assume an initial ray parameter y_o, for instance, then these equations mean that all parameters except x are known in Eq. (15) above. The equation is a quadratic which may be solved by computer easily. Then y can be found as well from Eq. (16).

Tests of the lenses showed good performance. Measures of the focal length of the lenses were made, giving a distance of 10.8±0.2 cm from the back surface of the lens to the focal point. Thick lens formulas in the Handbook of Military Infrared Technology then give the effective focal length as 12.3 cm, close to the expected value of 12.7 cm. Focal lengths were measured in several ways, of which the best was to image a small soldering iron on the detector with a symmetric pair of lenses as shown in Fig. 5.

7. Conical Light Condensers

We used a polished brass cone to condense the light into a light pipe which led into our detector cryostat. We also used a polished germanium cone just in front of the detector. Light cones are simple, fully enclosed, and efficient. A review of a small amount of literature about them is given in Möller and Rothschild (1971). A construction is given there which traces rays through a few reflections and generalizes from a two-dimensional case to the three dimensional cone, to show the following property, as shown in Fig. 6. The effect of the cone is to make the small aperture look like a sphere, especially when the cone angle is small. This sphere has the same center as the cone. Any ray which strikes the spherical image ball is allowed through the small

Reproduced with permission of the copyright owner. Further reproduction prohibited without permission.

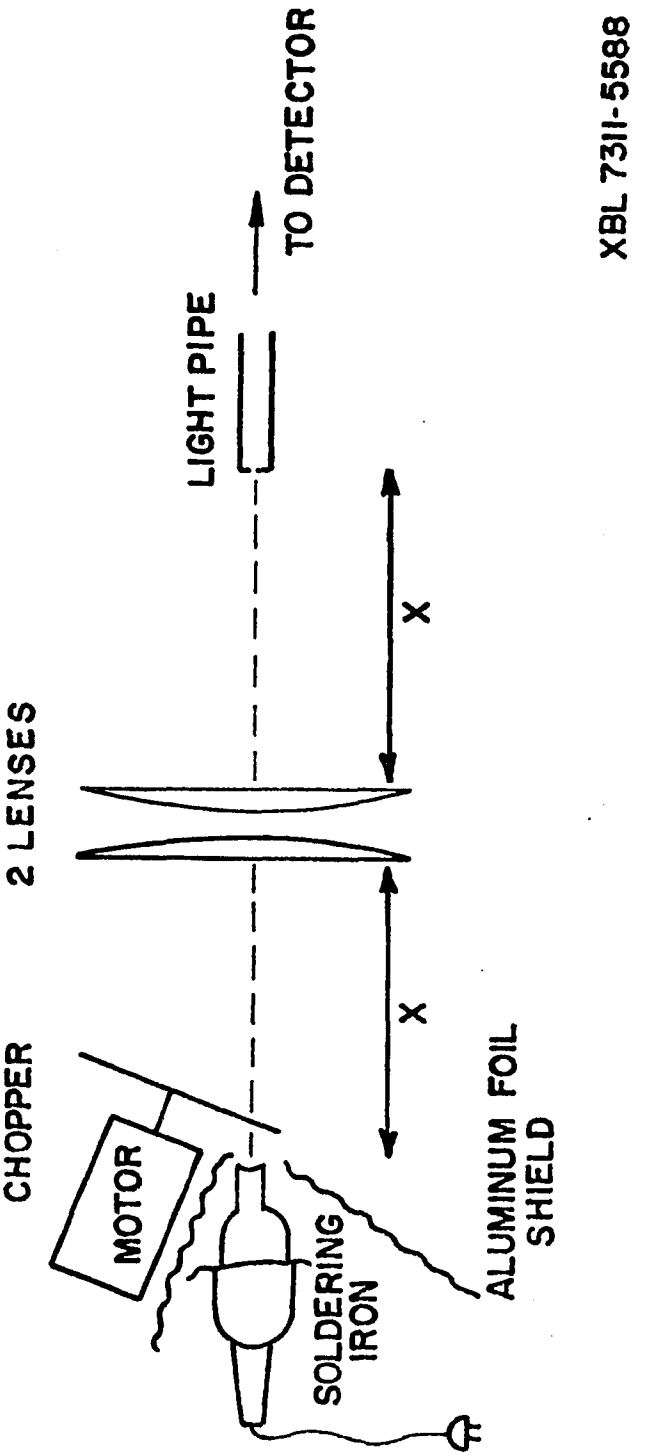

Fig. 5. Focal length measurement.

Reproduced with permission of the copyright owner. Further reproduction prohibited without permission.

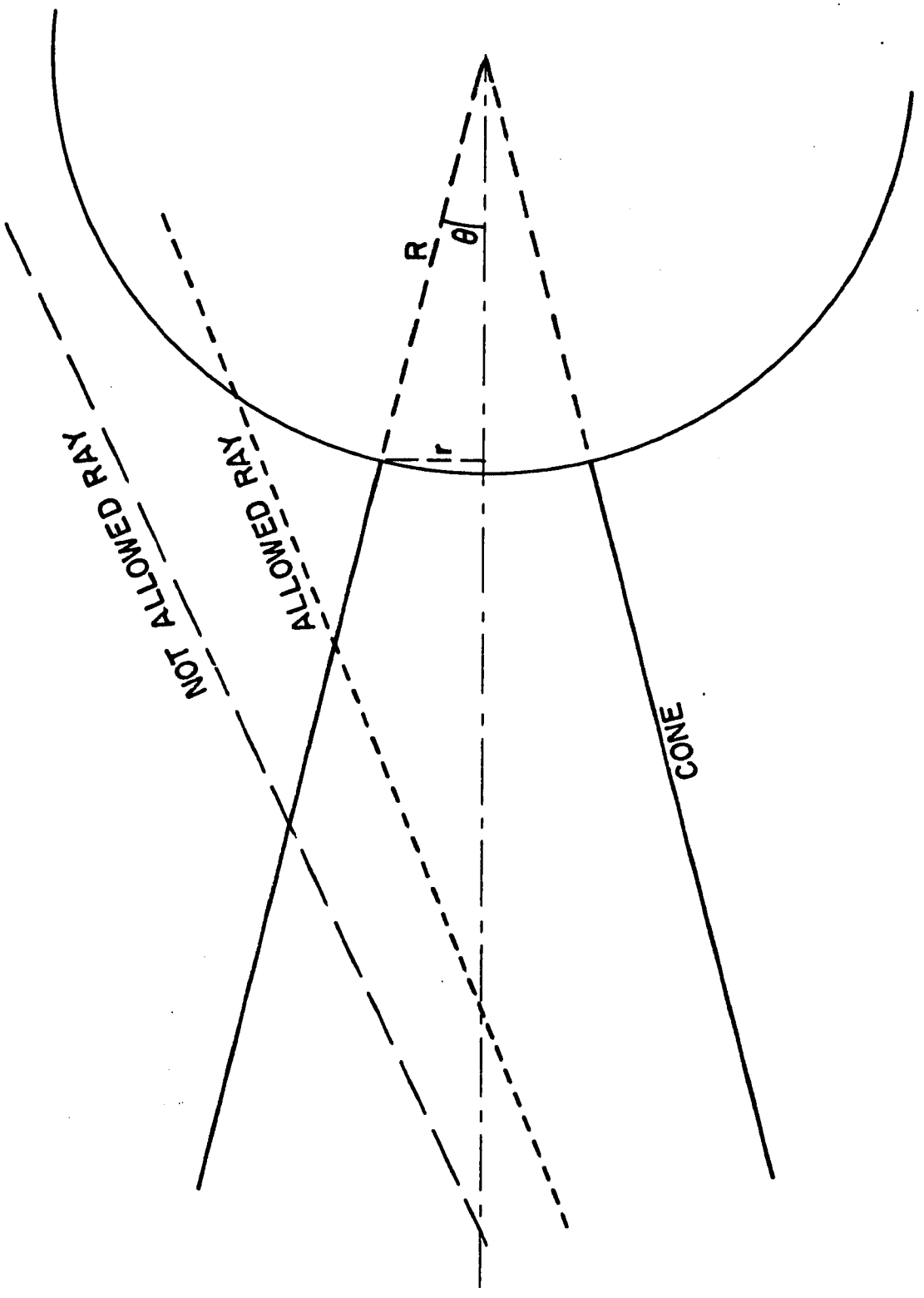

Fig. 6. Light cone and image ball.

Reproduced with permission of the copyright owner. Further reproduction prohibited without permission.

aperture of the cone.

I wish to show that this result is no mere generalization, but is the direct result of the kinematical invariants of the problem. In the case of spherical geometry the invariants are L_z, the angular momentum of a photon around the axis of the cone; and L^2, the square of the total angular momentum around the center of the sphere. For wave optics, these are the eigenvalues which describe a given mode. It is easy to see that they are conserved in the geometric optics problem as well, since each ray is reflected only from surfaces which pass through the center of the coordinate system and which are symmetric around the z axis. Now a ray which passes through the small aperture of the cone must have $L^2 \leq p^2R^2$, and $|L_z| \leq pr$, where r is the radius of the aperture and R is the radius of the image ball. The quantity p is the total linear momentum of the photon, which could be taken by convention to be unity for ray optics, but which would have importance for wave optics. The radius of the image ball is given by the relation $\sin\theta = r/R$, where θ is the half angle of the cone. The constraint that $L^2 \leq p^2R^2$ is equivalent to the construction of the image ball. The construction fails for large cone angles because the distance from a point in the plane of the exit aperture to the center of the sphere is not independent of its position in the plane. Hence, the maximum value of L^2 depends on the exit point and no single sphere works for all points. The limits given by L_z do not give further restrictions, at least when the cone is long and the angle is small. The throughput of a system like this is a constant as expected from the conservation of photons. It is $A\Omega = \pi^2r^2$

Reproduced with permission of the copyright owner. Further reproduction prohibited without permission.

as expected from the small aperture alone, accounting for Lambert's law. This subject will arise again in connection with the balloon-borne interferometer.

8. Detector Optimization

Our detector was one of several given us by Dr. Judy Pipher of Cornell. It is a piece of n-InSb, about 5 mm square and 0.5 mm thick, with leads attached with indium solder. It was selected as the best of its kind and compared with existing germanium and silicon bolometers. As operated, it was distinctly superior to any of the other detectors. It was operated in the circuit shown in Fig. 7, and its properties are summarized in Table I. No magnetic field was used, although the effects of a field were tested.

The transformer's properties are given in Table II. It was operated at liquid helium temperature, shielded by a mumetal can and additionally by a superconducting solder layer over the copper box which surrounded it. Without this superconducting shielding the transformer was sensitive to electrical interference from harmonics of 60 Hz up to the 12th. We looked for excess noise coming from the transformer, using helium temperature resistors substituted for the detector, and using an unbiased detector. For resistors of 200Ω and frequencies from 100 to 1000 Hz, excess noise was not more than the other noises. The preamp was a room temperature FET preamp with a noise of about 4 nv/$\sqrt{\text{Hz}}$, which was much less than the detector noise. The transformer was not apparently degraded by dc currents in the primary up to 3 ma.

Reproduced with permission of the copyright owner. Further reproduction prohibited without permission.

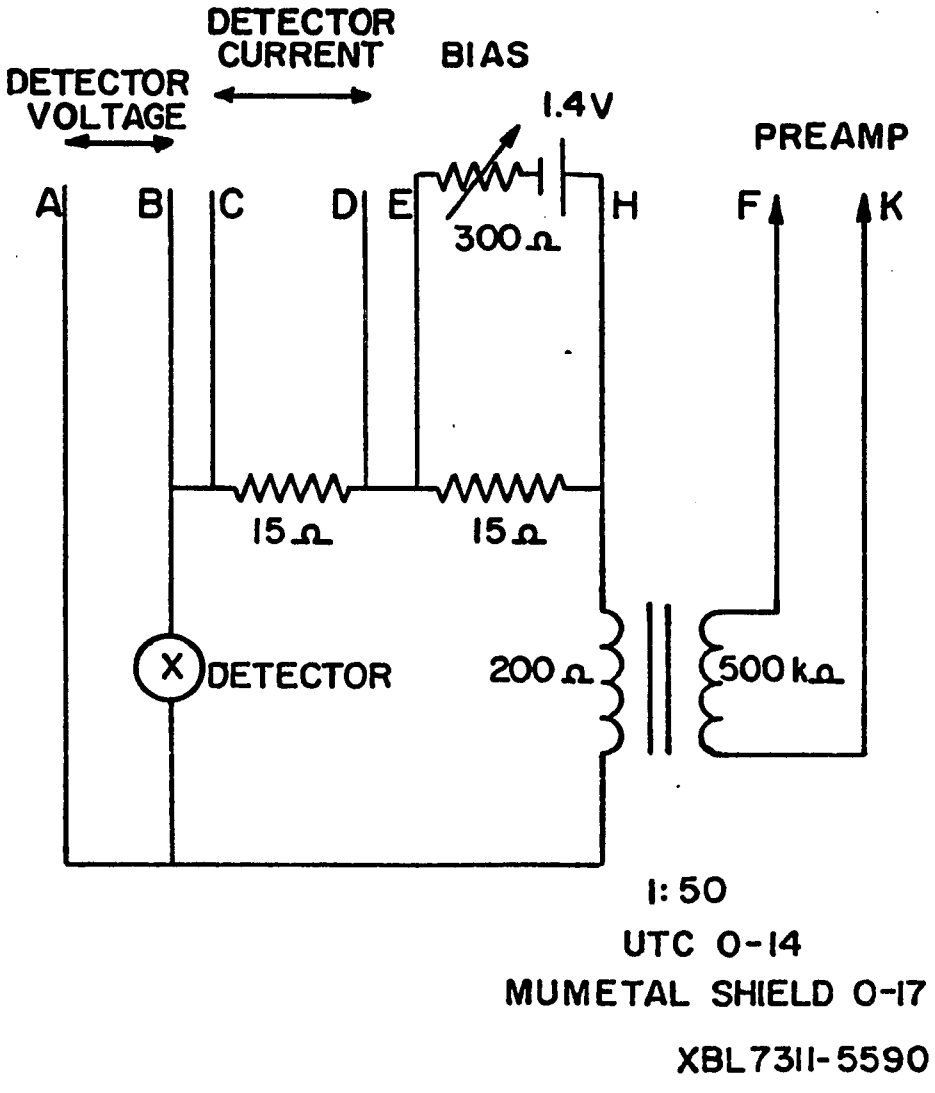

Fig. 7. InSb detector circuit.

Reproduced with permission of the copyright owner. Further reproduction prohibited without permission.

Table I. InSb Bolometer.

Source	Judith Pipher, Cornell University
Mounting	Vacuum Space, Infrared Laboratories Dewar
Size	$5^{\times}5^{\times}0.5$ mm
Throughput	0.25 cm^2-sr
Illumination	Immersion Optics with Germanium Condensing Cone
System Efficiency	0.1
Lattice Temperature	4.2 K
Bias Voltage	43 mV
Bias Current	0.15 mA
Resistance	255 Ω
Impedance	100 Ω
Responsivity	2000 V/W bare 10^5 V/W with 50:1 Transformer
Noise with Transformer	15 nV/$\sqrt{Hz}$ at 1000 Hz 50 nV/$\sqrt{Hz}$ at 300 Hz 90 nV/$\sqrt{Hz}$ at 200 Hz
NEP Electrical	1.5×10^{-13} W/$\sqrt{Hz}$ at 1000 Hz 5×10^{-13} W/$\sqrt{Hz}$ at 300 Hz 9×10^{-13} W/$\sqrt{Hz}$ at 200 Hz

Reproduced with permission of the copyright owner. Further reproduction prohibited without permission.

Table II. Transformer for Bolometer

Type	UTC 0-14
Shield	Mu metal, UTC 0-17; Superconductor
Nominal Impedance	200Ω-500kΩ
Turns Ratio	1:50
Nominal Frequency Range	50-5000 Hz
Secondary Inductance	2500 H±25% between Transformers at 300°K 1000 H at 4.2°K
Secondary Self-Resonance	500 Hz
Secondary Impedance	7 MΩ at 400 Hz
(primary open)	200 kΩ at 16 Hz
Primary Impedance	3000Ω at 500 Hz
(secondary open)	200Ω at 50 Hz, 5000 Hz 800Ω at 50 Hz with Resonating Capacitor
Primary Impedance	13Ω at 300°K, 500 Hz
(secondary shorted)	

Reproduced with permission of the copyright owner. Further reproduction prohibited without permission.

The entire system was mounted in the vacuum space of a 1 liter Infrared Laboratories helium dewar. Problems immediately arose with establishing thermal contact. We used vacuum grease in thin layers at all mechanical junctions. In the final configuration, the open end of the aluminum transformer was sealed with epoxy, and the mounting holes at the other end filled with greased screws. Gas trapped in the can, which can serve to establish heat contact down to 50°K or so where air freezes, may have been responsible for the success of this scheme. Two pieces of black polyethylene served as the cold low-pass filter. When this was used with a silicon bolometer it was unsatisfactory, as it seemed that it did not get cold. However, for InSb, the only requirement is that it stop the room-temperature emission of 5 micron radiation, which makes InSb a photoconductor. This pair of polyethylene layers was assembled as a sandwich in an attempt to trap a small amount of gas in the space between them.

Immersion optics was used for this detector, as suggested by Vystavkin (1970). The point is that the solid angle of a ray bundle is reduced by a factor of n^2 on entering a dense medium of index n. For InSb, $n^2 \approx 17$, so that in ordinary operation, a detector is not nearly filled with photons. Seventeen times as many could go through the same surface if it were not for the index change. If the detector were immersed in a medium of the same index, it could be smaller by a factor of 17 in area and would be more sensitive by a factor of ~4 if the usual scaling law applied.

Reproduced with permission of the copyright owner. Further reproduction prohibited without permission.

Our system used a condensing cone of pure germanium. This material closely matches the refractive index, having $n^2 = 16$. The cone is 2.5 cm long, 1 cm in diameter, and has a small end 1 mm in diameter. The large end is ground to a spherical surface with radius 3/4 the length of the cone, to act as a lens. This was necessary since no low-index optical material can achieve the required focal length. The small end was ground flat. Total internal reflection keeps the light in the cone until it reaches the detector, and actually keeps it in the detector too. With InSb detectors, the cone can be brought into thermal contact with the detector, since pure germanium is an electrical insulator when cold, and since the bolometer is not dependent on the lattice temperature but only on the electron temperature. When the cone was added to the system, there was no change in the sensitivity at frequencies below about 10 cm^{-1}, and there was a loss at higher frequencies. The frequency dependence is due to poor optical contact, which must be better than a hundredth of a wavelength for the efficiency to be better than 70%. Immersion optics would have been more beneficial if I had made a smaller and more sensitive detector.

Noise from the detector was measured using a lock-in amplifier, the PAR HR-8. Various methods were tried and found to agree. The simplest way is to set the output time constant to 1 sec, with 6 dB/octave filtering, giving a noise bandwidth of 0.25 Hz. If the output is observed for 1 minute, then the expected peak-to-peak fluctuation is about 5 standard deviations, for Gaussian or white noise. This number 5 is not very sensitive to the observing time used because slightly larger deviations are much more improbable. The method gave

Reproduced with permission of the copyright owner. Further reproduction prohibited without permission.

results good to around 20% usually. The noise formula is finally

$$\text{noise}/\sqrt{\text{Hz}} = 0.4\ (\text{peak-to-peak noise}).\ \sqrt{\text{time const.}}$$

Also used for these tests were true rms voltmeters and averaging voltmeters. An ordinary Simpson multimeter used as an AC voltmeter is an averaging meter. A large electrolytic capacitor across the meter movement can give it a time constant of minutes. The reading on the meter must be multiplied by a factor of 1.13 to account for the different calibrations for sine waves and noise.

C. Results

Figure 8 shows a first order spectrum of sky emission in the 7.5 - 13 cm^{-1} region, together with a theoretical atmospheric spectrum. The experimental spectrum in Fig. 8 is divided into two sections by a vertical line. These represent the ranges of actual experimental scans. The data in each range were obtained under different conditions of water vapor, resolution, and noise. Each section of the experimental curve is the weighted average of several individual runs. The individual spectra consisted of 1 to 3 hours of observation of the sky divided by a calibration spectrum of the liquid N_2 blackbody to establish a temperature scale. Because we measure the temperature difference ΔT between the sky and an ambient temperature blackbody, emission features (corresponding to a hotter sky and smaller ΔT) protrude downward on the plots. The theoretical spectra were prepared by using the compilation of H_2O lines given by Burch (1968) and the O_2 lines listed by Gebbie et al. (1969) to calculate atmospheric emission for an assumed atmospheric temperature $T_o = 270°K$,

Reproduced with permission of the copyright owner. Further reproduction prohibited without permission.

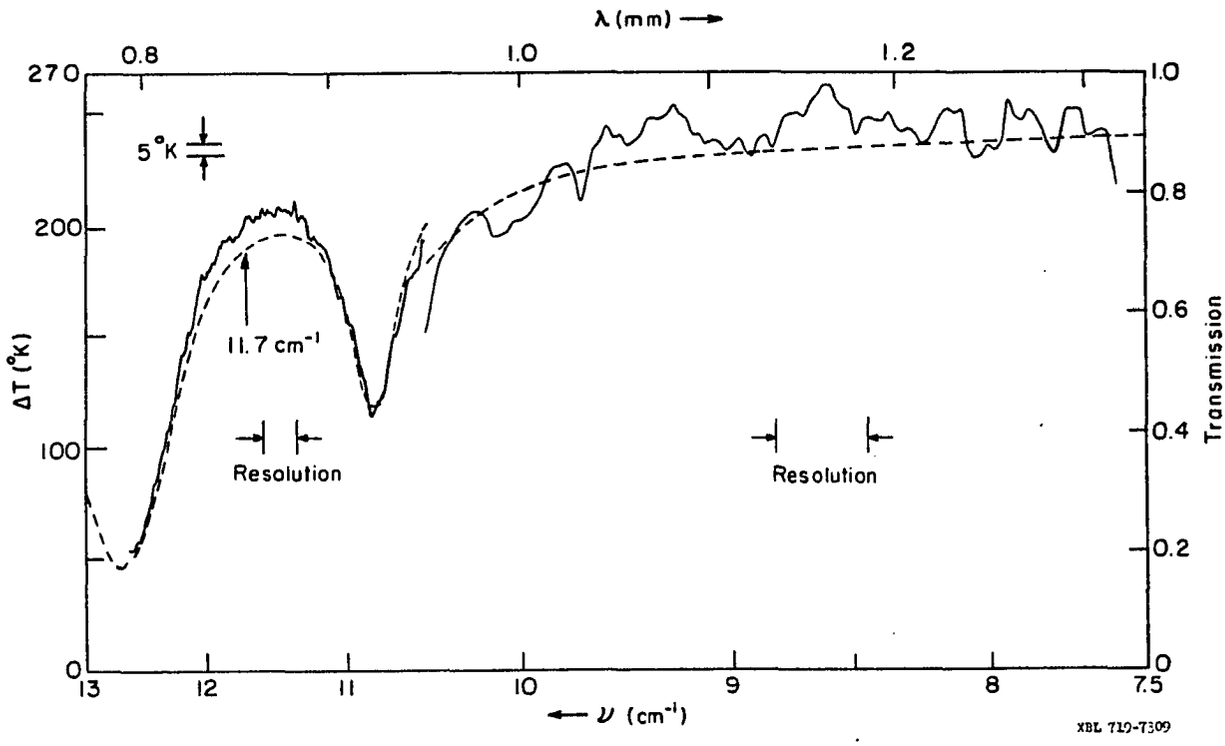

Fig. 8. Observed 7.5-13 cm^{-1} sky emission spectrum (solid) compared with theoretical spectrum (dashed) for 1.25 precipitable mm H_2O ($\nu > 10.6$ cm^{-1} and 1.5 precipitable mm ($\nu < 10.6$ cm^{-1}).

Reproduced with permission of the copyright owner. Further reproduction prohibited without permission.

pressure p = 0.67 atm, and various quantities of H_2O. The emission was convolved with our instrumental function to obtain the theoretical spectra shown. The theoretical curve shown corresponds to 1.25 precipitable mm of H_2O for $\nu > 10.6$ cm^{-1} and 1.5 precipitable mm for $\nu < 10.6$ cm^{-1}. The theoretical and experimental spectra show the expected strong lines of H_2O at 10.85 and 12.68 cm^{-1}. The continuum emission is due to the wings of the higher frequency H_2O lines. The close agreement between the theoretical spectrum and our experimental data is a useful check on our calibration procedure. Since the atmospheric H_2O above White Mountain is concentrated in a thin layer of (presumably) uniform temperature (O'Connor et al., 1968), the atmospheric transmission $t(\nu)$ may be estimated from our spectra as $t(\nu) = \Delta T(\nu)/T_o$. On the basis of this model the ordinate in Figs. 2-4 varies from zero to 100% transmission. Note that $t(\nu) \approx 70\%$ in the 11.5 cm^{-1} window, rising to >90% for $\nu < 10$ cm^{-1}.

Figure 9 is a third order spectrum of the 10-14 cm^{-1} region at three times higher resolving power than in Fig. 8. Note the O_2 lines at 12.3 and 14.2 cm^{-1}. The intent of this observation was to search with high resolution and low noise for sharp spectral features. To attain this goal, some sacrifice was made in the completeness of rejection of unwanted orders from the interferometer. Such contamination is largely responsible for the reduction in apparent transmission on the low frequency side as compared with theory or the data of Fig. 8.

We found no evidence for any features on our experimental spectra which can definitely be related to the hypothetical flux F_o. If we assume that $F_o = 1.3 \times 10^{-9}$ W $cm^{-2} Sr^{-1}$ was concentrated in a line of

Reproduced with permission of the copyright owner. Further reproduction prohibited without permission.

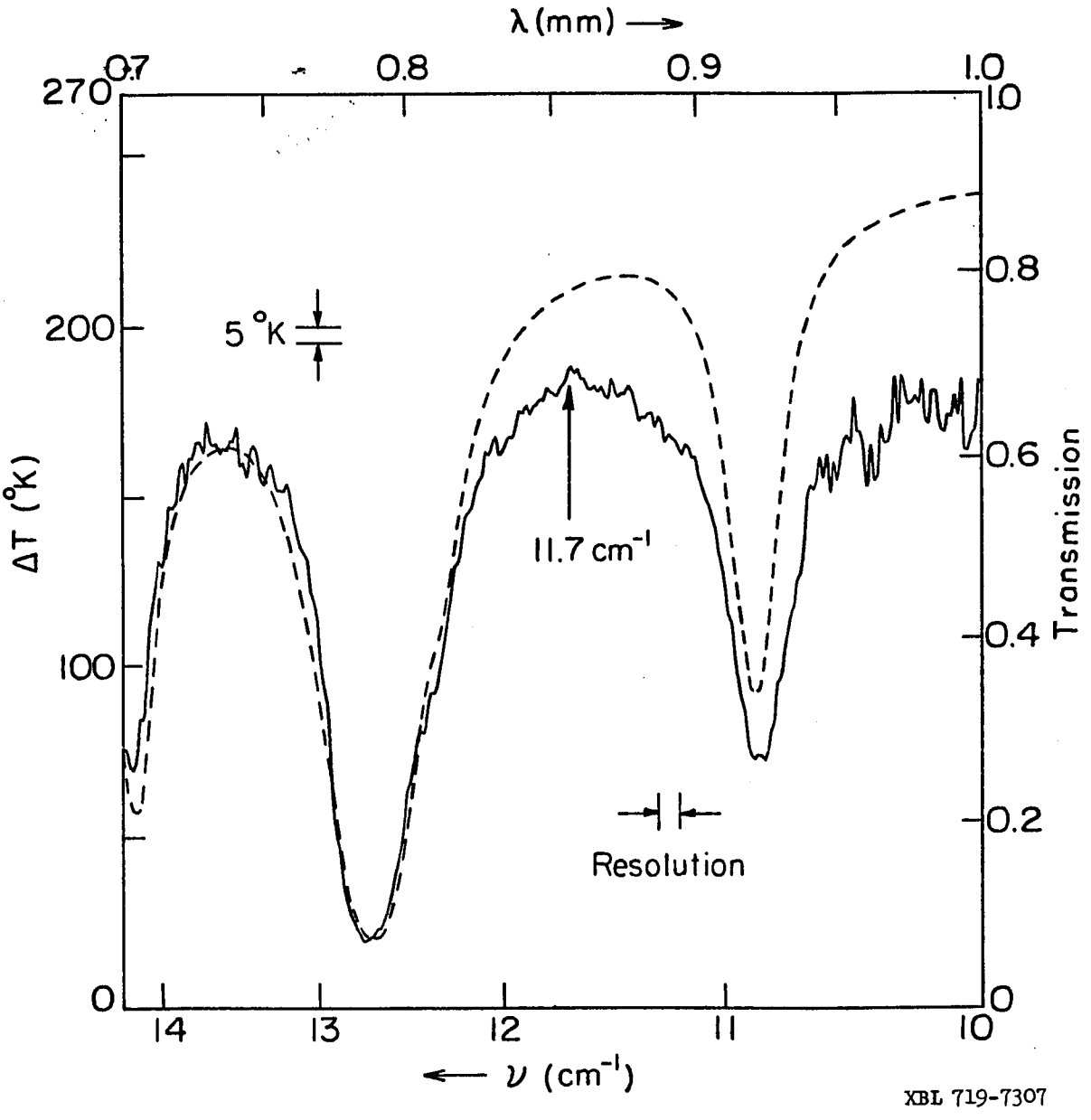

Fig. 9. 10-14 cm^{-1} sky emission spectrum observed in third order (solid), compared with theoretical spectrum (dashed) for 1 precipitable mm H_2O. Note the O_2 lines at 12.3 and 14.2 cm^{-1}. This spectrum contains a substantial contribution from unwanted orders from the interferometer.

Reproduced with permission of the copyright owner. Further reproduction prohibited without permission.

width $\delta\nu$ at frequency ν, this line would appear on our spectra as a feature of depth

$$T(\nu,\Delta\nu) = \frac{F_o t(\nu)}{2kc\nu^2\Delta\nu} = \frac{1570t(\nu)}{\nu^2\Delta\nu}\ ^\circ K \quad . \tag{17}$$

Here, k = Boltzmann's constant, c is the speed of light, and $\Delta\nu$ is the full width at half height of the line as it actually appears on the spectrum. If the feature is sharp, then $\Delta\nu$ equals the experimental resolution $\Delta\nu_I$. In this case $T(\nu,\Delta\nu_I)$ is very large (100°K line for $\Delta\nu_I = 0.08$ cm^{-1} at $\nu = 11.7$ cm^{-1}). No sharp feature approaching this strength appeared in any of our spectra. If the feature is much broader than $\Delta\nu_I$, its actual width $\delta\nu$ is observed and the depth is accordingly reduced. Our sensitivity to narrow features was greatest in third order (Fig. 9), while our sensitivity to broad features was greatest in first order (Fig. 8). Very broad features could not be detected because the atmospheric emission spectrum is not known accurately. By comparing the theoretical and experimental spectral shapes we set a lower limit $\delta\nu_L(\nu)$ to the width as a function of frequency of any spectral features contributing the flux F_o. On this basis, we arrived at the values for $\delta\nu_L(\nu)$ tabulated in Table III. The corresponding upper limits on the temperature of the feature calculated from Eq. (17) lie in the range 20-30°K.

The arrows in Figs. 8 and 9 at 11.7 cm^{-1} indicate the frequency at which Beery et al. (1971) reported detection of an emission feature with T = 30° and $\Delta\nu = 0.2$ cm^{-1}. In data obtained at various times throughout the day and night and at several zenith angles, we found no evidence for an emission feature at this frequency greater than

Reproduced with permission of the copyright owner. Further reproduction prohibited without permission.

TABLE III

Limits on Width of Sub-Millimeter Emission Feature

Contributing Flux $F_o = 1.3 \times 10^{-9}$ W/cm^2 Sr

Freq. Range	Total Observing Time	$\delta\nu_L(\nu)$
13.15-13.9 cm^{-1}	22 min.	0.25 cm^{-1}
11.1-12.1	7 (Fig. 8), 288 (Fig. 9)	0.4
10.65-11.1	120	0.1
7.5-10.65	200	0.5

$\delta\nu_L$ = minimum width of supposed feature. Limits are average values for each frequency range and vary from one frequency range to another because of differences in atmospheric transmission and observing conditions.

Reproduced with permission of the copyright owner. Further reproduction prohibited without permission.

the peak-to-peak noise, which was typically ≈5°K. The weak feature appearing at 12 cm^{-1} in Fig. 9 did recur in several individual spectra and may be real.

Figure 10 shows a low resolution spectrum of sky emission in the 6-9 cm^{-1} region. The main feature observed is the 6.11 cm^{-1} H_2O line. We saw no evidence for the diffuse emission reported in the 7-9 cm^{-1} region by several groups observing under conditions similar to ours (Harries and Burroughs, 1970; Gebbie et al., 1971) and attributed to the water vapor dimer $(H_2O)_2$. If the theoretically predicted dimer opacity (Viktorova and Zhevakin, 1967) is extrapolated to the atmospheric conditions for high altitude observations, the expected emission is somewhat less than the noise level in Fig. 10.

D. Conclusions from Ground-Based Observations

A consistent interpretation of all data on the sub-millimeter background available in 1971 required that the excess flux F_o be concentrated in the 10-12 cm^{-1} region. Our observations ruled out the existence of a single narrow line in this region carrying this much flux, such as might arise from an atmospheric maser. Thus, there seems to be no plausible terrestrial origin for this flux. Additionally, all features definitely present in our spectra over the wider region from 6 to 14 cm^{-1} were attributed to atmospheric O_2 and H_2O. However, our data could be reconciled with the earlier observations in several ways:

1. F_o is present in the 10-12 cm^{-1} region but the width of the feature is $\gtrsim$0.4 cm^{-1}, corresponding to a line depth $\lesssim$20°K. Under these circumstances, the line becomes difficult to detect because its width

Reproduced with permission of the copyright owner. Further reproduction prohibited without permission.

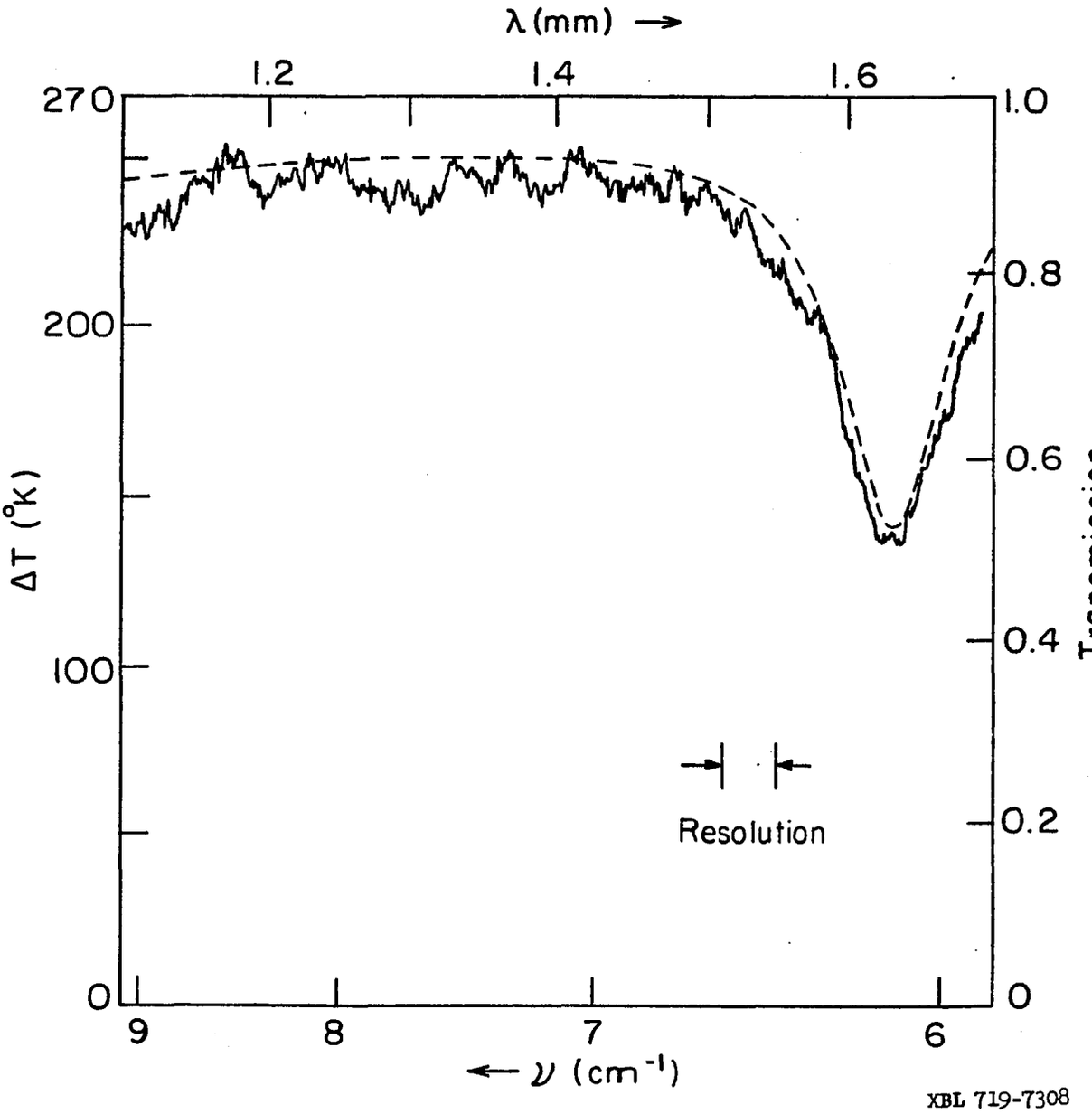

Fig. 10. Sky emission in the 6-9 cm^{-1} region (solid) obtained at lower resolution than Fig. 2, compared with a theoretical spectrum for 1 precipitable mm H_2O (dashed). Total observation time = 40 min. The main feature appearing is the 6.11 cm^{-1} H_2O line. Note the absence of any strong features in the 7-9 cm^{-1} region which could be attributed to the water vapor dimer, $(H_2O)_2$.

Reproduced with permission of the copyright owner. Further reproduction prohibited without permission.

is comparable with the scale of the structure in the atmospheric emission.

2. The radiation is present as a narrow line hidden behind the 12.68 cm^{-1} H_2O line. If the line is actually the 12.68 cm^{-1} H_2O line (say from an interstellar maser) one has the problem that this H_2O transition has an excitation energy of 200 cm^{-1} so that F_o may represent only a small portion of the energy emitted.

3. The radiation is due to a series of lines each contributing a fraction of F_o, clustered in the 10-12 cm^{-1} region. Since any line having width $\Delta\nu_I$ and $T \gtrsim 10°K$ would be apparent on our spectra, at least five such narrow lines would be required.

Reproduced with permission of the copyright owner. Further reproduction prohibited without permission.

III. BALLOON-BORNE SPECTROMETRY OF THE COSMIC BACKGROUND RADIATION

A. The Problem

In this section I describe the intentions of our experiment, the difficulties which must be overcome, the experiences of our predecessors in this field, and the present state of affairs.

Our balloon-borne spectrometer is designed to measure the spectrum of the cosmic background radiation in the frequency range from 3 to 18 cm^{-1}. This band includes about 90% of the total power emitted by a 2.7K black body. The total intensity of the emission from a 2.7K body is only 10^{-10} $W/cm^2 sr$, while the rate of photons is $10^{12}/cm^2 sec\ sr$. We are using a thermal radiation detector with sensitivity to absorbed power of only 3×10^{-14} $W/\sqrt{Hz}$, and an efficient spectrometer with a throughput of 0.25 $cm^2 sr$. Spectrometry of the 2.7K background radiation thus appears easy, especially when observing times of the order of 10^4 sec are available with balloons.

Complications arise, of course. First, our spectrometer is lossy, our detector does not absorb all incident radiation, and the radiation must be periodically interrupted by a chopper. The system has a net efficiency of less than 0.01 and detector noise is therefore important. Moreover, we are interested in spectral information, for which we must give up signal-to-noise ratio. Second, we are attempting to measure the spectrum at relatively high frequencies, well above the frequency of peak intensity. At 18.8 cm^{-1}, where $h\nu c/kT = 10$, the emission from a 2.7K black body is less than 10^{-5} as large as the emission from a 300K body. The entire apparatus is therefore immersed in liquid helium.

Reproduced with permission of the copyright owner. Further reproduction prohibited without permission.

The antenna must reject all radiation from warm objects without emitting any of its own. No window can be used to separate the liquid helium bath from the atmosphere, for even the thinnest available Teflon emits more than a 2.7K body at frequencies above 13 cm^{-1}. Third, the atmosphere emits more than a 2.7K black body at frequencies above 12 cm^{-1} even at an altitude of 40 km. A spectrometer is needed to measure the atmospheric emission. Water, ozone and oxygen molecules emit radiation with different zenith-angle dependences, and relative abundances are difficult to obtain from the zenith angle data alone.

Dirk Meuhlner and Ray Weiss of MIT have completed a series of balloon flights measuring the cosmic background radiation with broad-band filters. Their early flights produced data which did not agree with a 2.7K curve. Their most recent flight, October 1973, gave results consistent with a 2.7K curve (Muehlner and Weiss, April 1973). However, their signal-to-uncertainty ratio after corrections are made is only 2.5 for their lowest frequency band (1-11.5cm^{-1}), 1.2 for the middle band (1-13.5 cm^{-1}), and is less than 1 for their highest frequency band (1-18.5 cm^{-1}). Their largest uncertainties are not from detector noise but from atmospheric corrections, despite the facts that they had two filters specially tuned to the emissions of ozone and water, and that they were able to measure the zenith angle dependences of their intensities.

The experience of Muehlner and Weiss has been very valuable to us in designing our apparatus. Their observation of isotropy justifies our choice not to orient our antenna in azimuth. Their results

Reproduced with permission of the copyright owner. Further reproduction prohibited without permission.

confirming the 2.7K curve and estimating the densities of ozone and water allow us to plan our data-taking and analysis in accordance. They realized that a dielectric coating on a metal reduces the emissivity of the metal for grazing incidence radiation, so we have coated part of our antenna. Finally, they found as a result of an accident that at high altitude it may be unnecessary to use a window to separate the helium dewar from the atmosphere. They thus solved the problem of the window.

The present state of affairs is that Muehlner and Weiss have reached the limit of broad-band radiometry with their apparatus, and have ended this series of measurements. Our own apparatus has been flown once, on October 26, 1973. It malfunctioned and yielded no spectral information, but was recovered in good condition. It is being rebuilt and improved by David P. Woody for a future flight. Three other organizations have, to my knowledge, had plans to fly balloons to measure the far-infrared background radiation, namely groups at Queen Mary College (London), the University of Leeds, and Meudon Observatory (Grenier, et al., 1973). The first two will have spectrometers, while the third will not.

B. Description of the Apparatus

1. The Instrument

Our system is built into a liquid helium cryostat holding 62 ℓ of liquid. A scale drawing is shown in Fig. 11, a schematic drawing in Fig. 12, and a table of performance parameters is given in Table IV. The optical train consists of the following elements, in order: a warm calibrator, two windows, a warm horn, a long hollow conical

Reproduced with permission of the copyright owner. Further reproduction prohibited without permission.

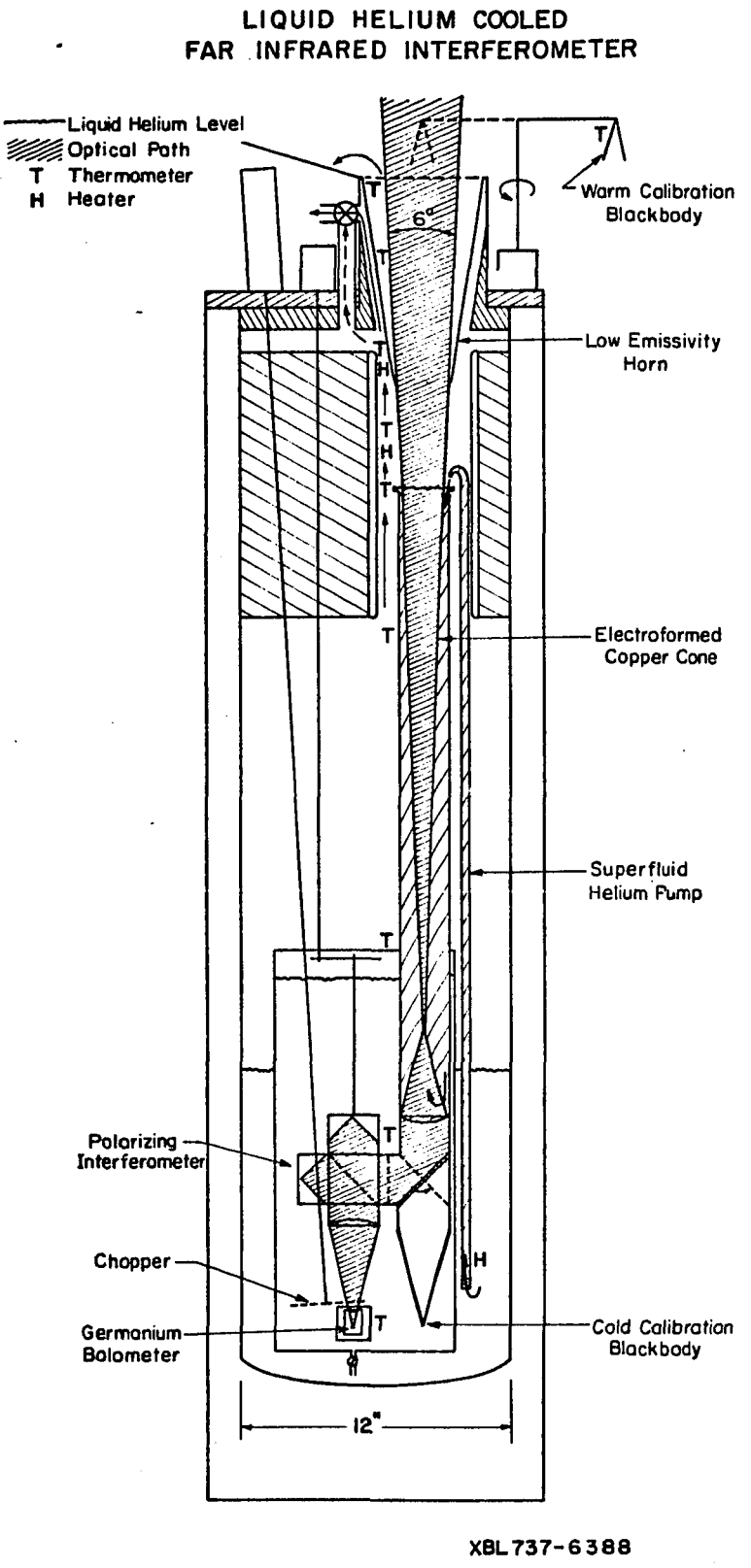

Fig. 11. Balloon-Borne spectrometer.

Reproduced with permission of the copyright owner. Further reproduction prohibited without permission.

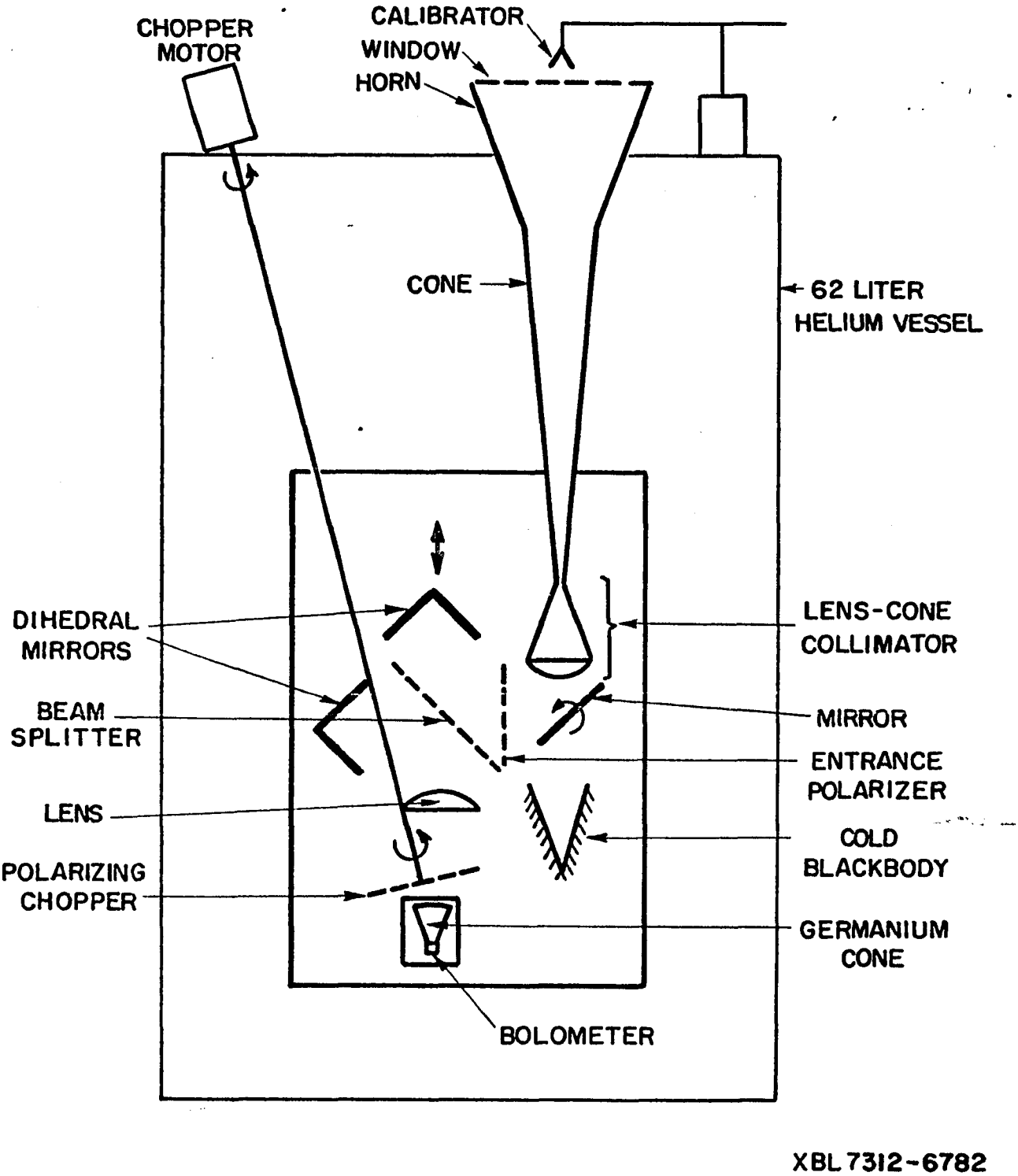

Fig. 12. Far infrared spectrometer schematic.

Reproduced with permission of the copyright owner. Further reproduction prohibited without permission.

Table IV. Balloon-borne system performance.

Property	Value
Geometric beam divergence	7.6° (farfield)
diffraction-limited effective antenna size	22cm
Throughput $A\Omega$	0.23 cm^2-sr
Resolution	$\geq$0.06 cm^{-1}
Frequency range	3-40 cm^{-1}
Power sensitivity	5×10^{-11} $W/cm^2 sr\sqrt{Hz}$ at 12 cm^{-1} (zero path)
Range of visibility of 2.7K black body	About 3-18 cm^{-1}, depending on resolution
Net efficiency	0.004 at 12 cm^{-1}
Approximate breakdown:	
antenna	0.95
lenses	$(0.93)^2$
input polarizer	0.5
vignetting	0.5
chopping	0.3
low pass filter	0.8
unfilled detector	0.33
bolometer and unknowns	0.24
	0.004
Helium capacity	62ℓ
Loss rate	2-3 ℓ/hr
Observing time at altitude	10-15 hr
Altitude	>35 km

Reproduced with permission of the copyright owner. Further reproduction prohibited without permission.

antenna, a re-collimator made with a hollow cone and a lens, a moveable mirror and cold reference black body , a polarizing Michelson interferometer used as a Fourier transform spectrometer, a chopper wheel, and a detector.

a. Upper Optics and Antenna. First, the calibrator is a thermal emitter, a black body at ambient temperature which may be moved into the beam. It is moved by a stepper motor on command. It is a hollow cone, cast of Eccosorb$^{T.M.}$ CR-110, an iron-filled epoxy. It fills 10% of the beam.

Second is a Mylar (polyethylene terephthalate) window, 0.013 cm thick, and 15 cm in diameter. It is carried on an aluminum frame so that it can be opened by command. It protects the instrument during ascent and is removed at altitude. Atmospheric emissions can be observed through this window, but not the cosmic background radiation.

Third is a Teflon window (polytetraflouroethylene) which is only 0.0003 cm thick. Some observations are made through this window, and then it too is removed. It keeps air out of the antenna.

Fourth is a low emissivity horn leading from the window down into the cryostat. Its diameter changes from 15 cm at the top to 6 cm at the bottom over a length of 25 cm. This horn is the warm part of the beam-defining optics. If it were not for diffraction, it would be entirely outside the geometric beam of radiation entering the antenna. However, 6 cm is only about 100 typical wavelengths across and diffraction is very important. The horn serves to minimize the effect of diffracted rays. It is made of stainless steel for low thermal conductance, coated with copper to maximize its reflectance for millimeter waves, and coated with 0.005 cm of polyethylene to further improve its reflectance

Reproduced with permission of the copyright owner. Further reproduction prohibited without permission.

for grazing incidence rays. The temperature of this horn ranges from ambient (200-300K) at the top down to a low temperature at the bottom which runs from 3 to 20K. The temperature is varied by command to study the emission from the horn.

Fifth is a long electroformed hollow copper cone. This cone is the primary beam-defining element of the system. Its diameter changes from 6 cm to 0.3 cm over a length of 70 cm. Its temperature is also varied to study its emission. The heat inputs to the cone and horn are metallic and gaseous conduction from the surroundings, radiation, and local electric heaters turned on by command. The heat outputs are metallic conduction to the boiling liquid helium bath at the bottom and gaseous conduction to the rising cold helium gas. Two fountain-effect superfluid helium pumps move the liquid helium to the top and bottom of the cone. These pumps are operated electrically by command. The rate of gaseous heat transfer is determined by the total gas flow rate, which is determined by the total amount of heat reaching the helium bath, and by a gas valve. The valve selects combinations of three gas flow paths: out the cone and horn if the window is open, or up the outside of the horn to cool it, or direct to the atmosphere without cooling the horn.

Sixth in the optical train is a short copper cone with a Teflon lens. These take the light which has passed through the 0.3 cm hole in the cone and collimate it to pass through the spectrometer. The beam is now 6 cm in diameter again.

Seventh is a mirror which bounces the radiation sideways into the spectrometer. This mirror rotates about a horizontal axis on command

Reproduced with permission of the copyright owner. Further reproduction prohibited without permission.

so that the spectrometer can also look down into a cold Eccosorb black body. The mirror is moved by a stepper motor on the top plate of the cryostat, and the connection is made by two cranks and a long wire cable. The cable slides inside two pieces of Teflon spaghetti insulation for low friction.

b. Spectrometer. Eighth is the spectrometer. This is a polarizing Michelson Interferometer (PMI). This is one of the most efficient known types of spectrometer for the far infrared. It was invented by Martin and Puplett (1970).

The classical Michelson interferometer used for visible light has been used since 1898 to give spectral information, but the spectra observed had to be simple line spectra to avoid confusion. The modern interferometer replaces the eye with a detector and digitizing system, the hand with a drive motor, and the brain with a digital computer performing Fourier transforms. In this form the interferometer has become a general purpose spectrometer capable of good efficiency, large light-gathering power (throughput, étendue), high resolution, and rapid data acquisition. It is compact and simple.

Other kinds of spectrometers used around 1 mm wavelength are Fabry-Perot Interferometers, ordinary grating spectrometers, grating spectrometers with coding masks to improve throughput and data acquisition rate (Phillips, Harwit, and Sloane, 1970), and microwave spectrometers. None of these have the advantages of the Michelson interferometer of wide bandwidth and simple mechanical construction.

The operation of the Michelson interferometer as a spectrometer has been described in numerous articles and has now been summarized in

Reproduced with permission of the copyright owner. Further reproduction prohibited without permission.

several excellent books. R. J. Bell's "Introductory Fourier Transform Spectroscopy" (1972) describes the history, the design, the operation, and the data reduction procedures, and discusses commercial instruments. The proceedings of the Aspen International Conference of Fourier Spectroscopy (1970) report many less conventional instrumental developments and innovations. The recent texts by L. C. Robinson (1973), K. D. Möller and W. G. Rothschild (1971), and G. W. Chantry (1971) are more general introductions to the field of submillimeter physics. Older books on interferometry include those by D. H. Martin (1967), W. H. Steel (1967) and M. Françon (1966).

Briefly, the interferometer operates by separating the incoming radiation into two beams. The beams are recombined after traveling different distances. When the two beams recombine they interfere. As the path difference between the two beams is varied, the output intensity varies to produce an interferogram. The part of the interferogram which depends on path difference is of utmost simplicity, being proportional to $\cos(2\pi\nu x)$, where ν is the spatial frequency of the waves, assumed monochromatic. Integrating over frequency gives, for the ideal system,

$$I(x) = \int_0^\infty S(\nu) \cos(2\pi\nu x)\, d\nu \ , \tag{18}$$

where $I(x)$ is the output interferogram and $S(\nu)$ is a spectrum to be determined. The spectrum is recovered by calculating an approximation to the Fourier inversion formula

$$S(\nu) = 2\int_{-\infty}^{\infty} I(x) \cos(2\pi\nu x)\, dx \ . \tag{19}$$

Reproduced with permission of the copyright owner. Further reproduction prohibited without permission.

In our polarization interferometer, drawn schematically in Fig. 12 and pictorially in Fig. 13, the interference occurs between waves of different polarization. The radiation is first polarized by an entrance polarizer. It is then split equally into two beams by a second polarizer called the beamsplitter. The beamsplitter polarization is 45° from that of the incident radiation. The two beams travel to dihedral corner reflectors which change the polarization directions by 90°, and return the beams to the beamsplitter. The beams recombine at the beamsplitter to produce a wave whose polarization state depends on the path difference x between the two beams. This recombined wave is entirely directed toward the output of the interferometer, and none is directed back toward the input polarizer. This occurs because of the change of polarization by the corner reflectors. The beam which was first reflected from the beamsplitter returns in the other polarization and is transmitted, and vice versa for the other beam.

As the path difference x is increased from zero, the (generally elliptical) polarization of the output wave goes from linear, to circular, to the perpendicular linear, to the other circular, and back to the original linear polarization state.

The polarization state of the output wave is analyzed by a polarizing chopper wheel. The wheel carries sectors of polarizer material which alternately transmit one linear polarization and then the perpendicular polarization. The difference between the intensities transmitted by the two orientations of output polarizer is proportional to $\cos(2\pi\nu x)$ as desired. There is no constant offset term as there is with many of the other forms of the Fourier spectrometer. This feature

Reproduced with permission of the copyright owner. Further reproduction prohibited without permission.

is one of the important virtues of this interferometer, as it means that variations in detector sensitivity or source brightness do not simulate spectral information, at least to lowest order.

The interferometer is constructed of Invar and aluminum. In the far infrared ordinary machine shop tolerances are sufficient for most purposes, so the mirrors, for instance, are merely polished aluminum blocks.

For our wavelength region, very simple and nearly ideal polarizing material is available. As discussed in connection with Fabry-Perot interferometers, a one-dimensional grid has the desired properties. It is an anisotropic conductor, conducting along the wires and not perpendicular to them. The material then transmits all of the radiation with electric field perpendicular to the wires and reflects all the radiation polarized parallel to the wires.

Our entrance polarizer and the polarizing chopper wheel are both made of gold wires, deposited on a Mylar substrate. The spacing of the wires is 0.00254 cm and the Mylar is also 0.0025 cm thick. The wires are protected by a coating. This material is commercially available from Buckbee-Mears, Inc.

The beamsplitter is made of copper-plated tungsten wires supported on an Invar frame. We made the beamsplitter this way for two reasons. First, the freestanding polarizer is a better beamsplitter than the dielectric-supported beamsplitter, since it avoids the interference effects between waves reflected from the dielectric surfaces and the waves that interact with the wires. Second, we can choose the grid constant of the wires to make the efficiency of the beamsplitter fall off at high frequencies. It is thus a low-pass filter.

Reproduced with permission of the copyright owner. Further reproduction prohibited without permission.

Reproduced with permission of the copyright owner. Further reproduction prohibited without permission.

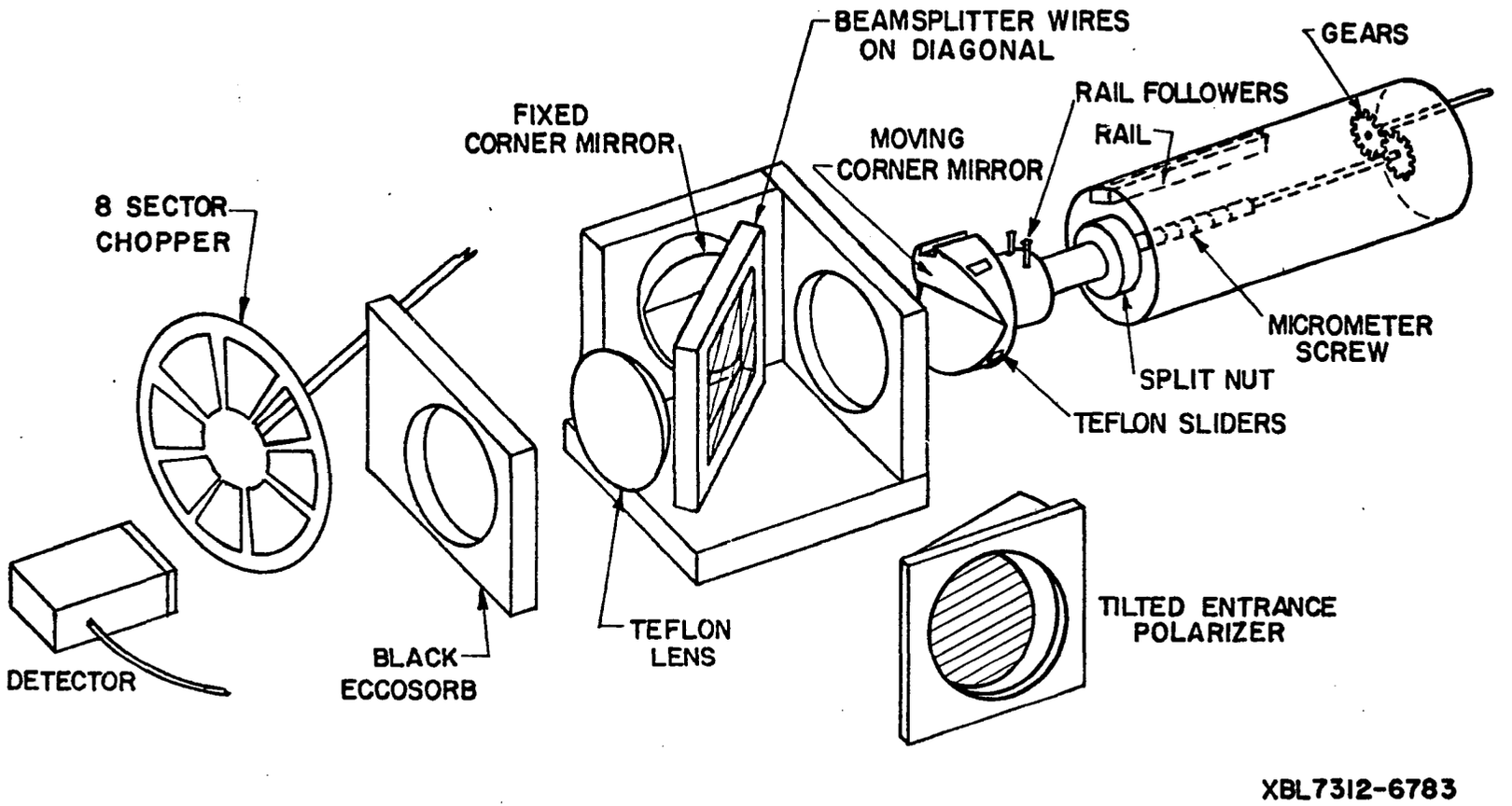

Fig. 13. Polarizing Michelson interferometer.

The tungsten wires are 0.0025 cm in diameter and are spaced by 0.0153 cm. With these parameters, the theory discussed in Section II-A-2 predicts that the efficiency is 90% at 16 cm^{-1} and drops rapidly to 50% at 36 cm^{-1}. The simple theory is expected to be inaccurate because it applies for normal incidence, while our incidence angle is 45°.

Measurements of the efficiency of the interferometer were made using a black body source and a calibrated Golay cell detector, and by direct substitution tests. The results are in doubt but suggest that the interferometer has a lower efficiency than predicted, and falls off at a lower cutoff frequency. At low frequencies, the efficiency is about 0.5. Several effects are thought to be involved. First, if optical surfaces are not flat, then the interference cannot be constructive. Surfaces need to be flat to about 0.05 wavelengths for full efficiency. At 20 cm^{-1} this length is 0.0025 cm, a tolerance easily achieved for solid mirrors, as described below. The beamsplitter is therefore suspected. It appears flat, and indeed the edge of the Invar frame is very good. The wires remain taut when the system is cooled in liquid helium because tungsten contracts more than Invar. The wires bend as they pass over the edge of the frame, and they are not all under the same tension. Moreover, the spacing of the wires could not be made perfectly uniform. A nonuniform spacing simulates roughness, since the reflected wave penetrates a distance behind the wires which depends on the spacing. For our case, a change in spacing simulates a roughness about 0.1 as large.

Reproduced with permission of the copyright owner. Further reproduction prohibited without permission.

The corner mirrors are made of solid aluminum, cut to shape on a milling machine, lapped on sandpaper as described previously in connection with the Fabry-Perot Interferometer, and then polished with Brilliantshine.T.M. The polishing was done with soft paper laps and was noticeably nonuniform, resulting in turned-down edges. A moderate polish is necessary for the visual alignment procedure described later. Estimates from the displacement of visual images indicate that the mirrors still are very nearly flat, for the purposes of the far infrared.

The interferometer path difference is varied by moving one of the corner reflectors with a micrometer screw. As shown in the figure, the moving mirror slides inside a tube. The micrometer screw is attached with a ball bearing to one end of the tube, and the nut on the screw is attached to the mirror. A follower on the mirror runs along a rail to keep the nut from turning. The micrometer screw is turned by a pair of gears, spring-loaded to take up backlash. One gear is connected by a stainless steel tube used as a shaft to a stepper motor (Slo-Syn$^{T.M.}$) on the top plate of the cryostat. The motor position is read out electrically by a potentiometer, and turns are counted by a precision shaft encoder on a gearbox.

The micrometer screw is from a Starrett micrometer with 5 cm travel, about 1.6 cm thread diameter, and 20 turns/cm. The length of this screw allows a best spectral resolution of 0.05 cm^{-1}. The screw has a split nut so the tightness can be adjusted. It was thoroughly degreased in trichloroethylene to permit use in liquid helium, but it soom rusted. It is now lubricated with a small amount of fine Teflon powder. It

Reproduced with permission of the copyright owner. Further reproduction prohibited without permission.

seems that the nut must be set rather loose to permit operation in liquid helium without squeaking, since the detector is sensitive to mechanical vibration. As a result, the precision of the screw has been sacrificed and the performance of the interferometer suffers. This design is under review. An alternative screw has been tested. It is a precision ball bearing screw made by Beaver Precision Products, Troy, Michigan, which appears to work very well when clean and tight. Its tightening adjustment, however, requires frequent attention when the screw is cycled between room temperature and liquid helium temperatures.

The chopper wheel is close to the detector, near the focal point of a Teflon lens. It has eight sectors of Buckbee-Mears polarizer with alternating directions. Its shaft runs straight to the top plate of the cryostat where it is turned by a gearbox and motor. The shaft is specially hardened stainless steel hypodermic needle tubing, 0.475 cm in diameter. It is supported by two bearings, one near the chopper and one near the middle. The bearings are Teflon-covered aluminum split blocks, clamped tight on the tubing. The tubing was polished with Brilliantshine to reduce wear. The bearings are perfectly quiet as far as the detector is concerned. The shaft turns at 4.26 Hz giving a chopping frequency of 17.1 Hz. The top of the shaft is connected by a specially made weak wire flexible coupling to the gearbox, which is a 9:1 PIC$^{T.M.}$ speed reducer. The input shaft of the gearbox is turned by a hysteresis synchronous motor (Globe$^{T.M.}$) whose two windings are driven with square waves at 76.6 Hz, 100 Vrms. These frequencies and gears were chosen to keep the acoustic noises produced by the chopper

Reproduced with permission of the copyright owner. Further reproduction prohibited without permission.

from simulating optical signals, and to separate the chopping frequency from fundamental telemetry cycle frequencies. Despite the weak coupling of the gearbox to the shaft, the detector output contains over a microvolt of kilohertz noise assiciated with the gear teeth in the speed reducer. A low-pass filter was installed in the detector preamp to minimize the effect of this noise on the telemetry.

c. Detector. Lastly, the detector is located directly under the chopper. It is a small germanium bolometer purchased from Infrared Laboratories after lengthy laboratory development efforts, described below in Chapter V.

The electrical and optical properties of the detector are described in Table V, and a drawing is shown in Fig. 14. The detector is operated in a mode not previously used with germanium bolometers. It is mounted in physical and optical contact with a pure germanium focusing cone, very similar to that used for the InSb detector for the Fabry-Perot interferometer. The new fact which came to light is that despite a gentle physical contact between the two pieces of germanium, there is no electrical or thermal contact. The force holding the bolometer against the cone is merely the elasticity of the wire leads to the bolometer. They are brass, about 0.0025 cm in diameter and 0.1 cm long.

Because this bolometer is smaller than the light beam to be observed, an improvement in signal is obtained when the cone is used. In this case an improvement of a factor of three is seen. The full improvement theoretically possible if all surfaces could be illuminated by the germanium cone would be 16 (the dielectric constant). We are illuminating only one part in 3.5 of the total surface area of the bolometer, since

Reproduced with permission of the copyright owner. Further reproduction prohibited without permission.

Table V. Germanium bolometer.

Property	Value
Source	Infrared Laboratories
Material	Germanium
Size	0.8×0.8×0.3 mm
Blackening	None
Resistance	$420\Omega \cdot \exp(17°K/T)$
Best Electrical NEP_e	$<2\times10^{-14}$ W/$\sqrt{Hz}$
Operating Point During Flight	
Bath Temperature T_s	1.5K
Bolometer Temperature T_b	2.2K
Voltage V	0.7V
Current I	0.7 μA
dV/dI	0 MΩ
V/I	1 MΩ
Responsivity	0.7×10^{6} V/W
Noise	40×10^{-9} V/$\sqrt{Hz}$
NEP_e	6×10^{-14} W/$\sqrt{Hz}$
Frequency	17 Hz
Time Constant	7 msec
Load Resistance	5 MΩ
Optical Properties	
AΩ (bare)	0.07 cm^2sr
AΩ (immersion optics)	0.25 cm^2sr
Absorptivity a	0.05-0.2 ? (temperature dependent)

Reproduced with permission of the copyright owner. Further reproduction prohibited without permission.

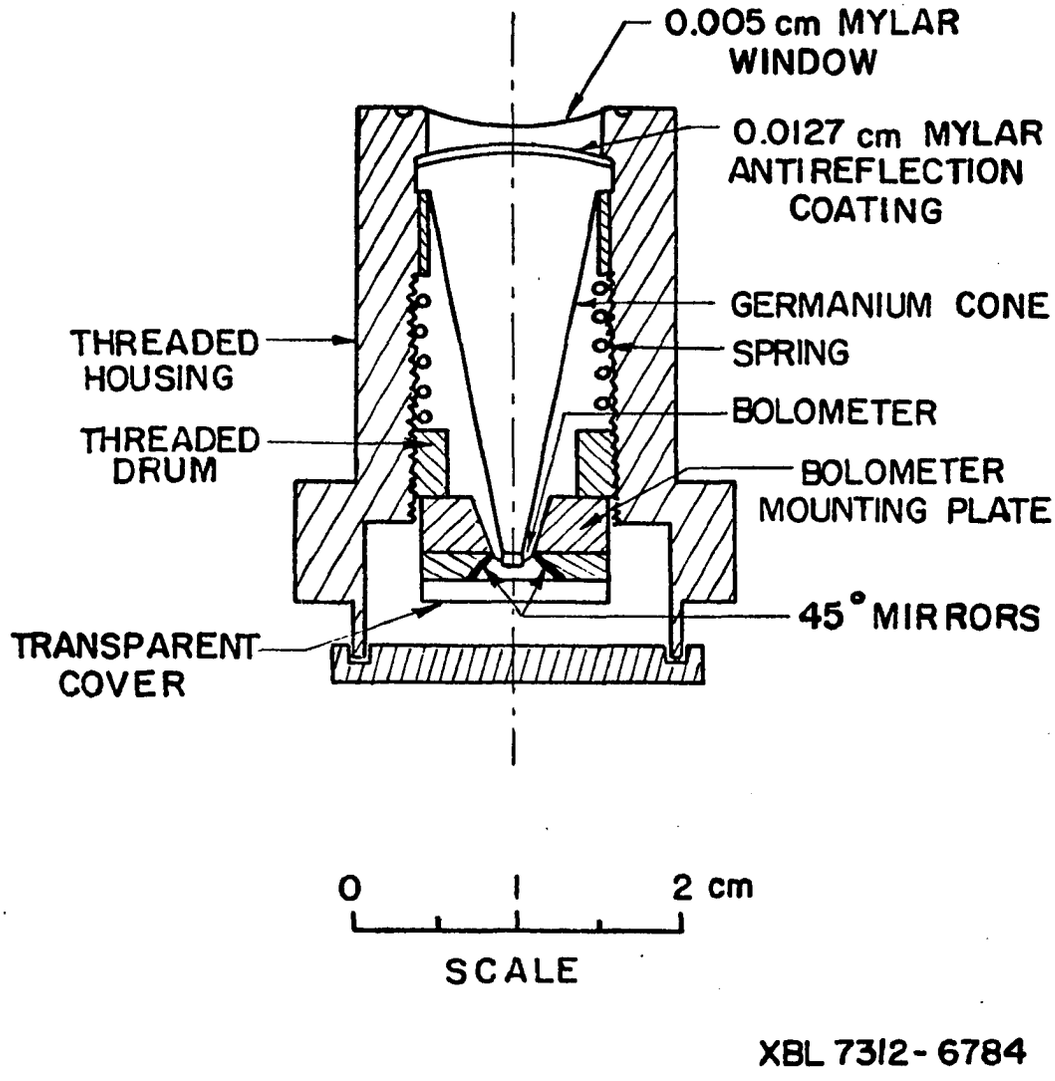

Fig. 14. Immersion optics mounting for Ge bolometer.

Reproduced with permission of the copyright owner. Further reproduction prohibited without permission.

we can make contact with only one surface out of six. It is presumed that the remaining discrepancy with the theoretical improvement is explained by lack of perfect optical contact and by not having a large enough light beam to completely fill the detector, owing to vignetting and imperfect alignment.

An additional factor of 1.3 is obtained by the use of an anti-reflection coating on the curved front surface of the germanium cone. This coating is a quarter-wave thickness of material with index of refraction approximating the geometric mean of the indices of the other two media. In this case the vacuum and germanium have indices of 1 and 4, while the coating is Mylar with an index of 1.75. The coating is 0.0127 cm thick, making a quarter wave thickness at 11 cm^{-1}. At 22 cm^{-1} it is a proreflection coating and causes a loss of signal by a factor of about 1.3. The Mylar was cut from sheet and heated in a mold to match the spherical shape of the front surface of the germanium cone. It is held down mechanically at the edge.

The detector is mounted in a brass vacuum chamber which has a window of 0.005 cm Mylar. This window is chosen because it can be made so thin that its reflection losses are negligible, and it is easy to attach. It is epoxied to the brass housing with Miller and Stephenson epoxy #907, after the Mylar has been sandblasted and the brass roughened with sandpaper. The adhesion is not very strong even so and the window must be protected from being peeled off. A small bag of activated charcoal in the vacuum space cryopumps the small amount of helium which diffuses through the window.

Reproduced with permission of the copyright owner. Further reproduction prohibited without permission.

The detector chamber is surrounded by a bakelite box with a Fluorogold$^{T.M.}$ top, which serves as a low-pass filter (Muehlner and Weiss, January 1973). The box is both a mounting device and a thermal filter. The time constant of the filter is set by the volume of the superfluid helium contained within it and by the area of superfluid channels connecting the inside to the outside.

The detector is biased by a cold 5 MΩ wirewound resistor and an R-C filtered adjustable room temperature voltage supply. Connections are made to the top of the cryostat with a special low-noise cryogenic coaxial cable (Microdot #250-3896-0000) which appears to be essentially noiseless for our purposes. Since the insulation of the central wire has a conductive coating, the cable must be arranged to avoid unwanted contacts to this coating. The load resistor is contained in a superconducting solder shield to minimize magnetic pickup from vibrations in the ambient magnetic field. Calculations showed that this would otherwise be important. The most evident source of microphonic noise was the connector to the preamplifier, which was therefore immobilized with a clamp.

d. Cryogenic Liquid Handling. Our cryostat has no liquid nitrogen chamber, being fully superinsulated and having a radiation shield thermally connected to the dewar neck, which is cooled by the escaping gases. Despite its large size and wide mouth, it dissipates only 0.25 ℓ of liquid helium per hour when there is no experimental apparatus installed. It was purchased from Cryogenic Associates. The capacity is 62 liters below the styrofoam plug which shields the top plate.

Reproduced with permission of the copyright owner. Further reproduction prohibited without permission.

The cryostat and spectrometer are precooled by partial filling with liquid nitrogen. A total of 15 liters of nitrogen are required to precool the system, and then some 15 more are added. This nitrogen is boiled by a heater to provide gas cooling of the neck of the dewar for a period of about 12 hours. Then the nitrogen liquid remaining is forced out and the last vestiges boiled away with the heater, which is held down onto the very bottom of the cryostat. Then the system is filled with liquid helium. Again it requires about 15 liters to cool it before liquid can remain inside.

Ensuring the cleanliness of the optical system is difficult. Before cooling with liquid nitrogen, the entire vessel is evacuated and flushed with dry helium several times until the gas which is removed is also dry. Purifying the helium is done by multiple passes through liquid nitrogen cooled tubes. Between passes through the liquid nitrogen, the helium gas is warmed up by tubes in warm water. This sequence seems necessary because a fraction of the water in the gas forms fog and does not condense on the walls of the tube. The purity of the gas is monitored by a glass U-tube dipping into liquid nitrogen which condenses impurities as they pass through.

After liquid nitrogen is in the dewar it is crucial to maintain a gas flow up the antenna and horn. Otherwise air which leaks in and vapors which are outgassed by styrofoam and other organic materials may diffuse down the antenna until they freeze on it. However, a quite moderate flow seems adequate for this purpose, and the cryostat may be kept cold for days with either nitrogen or helium, providing the gas flow is maintained, without generating visible condensation of solid air.

Reproduced with permission of the copyright owner. Further reproduction prohibited without permission.

It is important that if the system is evacuated while cold, this gas flow must still be maintained by pumping gas out through the antenna rather than by other paths.

The spectrometer itself is protected from the liquid nitrogen by a copper box. This box also keeps out stray radiation and keeps the spectrometer immersed in liquid helium even when the supply is low elsewhere. It proved to be difficult to prevent nitrogen from freezing into the micrometer screw without these precautions. The box is filled through either a valve at the bottom, or through a small hole at the top.

Liquid helium is moved about by two superfluid helium pumps mentioned previously. They use the thermomechanical effect, which in the two-fluid model of superfluid helium is just a kind of osmosis. R. J. Donnelly (1967) gives graphs showing the amount of pressure developed by such a pump, and describes the theory. The osmotic membrane is porous ceramic material called Lavastone,$^{T.M.}$ which may be fabricated while soft and then fired. The Lavastone allows the superfluid fraction of helium to flow freely but stops the normal fraction. The difference in concentrations which runs an osmosis machine is determined in this case solely by the temperature of the helium. A heater on the inside of a Lavastone cavity, therefore, increases the mechanical pressure of the liquid helium. Our pumps have glass tubing leading the helium to the destinations. The end of each tube is drawn into a nozzle to inhibit gas flow. If this is not done, the helium evaporates from and cools the Lavastone chamber so that it does not work. Metal tubing was tested but abandoned because its thermal conductivity was too large. A pump connecting a warm location with the bath can conduct enough heat to

Reproduced with permission of the copyright owner. Further reproduction prohibited without permission.

run itself if it is made of metal.

The two pumps are used to fill the copper box around the spectrometer and to cool the top of the copper antenna cone. Each requires a power of less than 0.1 watt to pump 3 liters per hour.

The level of the liquid helium is measured by two level sensors made by American Magnetics, Inc. They are fine superconducting wires of Nb-Ti alloy. When biased with sufficient current, the wire stays normal when in gaseous helium, although it is still superconducting when in liquid helium. The resistance of the wire is thus a measure of the helium level.

The level of liquid nitrogen is measured by 1/8 W, 1.5 kΩ carbon radio resistors. When biased with a power comparable to this rating, they heat up noticeably more in gaseous nitrogen than they do in liquid nitrogen. As they are temperature-dependent resistors, the resistance affords an indication of the presence of liquid.

e. Liquid Helium Lifetime. Helium hold time is a major design problem. It is necessary to maintain a cold antenna a short distance from the warm outside world, without vacuum insulation. The major estimated heat inputs to the helium chamber are (1) gaseous conduction through the styrofoam plug in the top of the dewar, 6W; (2) gas conduction down the antenna horn, 1 W; (3) metallic conduction in the horn, 3 W; (4) direct radiation into the antenna, <1 W; and (5) radiation to the dewar wall through the superinsulation and heat shields, <1 W. Items (1) and (2) are estimated from the thermal conductance of helium gas, $k = 2 \times 10^{-5} T^{3/4}$ W/cm deg (Chelton and Mann, 1956). Item (3) is obtained from the conductivity of copper, 4 W/cm deg at room temperature.

Reproduced with permission of the copyright owner. Further reproduction prohibited without permission.

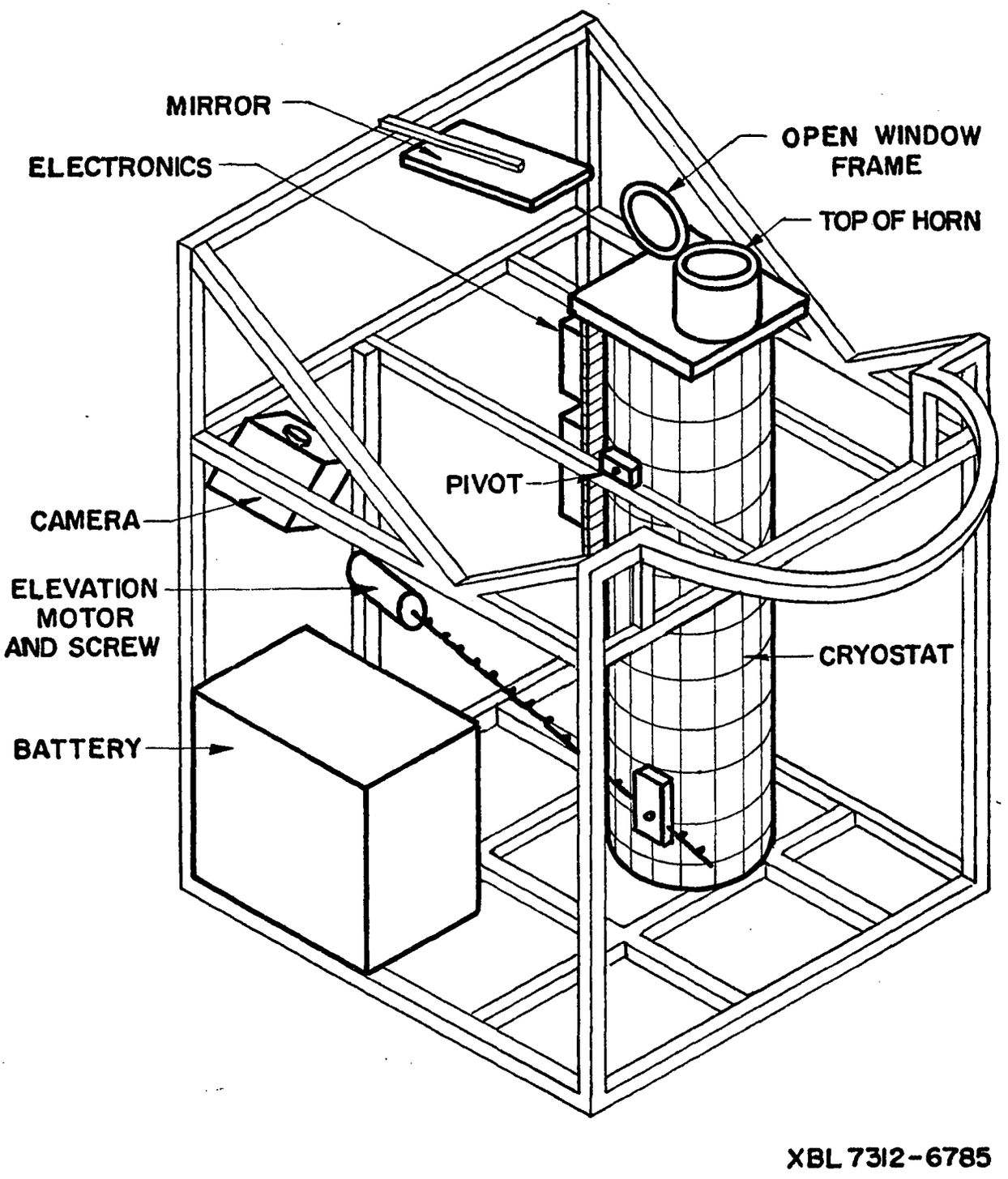

Fig. 15. Balloon gondola.

Reproduced with permission of the copyright owner. Further reproduction prohibited without permission.

The copper film dominates the conduction of the horn. Item (4) is not well known but it is probably small due to the multiple bounces the radiation makes, so that most of it is absorbed in warm parts of the cone. Item (5) is estimated from the loss rate of an empty dewar, 0.25 ℓ/hr.

The observed loss rate of the dewar with apparatus installed is about 2.5 ℓ/hr, enough to account for items (1), (4), and (5). The heat of vaporization is 84 J/mole, and its density of 36 mole/ℓ. In addition, we obtain cooling from the specific heat of the boiloff gas, which is (5/2) R = 21 J/mole deg. Under typical conditions, the gas warms from 1.5 K to 10 K just under the styrofoam. The net power absorbed by the helium is then 6.6 W.

The heat conducted and radiated down the horn is carried away by helium gas. The boiloff gas is directed either over the outside or up the inside of the horn, but in either case its temperature greatly increases as it absorbs the heat.

2. Balloon Gondola and Electronics

A drawing of the balloon payload is shown in Fig. 15. The framework is a modification of a pre-existing frame. It is a nearly rectangular structure, 120 cm × 120 cm × 155 cm high. The instrument in its cryostat is pivoted near the center of the volume, so that it can look out at different zenith angles. The total scanning range is out to 40° from the zenith in one direction and 25° from the zenith in the other direction. A nearly horizontal mirror is installed at the top of the gondola and a movie camera is in one corner, so that photographs of the dewar top can be made. These photographs show the inside of the antenna cone and are an important check on whether air condenses into the antenna.

Reproduced with permission of the copyright owner. Further reproduction prohibited without permission.

The electronics for this system were designed and built by J. Henry Primbsch and his assistants at the Space Sciences Laboratory in Berkeley. The telemetry devices for transmitting and receiving data and commands were all built for previous balloon experiments, as was the battery box. The system can transmit 12 command tones on a transmitter at about 138 MHz, giving a total of 40 different commands. This system is reliable because the small receiver bandwidth (1 Hz) allowed for each tone prevents response to other transmitters. The data are transmitted back from the balloon on a number of digitized analog channels. All the analog channels are digitized by the same eight-bit, 0-5V analog-to-digital converter. Two data channels are sampled 250 times per second, and they are used for the detector signal and for the phase reference signal generated by the rotating chopper shaft. Thirty-one channels are sampled every 0.064 second and are used mostly for thermometers and position readout potentiometers. One is subdivided into 16 subchannels, each of which is sampled for 2 sec out of every 32. These are used for housekeeping data like battery voltages, level indicators, and more thermometers. Another analog channel is used to transmit octal data numbers, recording the positions of two shaft encoders, the status of the camera and heaters, the preamplifier gain, and the command system state.

The electronics which are specific for this experiment are mounted on an aluminum sheet on the side of the cryostat. They include a special circuit which runs the interferometer stepper motor in a prearranged automatic sequence, a chopper motor driver, heater controls, helium level indicator power supplies, other stepper motor drives, and

Reproduced with permission of the copyright owner. Further reproduction prohibited without permission.

a low-noise gain-switched preamplifier for the detector.

The preamplifier uses the 2N4867A transistor in a circuit which provides rapid recovery from transients. The method used is to stabilize the DC operating point with a feedback loop. This feature has proven to be important because the detector produces electrical transients that are presumed to be of mechanical origin. Rechargeable Ni-Cd batteries provide a low impedance, low noise power supply so that even with a gain of 10^6 there is little feedback through the power supply.

The total power consumption of the entire balloon gondola is between 50 and 100 wats, depending on how many motors and heaters are running. About 10 watts are required for each motor and for the transmitter, and 10 watts are needed to run telemetry and command systems. The measured capacity of our battery is 1000 W-hr but this is reduced by low temperatures. The battery is made of about 45 kg of lead-acid gel storage cells. The battery is insulated by about 5 cm of Styrofoam to postpone the loss of heat.

C. Spectrometer Operation

Both our interferometer and the purpose to which we are putting it are somewhat novel, so we have developed our own techniques for adjustment and for computation. The adjustment is different from that which we use for our ordinary laboratory interferometer and the geometry is much more complex. The computations are unique because they involve measuring a continuous spectrum in the presence of an unresolvable series of line emissions from the atmosphere which can however be modeled.

Reproduced with permission of the copyright owner. Further reproduction prohibited without permission.

1. Aligning the Interferometer

As previously discussed, our interferometer has a beamsplitter and two corner reflectors to be aligned. The other parts of the interferometer are entirely uncritical as regards alignment. Each input plane wave produces four different plane waves at the output which must be accurately superposed to provide the interference that is the basis of the instrument. Each plane wave is divided into two at the beamsplitter, and at each corner reflector the wave is again divided, according to which half of the reflector is struck first. If the corner angle of the dihedral mirror is not precisely 90° then the two paths do not produce parallel rays coming back.

Our most effective method of alignment is visual. The mirrors are of solid aluminum and are given a moderate polish, as previously described. The beamsplitter is of no use for visible light but a plane-parallel glass plate can be used as a substitute, merely by pressing it against the plane which holds the wires. The first step is to set the corners to right angles. The setup in Fig. 16 is used. The target is a perforated brass sheet illuminated from the back by a lamp. First a plane mirror is placed at M and the telescope is focused on the target. Then the plane mirror is replaced by the corner mirror and its angle is adjusted until the two images seen in the telescope are superimposed. The telescope has a large enough aperture (50 mm) to view the entire corner mirror, and a large enough magnification (25×) that the entire ray bundle can fit into the pupil of the eye. It is necessary to use the entire area of the mirrors because they are not perfectly flat, and we want to form the correct average. The telescope is prefocused for

Reproduced with permission of the copyright owner. Further reproduction prohibited without permission.

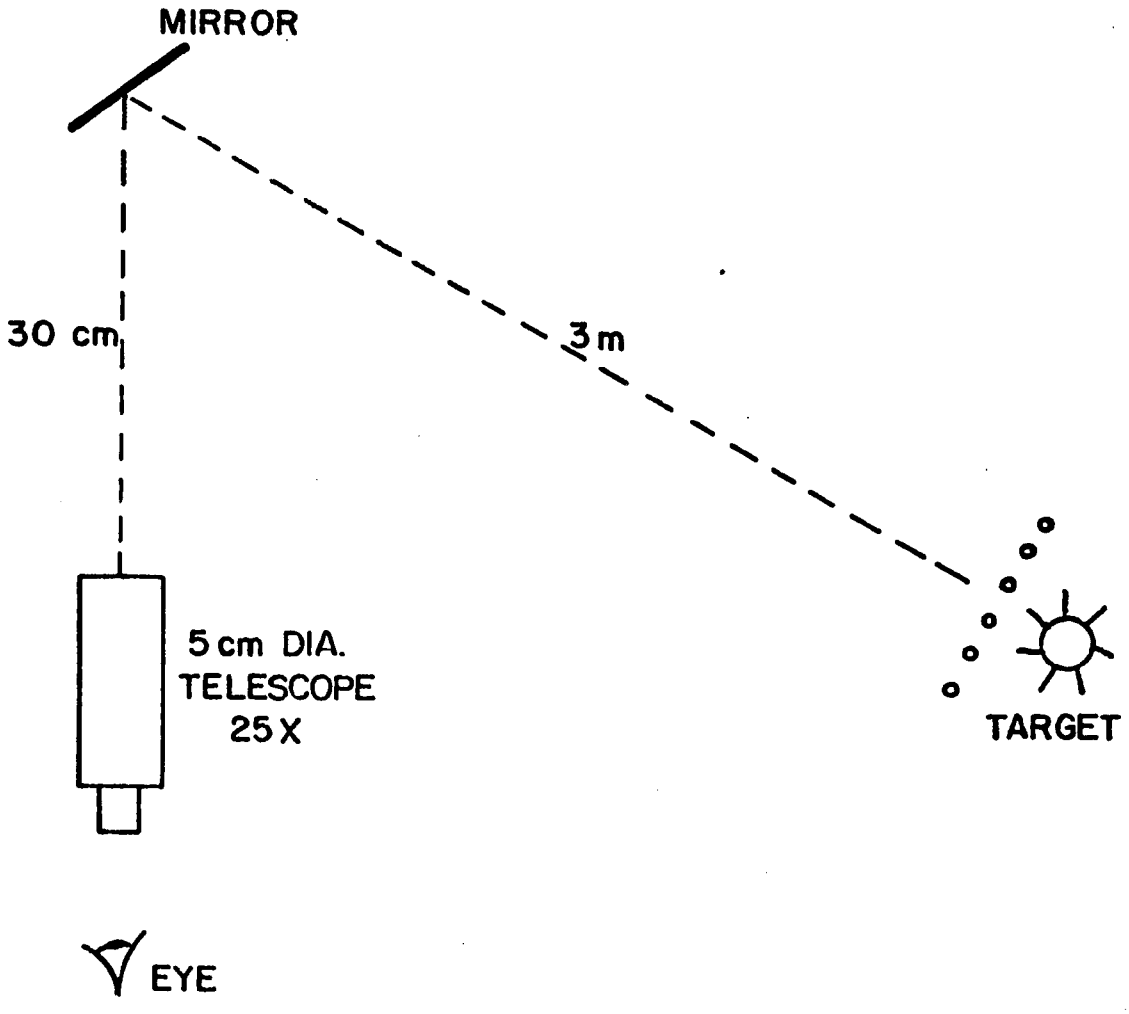

Fig. 16. Corner mirror alignment.

Reproduced with permission of the copyright owner. Further reproduction prohibited without permission.

the same reason.

Then the two corners are aligned relative to the beamsplitter. The first step is to align the vertex lines of the dihedral mirrors at an angle of 45° to the direction of polarization of the beamsplitter. The method is to look through the beamsplitter at the corner mirror and the image which it forms of the beamsplitter. When correctly aligned, the images of the beamsplitter wires are perpendicular to the wires themselves.

The final alignment is made using the glass beamsplitter pressed against the wire one, as shown in Fig. 17. The telescope looks through the interferometer at a distant target. It is prefocused using the measured total optical path including all the bounces in the interferometer. Both corner mirrors can be rotated about their optic axes slightly, and there is one tilt adjustment. If the preceding adjustments have been accurately made, only the tilt adjustment need be used to superimpose the two images seen in the telescope. The target is a two-dimensional pattern so that it is possible to examine all parts of the field of view simultaneously. It is necessary to have the target at a great distance to avoid confusion with the extra sets of images that arise from the two-sided glass beamsplitter. In the limit of infinite target distance all the images are superposed.

These adjustments arrange that parallel ray bundles entering the interferometer will be able to interfere at the output. It is important that the interference be able to occur at all points in the field of view. If the corner mirrors are not correctly installed, then adjustment can be obtained at only one point in the field of view. For example,

Reproduced with permission of the copyright owner. Further reproduction prohibited without permission.

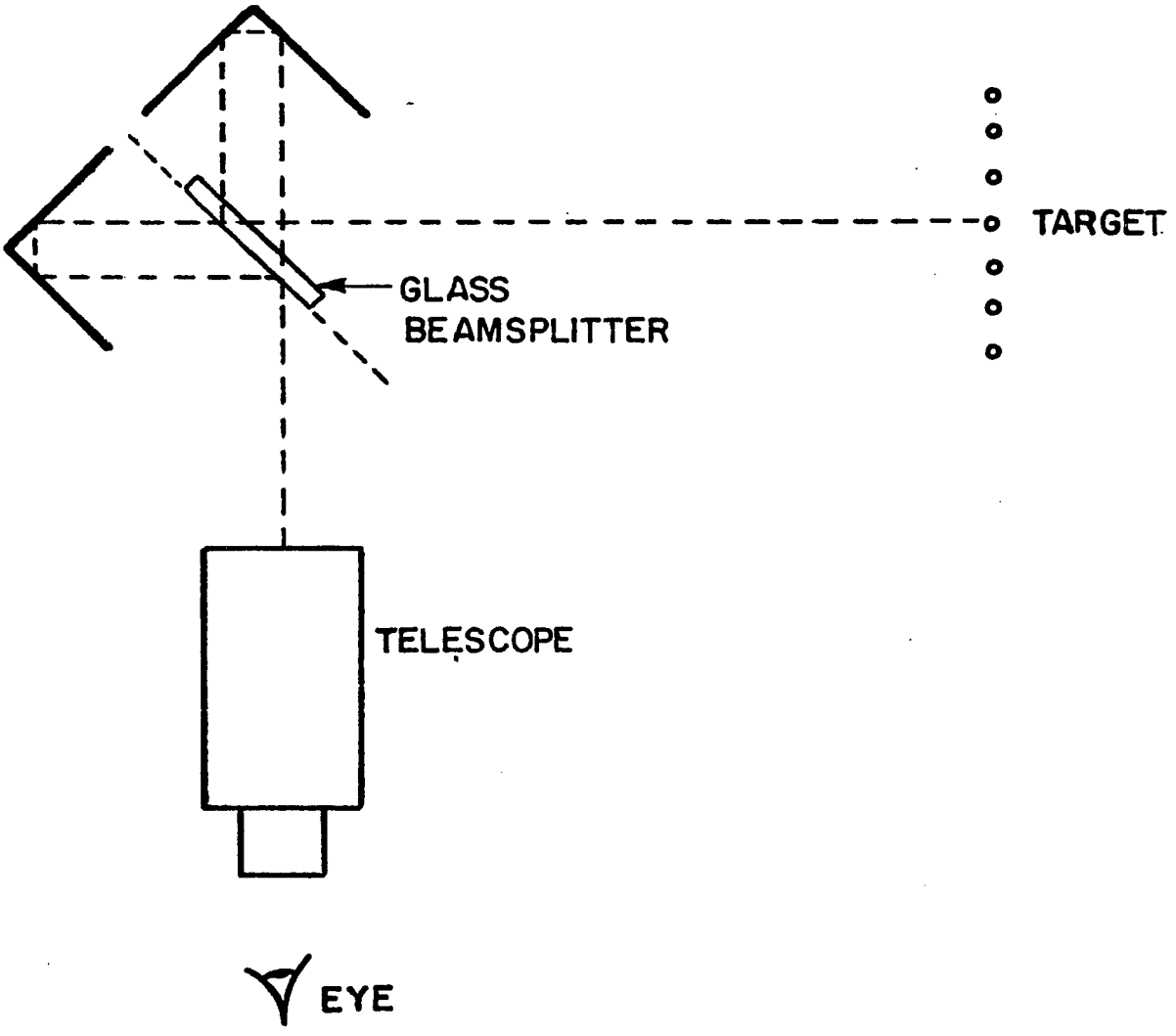

XBL 7312-6787

Fig. 17. Alignment of the polarizing Michelson interferometer.

Reproduced with permission of the copyright owner. Further reproduction prohibited without permission.

there are two ways in which to satisfy the orientation of the corner mirror relative to the polarization direction of the beamsplitter. Either is acceptable but both mirrors must be done the same way. When the glass beamsplitter is present one should be able to see the reflected image of one corner mirror superimposed on the direct image of the other. For this to be so, the vertex lines of the corner mirrors must intersect, and the plane of the beamsplitter must bisect the angle between them, or should at least be parallel to such a plane.

The alignment discrepancy must be small compared to the diffraction angle $\theta = 1.22\ \lambda/d$, where λ is the wavelength of interest and d is the diameter of the optics, about 6 cm. For a wavelength of 0.02 cm, this angle is 4 mrad, which is easily visible in the 25× telescope. If the beams are not aligned this well, they do not overlap enough to interfere.

As with the Fabry-Perot interferometer, the frequency resolution is limited by the solid angle passing through the interferometer. In fact, the same formula applies: $\nu/\Delta\nu \leq 2\pi/\Omega$.

Unlike the Fabry-Perot interferometer, the PMI does not require especially flat surfaces. What it requires instead is precisely parallel translation of the moving mirror. The resulting spectrum is accurate to a limit set by the precision of motion of the moving mirror. If the resulting spectrum is to be accurate to within 1% of the peak signal strength, then the mirror must be set to within about $0.01\ \lambda/2\pi$, where λ is the predominant wavelength observed. For our case, λ is about 0.07 cm, and the required precision is about 10^{-4} cm, quite comparable to the setting needed for the Fabry-Perot interferometer.

Reproduced with permission of the copyright owner. Further reproduction prohibited without permission.

Our drive mechanism is not of optimal design for precision photometry and is under review. The moving mirror can wobble up to about 2 mrad if it is not sprung or weighted to avoid transverse motion. This motion occurs because the micrometer screw is part of the alignment mechanism and it must be loosely set so that it will not squeak. Tests in the laboratory show that successive measurements of the same interferogram have random variations with a standard deviation of about 1% of the signal strength. Fourier transforms of these test interferograms show false energy (ghosts) of the order of 3% of the maximum signal level. Ghosts can be recognized easily where it is known for other reasons that there is no signal energy.

2. Calibration

Our spectrometer is a linear device with a single adjustable coordinate, the path difference x. With it we desire to measure the spectral intensity $F(\nu)$ of some source. There are two functions needed to describe this kind of system. The first is the zero level $F_o(\nu)$ as a function of frequency. This is the spectral intensity which must be supplied to the instrument in order to produce a zero output for all values of x. We desire that this value $F_o(\nu)$ be small compared to the spectrum to be measured, and it should be accurately known. If our spectrometer is working correctly, $F_o(\nu)$ is the black body emission spectrum for the temperature of the helium bath in which the spectrometer is immersed. Experimentally we verify this statement by supplying such a black body in either of two ways. The first way is to rotate the diagonal mirror so that the spectrometer looks downwards at an Eccosorb cone immersed in the liquid helium. The second way is to

Reproduced with permission of the copyright owner. Further reproduction prohibited without permission.

slide a cone of Eccosorb down the antenna cone until it fills the beam and is immersed in liquid helium too.

These bodies should produce zero output for all x because the spectrometer cavity is isothermal. Therefore, no radiation gradients can exist to be chopped by the chopper and produce signals at the detector. The detector temperature of 2.2K is slightly higher than the bath temperature of 1.6K, but no effects of this difference have been observed with either cold black body.

The second function to be determined is the transmission function of the instrument for general ν and x. As it happens, this function is simple for the Fourier spectrometer. It is

$$t_2(\nu,x) = t_1(\nu) \cos(2\pi\nu x + \phi(\nu)) \quad , \tag{20}$$

where $t_1(\nu)$ and $\phi(\nu)$ are functions of ν only. When this expression is integrated over frequency, an expression for the interferogram is obtained:

$$I(x) = \int_0^\infty [F(\nu) - F_o(\nu)]\, t_1(\nu) \cos(2\pi\nu x + \phi(\nu))\, d\nu \, . \tag{21}$$

To use the spectrometer one observes the function I(x) at a variety of points x and solves this integral equation for $[F(\nu) - F_o(\nu)]\, t_1(\nu)$ and for $\phi(\nu)$. The method of solution is ordinarily the Fourier Transform discussed at some length in Section IV. The result is that because of the special properties of the kernel $\cos(2\pi\nu x + \phi(\nu))$, the solution is very simple. One defines

$$G(\nu) = \int_{-\infty}^{\infty} I(x)\, e^{-2\pi i\nu x}\, dx \quad ,$$

Reproduced with permission of the copyright owner. Further reproduction prohibited without permission.

from which follow the desired results

$$S(\nu) = [F(\nu) - F_o(\nu)]\, t_1(\nu) = 2|G(\nu)| \quad ,$$

and

$$\phi(\nu) = \arg(G(\nu)) \quad .$$

Approximations to the integral for $G(\nu)$ are usually made by sampling $I(x)$ at a regularly spaced set of points and then performing a discrete sum. Providing enough samples are measured, the sum gives a good approximation.

Typical experimental results for a spectrum $S(\nu)$ and a phase function $\phi(\nu)$ are shown in Fig. 18. For this set of data the source was a room temperature Lucite plate 1.27 cm thick covering the top of the horn. This material is a good black body. The function $t_1(\nu)$ can be derived from $S(\nu)$ by dividing by $F(\nu)$, since $F_o(\nu)$ is negligible, and is also plotted. The bath was at 1.6K.

We also test our system with low temperature black bodies. A light pipe 1.27 cm in diameter is inserted into the copper cone antenna, making contact about 12 cm from the small end. A tight-fitting conical black body of Eccosorb slides inside this light pipe, so that its temperature can be varied from the bath temperature up to room temperature. The results of a test with a black body at 4K are given as curve (d) of Fig. 18. This curve is the ratio of $S(\nu)$ for a 4K body to $S(\nu)$ for a 300K body. The transmission factor $t_1(\nu)$ cancels out, so this curve should be the ratio of black body intensities. The theoretical ratio has the simple form

Reproduced with permission of the copyright owner. Further reproduction prohibited without permission.

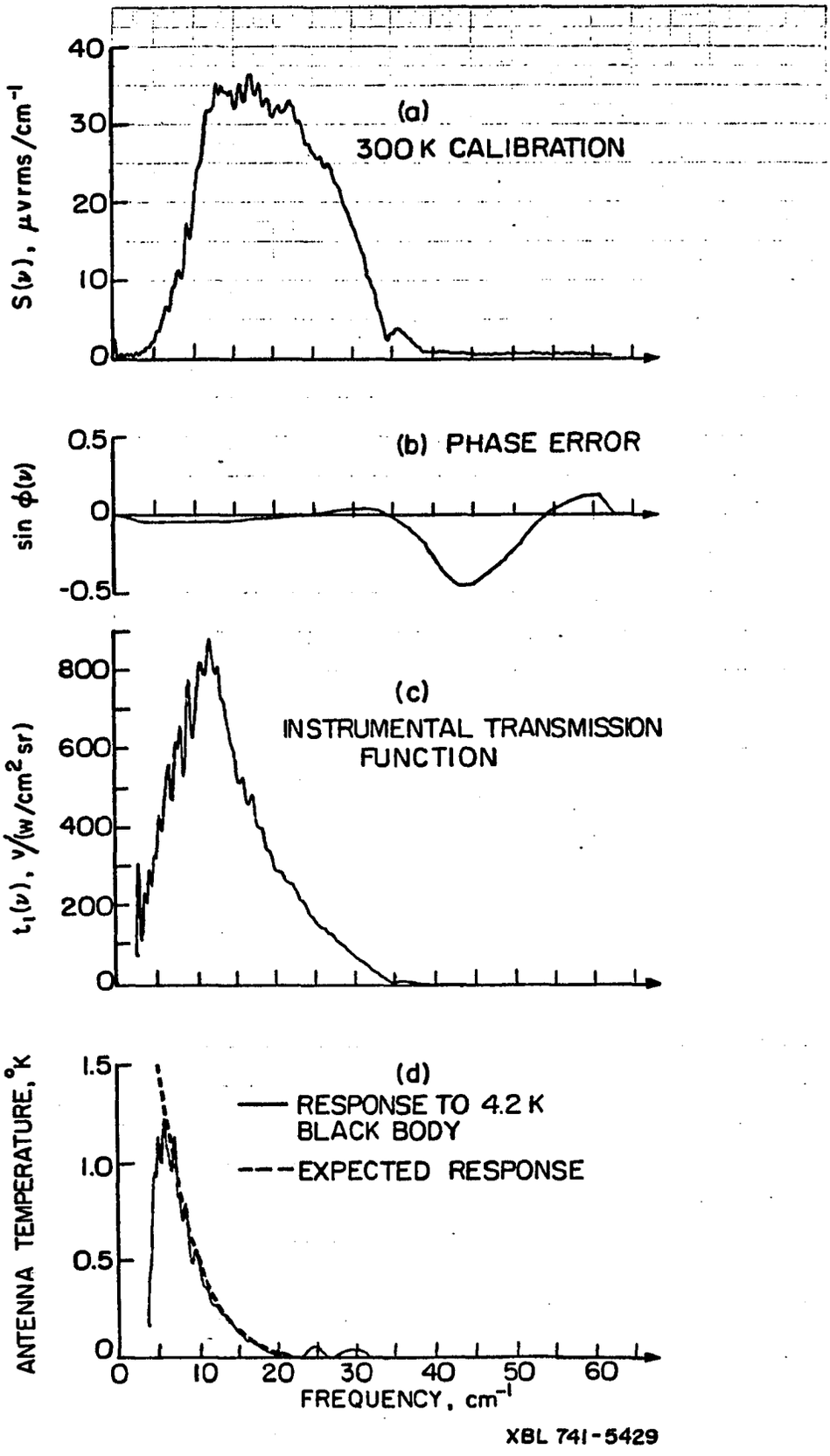

Fig. 18. Spectrometer calibration.

Reproduced with permission of the copyright owner. Further reproduction prohibited without permission.

$$F_T(\nu)/F_{T'}(\nu) = (\exp(h\nu c/kT') - 1)/(\exp(h\nu c/kT) - 1) \quad , \qquad (22)$$

which is also plotted in the figure. This function is the ratio of mean occupation numbers of the eigenmodes of the radiation fields, as given by Bose-Einstein statistics.

The calibration curves $t_1(\nu)$ and $\phi(\nu)$ tell us how well our instrument is working. The function $t_1(\nu)$ shows the effects of detector transparency at low frequencies, and the combined effects of the low pass Fluorogold filter and the beamsplitter efficiency rolloff at high frequency. The function $\phi(\nu)$ shows a bump at low frequency, a straight line section at intermediate frequencies, and a pronounced oscillation at high frequencies. These features are all reproducible. The straight line section corresponds to an ideal interferometer with the coordinate x measured from the wrong origin. Neither of the other effects is understood, but they may be related to the mirror wobble.

3. Observational Strategy

Because of the complexity of the interpretation of phase corrections and because our spectra contain unresolvable atmospheric lines, we are planning to avoid the method of Fourier transforms altogether. We will fit models with small numbers of parameters directly to our observed interferograms. The difference between the observed and fitted interferograms will then be Fourier transformed and studied. Since the effect of large, known emissions are already removed, problems of phase correction and resolution of lines are minimized. It is believed that this procedure can extract the maximum amount of information from the observations.

Reproduced with permission of the copyright owner. Further reproduction prohibited without permission.

As described in Section D below, models have been constructed for all the known sources of emission into the spectrometer. The synthetic interferogram which is adjusted to fit the observations is derived by numerically evaluating the integral

$$I(x) = \int_0^\infty [F(\nu) - F_o(\nu)]\, t_1(\nu)\, \cos(2\pi\nu x + \phi(\nu))\, d\nu \,. \quad (23)$$

The function $F(\nu)$ is a function of the model parameters, while $t_1(\nu)$ and $\phi(\nu)$ are known calibration functions. For the simplest form, we model $F(\nu)$ by a sum of only three terms: the emissions from a 2.7K black body, from water vapor, and from ozone. If the temperature of the atmosphere is assumed, there are only two unknown parameters needed to calculate its emissions, namely the numbers of molecules of ozone and water in the line of sight. All the rest are known from direct observation. In a slightly more general case, we can replace the 2.7K black body with a gray body, characterized by an emissivity and a color temperature, and fit these parameters to the interferogram as well.

We have made estimates of how well these four parameters can be simultaneously determined from a noisy interferogram. The theory of least squares fitting yields a correlation matrix for the noise on the fitted parameters. This matrix is derived from the properties of the model and the values of the fitted parameters. To find the actual noise on a fitted parameter, one needs to estimate of the noise on the original interferogram. If the model is an adequate model, the residuals of the fit give a noise level comparable to the random noise coming from the detector when the interferometer is not scanning. The resulting estimates are presented in Table VI for measured detector noise and an observing time of 1 hr.

Reproduced with permission of the copyright owner. Further reproduction prohibited without permission.

Table VI. Estimated noise in data fitting.

		rms Fractional Noise	
Parameter	Fitted Value	L = 1/2 cm $\Delta\nu$ = 1 cm^{-1}	L = 1 cm $\Delta\nu$ = 1/2 cm^{-1}
n_{H_2O}	3×10^{17} cm^{-2}	0.009	0.009
n_{O_3}	3×10^{17} cm^{-2}	0.007	0.0085
T gray body	2.7K	0.02	0.03
ε gray body	1.0	0.07	0.13

Total Observing time: 1 hr.
Measured detector noise only.

Reproduced with permission of the copyright owner. Further reproduction prohibited without permission.

The important feature about this table is that it demonstrates that the molecules are not measured better with higher resolution. However, the total emission from the gray body, given by the parameter ε, is only half as well determined when the resolution is improved by a factor of two. This result is in direct agreement with the noise analysis given in Section IV-D. It is curious that $\Delta T/T$ is only a fourth as large as $\Delta\varepsilon/\varepsilon$. The explanation of this is that we are observing almost the entire power emitted by the gray body, which is proportional to T^4.

It is thus seen that high resolution is unnecessary to observe the atmospheric line emissions. It is only necessary to observe the interferograms to give the resolution we wish to have on whatever discrepancies we are looking for. If the discrepancy with the model is localized in frequency with a width $\Delta\nu$, then we should run the interferometer to give just that resolution.

D. Models for Emissions Into the Radiometer

Essentially every item in the optical train of our apparatus must be considered as a source of radiation. The atmosphere, the earth, the balloon and rigging, the windows, the horn, and the antenna cone all emit radiation. They will be discussed in that order in the following sections. Estimates show that the atmosphere and the window (Teflon) have large and comparable contributions, while the other effects have been designed out. The atmosphere is measured by the spectrometer and by zenith angle scans. The window is measured by removing it. In principle, there could be two identical windows of which only one was removed. The difference signal would then estimate

Reproduced with permission of the copyright owner. Further reproduction prohibited without permission.

the correction for the remaining window. The horn and cone are checked by varying their temperatures. Earth, balloon and rigging are investigated by zenith angle scans. Figures 19 and 20 summarize the estimates of the next section.

1. Atmospheric Emissions

Rotating molecules in the atmosphere are the major source of radiation seen by our spectrometer. At our operating altitude, the atmosphere emits more than a 2.7K black body for frequencies above about 12 cm^{-1}. Water emits about ten lines in our region, some of which have optical depth much larger than unity. Ozone emits hundreds of lines spaced by tenths of cm^{-1}. Its lines are more closely spaced than those of water because it is larger and heavier and therefore rotates more slowly. The strongest ozone lines have optical depth near unity.

Both water and ozone emit by electric dipole transitions. Molecular oxygen also emits but by magnetic dipole transitions. In its ground electronic state there is a magnetic moment because there are two unpaired electrons. The ground state is split by a fine-structure interaction, which couples the electronic angular momentum to the molecular rotational angular momentum. Transitions between fine structure states give lines at 2 and 4 cm^{-1}. Transitions between different rotational states give lines at higher frequencies. These lines occur in triplets because of the fine structure. The first group is centered at 14 cm^{-1}.

Reproduced with permission of the copyright owner. Further reproduction prohibited without permission.

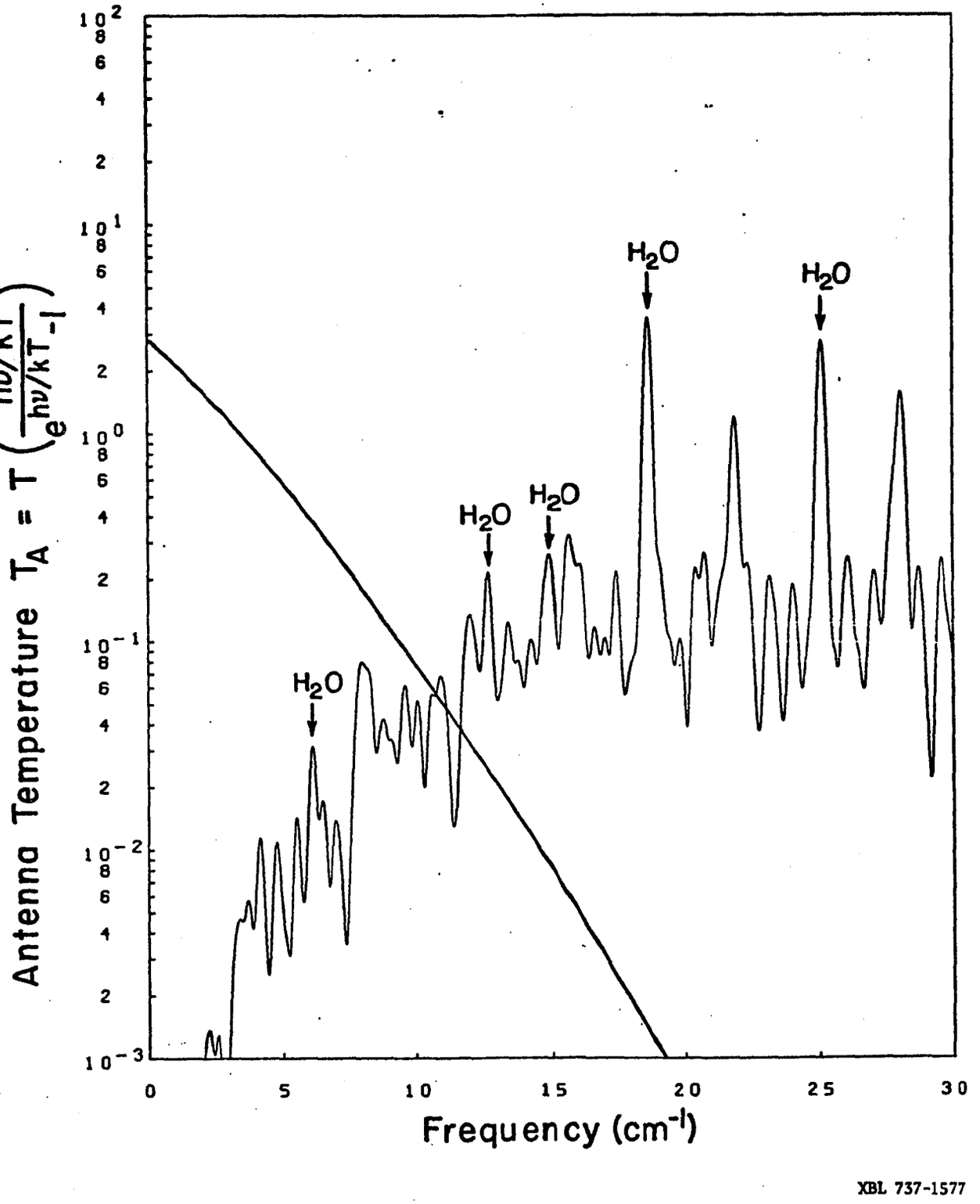

Fig. 19. Emission of water, ozone and a 2.7K black body.

Reproduced with permission of the copyright owner. Further reproduction prohibited without permission.

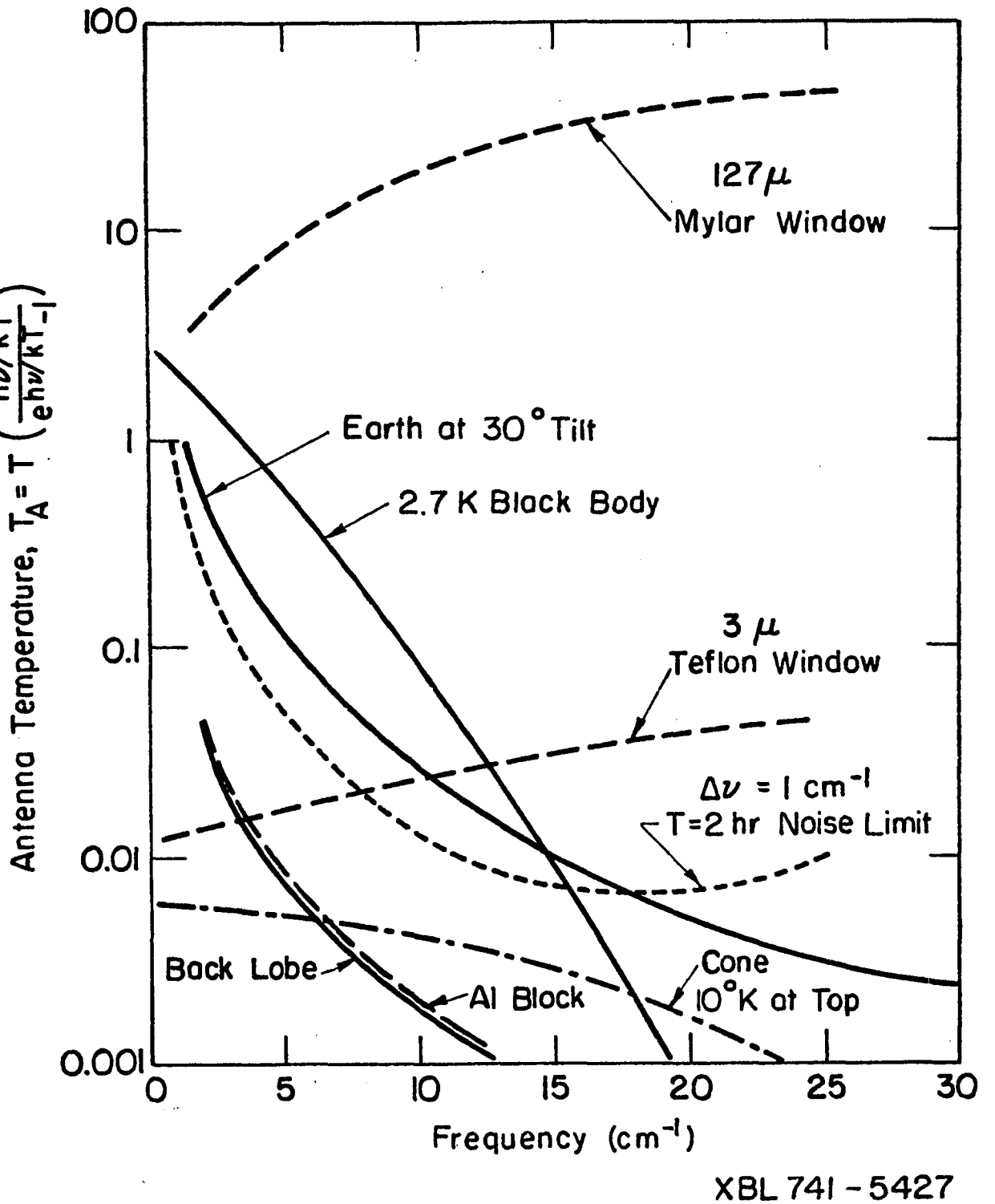

Fig. 20. Emission of continuum sources into radiometer.

Reproduced with permission of the copyright owner. Further reproduction prohibited without permission.

Figure 19 is a frequency plot of the effective antenna temperature of the emissions expected from ozone and water. The spectrum is portrayed with a Gaussian resolution function of standard deviation 0.125 cm^{-1}. The numbers of molecules are 3×10^{17} cm^{-2} for both ozone and water. Muehlner and Weiss (January 1973) found that these numbers were consistent with their observations.

The antenna temperature is defined as the temperature which, when used in the Rayleigh-Jeans black body formula for an object that fills the antenna beam, would produce the observed signal level. In terms of the spectral intensity F_ν ($W/cm^2 sr\ cm^{-1}$), the antenna temperature is

$$T_A = F_\nu / 2k\nu^2 c \quad , \tag{24}$$

where ν is the frequency in cm^{-1}. If a physical object at temperature T with emissivity ε fills a fraction f of the beam, then it produces an antenna temperature

$$T_A = T \cdot \varepsilon \cdot f \cdot (\eta / (e^\eta - 1)) \quad , \tag{25}$$

where $\eta = h\nu c/kT$.

The antenna temperature for a 2.7K black body is also plotted. For this curve $\eta = 1$ at only 1.88 cm^{-1}. This is the curve which we are attempting to measure. The plot shows that the difficulty of measurement increases rapidly with frequency.

Line strengths for ozone and water are calculated from the data of McClatchey, et al. (1973). The data are available on computer tape from them. The calculations involve the vibrational and rotational partition functions, and formulas are given by them to simplify this

Reproduced with permission of the copyright owner. Further reproduction prohibited without permission.

computation. The pressure-broadened linewidths are proportional to the pressure and the molecular velocity, and are typically of the order of 3×10^{-4} cm^{-1} = 9 MHz. Data for oxygen lines are given by Meeks and Lilley (1963) for the 2 and 4 cm^{-1} transitions and by Gebbie et al. (1969) for higher frequencies.

Proper accounting must be made for the effects of saturation of the line emissions. It is customary to assume the Lorentzian line shape

$$k(\nu) = (S\alpha/\pi)((\nu - \nu_o)^2 + \alpha^2)^{-1}, \tag{26}$$

where

$$S = \int k(\nu)\, d\nu \quad . \tag{27}$$

In this formula, $k(\nu)$ is the absorption coefficient per (molecule/cm^2) and can be interpreted as a molecular cross section. S is the line strength (cm^{-1}/molecule cm^{-2}), while α is the line width parameter, the half-width at half-maximum in cm^{-1}, and ν_o is the resonant frequency in cm^{-1}.

When radiation passes through an absorbing medium, it is attenuated exponentially. The negative logarithm of the transmission t through a portion of the medium is called the optical depth τ, so that $t = e^{-\tau}$, and the absorption is then $a = 1 - e^{-\tau}$. The optical depth may be found by an integration of the absorption coefficient along the ray path: $\tau = \int k\rho ds$, where k is the absorption coefficient, ρ is the number density of the molecules, and ds is an element of path length.

For line emissions, and especially when line shapes are unresolved, it is useful to define an equivalent linewidth A. This is the linewidth that a completely opaque absorber would have if it absorbed the same

Reproduced with permission of the copyright owner. Further reproduction prohibited without permission.

amount of energy from a continuous spectrum of energy incident on the medium. The fraction of light which the real line absorbs at each frequency is $1 - e^{-\tau(\nu)}$, so we define

$$A = \int (1 - e^{-\tau(\nu)})\, d\nu \tag{28}$$

We may then approximate our absorption function by $a = A\delta(\nu - \nu_o)$, where δ is the Dirac distribution.

By Kirchhoff's law of reciprocity, if the line absorber is at a temperature T, it is also an emitter according to

$$I_\nu = B_{bb}(\nu,T) \cdot A \quad , \tag{29}$$

where I is the integrated brightness of the line in W/cm^2sr, and $B_{bb}(\nu,T)$ is the spectral brightness of a black body at the temperature T and wavenumber ν. In these units,

$$B_{bb}(\nu,T) = 2kTc\nu^2(\eta/(e^\eta - 1)) \quad , \tag{30}$$

where

$$\eta = h\nu c/kT \quad . \tag{31}$$

For any of our atmospheric absorption-emission lines, we must perform integrals over space and frequency to obtain A. The simplest assumption is the isobaric, isothermal case, so that

$$k(\nu) = (S\alpha_o/\pi)((\nu - \nu_o)^2 + \alpha_o^2)^{-1}$$

with α_o a constant. Then

$$\tau(\nu) = \left(\frac{Su}{\pi\alpha_o}\right) \frac{\alpha_o^2}{(\nu - \nu_o)^2 + \alpha_o^2} \quad , \tag{32}$$

Reproduced with permission of the copyright owner. Further reproduction prohibited without permission.

where u is the total number of molecules per cm^2. I integrated the linewidth integral by parts, and identified the result as a confluent hypergeometric function. Applying identities for this function led to the formula

$$A = 2\pi\alpha_o y e^{-y}[J_o(iy) - iJ_1(iy)] \quad , \tag{33}$$

where $y = Su/2\pi\alpha_o = \tau_o/2$ defines y and τ_o. This verifies the statement of Muehlner and Weiss (January 1973).

The next more complicated system relaxes the isobaric condition but maintains a constant mixing ratio. To solve this problem, I set up formulas expressing the attenuation coefficient k and the number density ρ in terms of the pressure p. The integral for $\tau(\nu)$ turns out to be an elementary integral

$$\tau(\nu) = (\tau_o/2)\ \ell n\ (1 + (\alpha_o^2/(\nu - \nu_o)^2)) \tag{34}$$

where as before we define $\tau_o = Su/\pi\alpha_o$, and u is the number of molecules/ cm^2 in the line of sight. Here α_o is the parameter τ evaluated at the position of the spectrometer. It is important that τ_o is no longer the optical depth at the center of the line, which is infinite in this approximation. It is, however, the optical depth which would apply at line center if all the molecules were at the same pressure p_o, the pressure at the spectrometer.

Putting this result into the formula for A gives

$$A = \alpha_o \int_{-\infty}^{\infty} \left(1 - (1 + \frac{1}{\zeta^2})^{-\tau_o/2}\right) d\zeta \ , \tag{35}$$

where $\zeta = (\nu - \nu_o)/\alpha_o$.

Reproduced with permission of the copyright owner. Further reproduction prohibited without permission.

This I integrated by parts, changed variable to $\xi = 1/\zeta^2$, and obtained

$$A = \alpha_o \tau_o \int_{-\infty}^{\infty} (\xi)^{1/2} \, (1 + \xi)^{-1 - \tau_o/2} \, d\xi = \alpha_o \tau_o B\left(\frac{1}{2}, \frac{\tau_o}{2} + \frac{1}{2}\right) , \tag{36}$$

where this B is the Beta function defined by

$$B(x,y) = \Gamma(x) \, \Gamma(y)/\Gamma(x + y) \quad . \tag{37}$$

For unsaturated lines, the Beta function is approximately π, and the linewidth is $A = Su$ as expected. For large τ_o, the Stirling approximation shows that

$$A = \alpha_o \sqrt{2\pi\tau_o} = \sqrt{2Su\alpha_o} \quad . \tag{38}$$

For computational purposes the B function with one argument fixed at 1/2 is easily evaluated with an expansion around infinity. A recursion relation is used to increase the argument so that the expansion around infinity is good, even for small τ_o.

A synthetic interferogram is now easily generated to fit to observations. First, the effective linewidths are computed from number densities, assumed average temperature, and measured pressure. These are multiplied by the black body intensity and the measured gain of the interferometer at the appropriate frequencies. Then phase-shifted cosines are calculated from the known instrumental phase function $\phi(\nu)$, and the products of all these factors are summed over all the known atmospheric lines.

If good fits cannot be obtained, we may need to construct a model which takes explicit account of the temperature profile of the atmosphere.

Reproduced with permission of the copyright owner. Further reproduction prohibited without permission.

2. Measurement of Antenna Pattern

Warm objects emit vastly more radiation in the far-infrared than does a 2.7K body. At 18 cm^{-1}, a 300K body emits more than 10^5 as much as a 2.7K body. Our antenna must reject radiation from the following warm bodies: a balloon (mostly transparent, slightly reflective, and very large); the rope, parachute, support cables, and spreader bar suspending the gondola; and the gondola and the earth which fill the back lobe of the antenna and part of the front lobe of the antenna.

As previously described, our antenna is a long, thin reflecting cone, with a shorter and steeper horn at the large end. This design has the advantages that it

(a) does not suffer from local stray light, being totally enclosed,

(b) places no dielectric surfaces in the beam which could otherwise reflect several percent of the radiation from undesired directions into our beam,

(c) has no solid objects obstructing and diffracting the beam,

(d) has well-understood geometrical and wave optics, and

(e) has calculable losses and emissions.

To understand the diffraction of the incoming waves into our antenna, we consider the time-reversed situation. Imagine that the detector is replaced by a source, and the source by a moveable detector. There is now a spherical wave going up the inside of the cone. This wave diffracts at the abrupt change in boundary conditions where the long cone ends and the horn begins. Radiation diffracted at small angles does not interact with the horn, but rays at larger angles strike the horn and are redirected into the forward direction. By

Reproduced with permission of the copyright owner. Further reproduction prohibited without permission.

geometrical optics, using the image-ball construction given in Section II-B-7, no rays from the cone-horn junction can leave the horn at more than 37° from the axis.

To verify that this construction works to reduce the effects of diffraction, we measured the response pattern of the antenna. The most obvious method of measurement is to move a chopped point source of radiation about in the field of view. We did this, using a mercury-arc lamp as a black body at 1000K, two glass liquid nitrogen vessels at 77K, a klystron generating several mW of power at 2.5 cm^{-1}, and a diode harmonic generator producing a few microwatts at 5 cm^{-1}, 7.5 cm^{-1}, and higher harmonics. With these sources the angular response pattern can be measured at angles up to about 20° off axis. Except for the fundamental klystron measurements, the signal is too small to measure at larger angles, even with our best detectors. With the klystron, the problem is the opposite, in that the detector responds to leakage through other paths, masking the desired signal.

Despite the difficulty of measuring responses at large angles, extrapolations and diffraction calculations indicate that they are very important. Hence, we undertook to measure our antenna pattern at much larger angles. The device shown in Fig. 21 was used to measure at angles up to 70° off axis. It utilizes the axial symmetry of the antenna to produce a source with large solid angle. The reflection of the rays from the source on the inside of a barrel-shaped reflector produces a ring-shaped image as described in more detail below.

Reproduced with permission of the copyright owner. Further reproduction prohibited without permission.

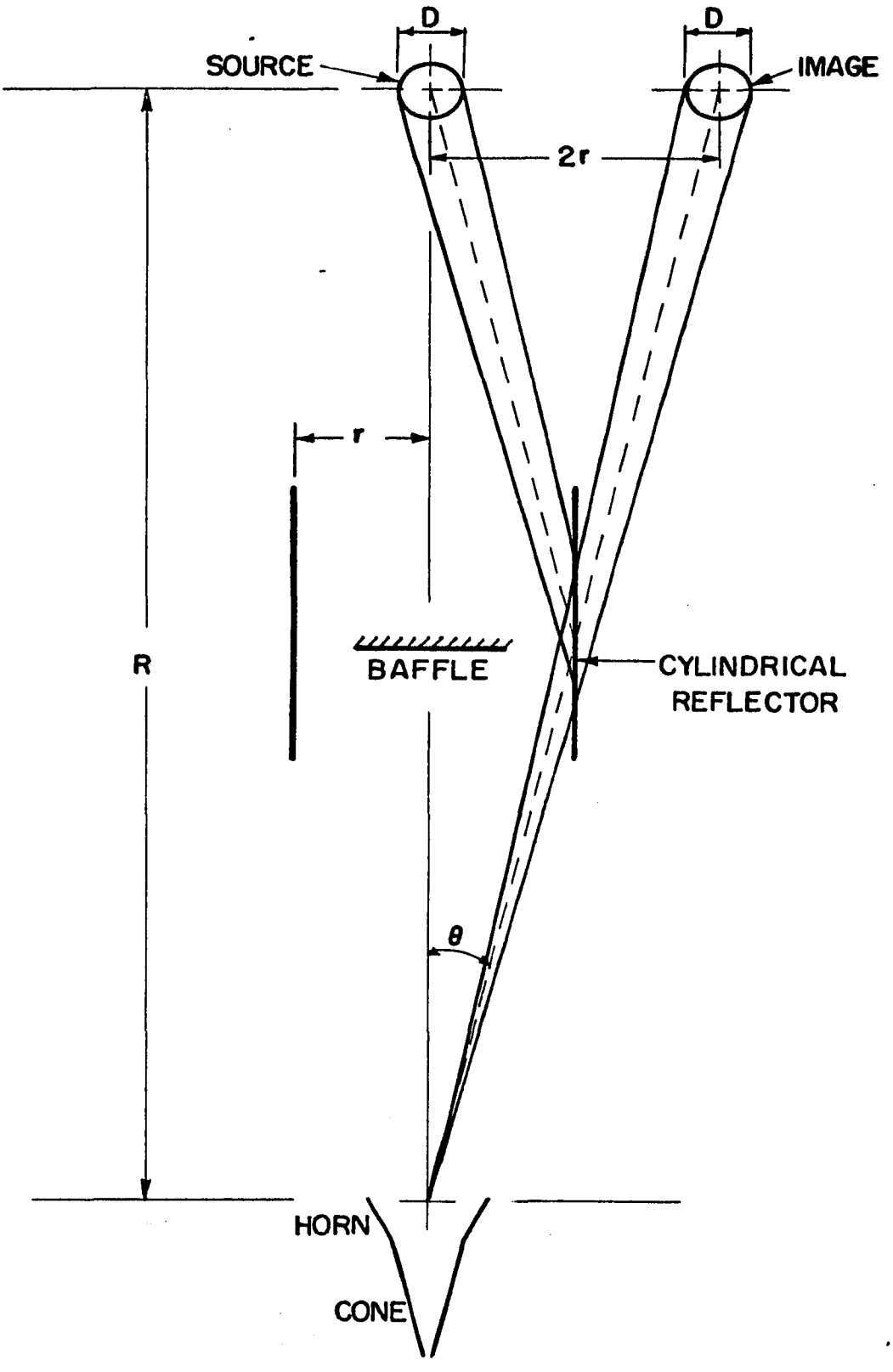

Fig. 21. Antenna measuring system.

Reproduced with permission of the copyright owner. Further reproduction prohibited without permission.

The actual source used is another thermal source, this time a liquid-nitrogen filled beaker. It is of glass, which is a good absorber at these frequencies, and is a right circular cylinder 15 cm in diameter and 15 cm tall. It is surrounded by several layers of polyethylene bubble sheet, a common packing material, which is a thermal insulator and is nearly transparent in the far-infrared. The radiation from this source is chopped by a drum which rotates on an axis passing through the center of the beaker. Half of the drum is metal and the other half is polyethylene film. The nitrogen gas boiling from the beaker is contained within the drum and prevents condensation of water onto the cold black body. A liquid nitrogen fill tube leads to the beaker through one bearing of the drum.

This source of radiation is located on the axis of the antenna. For normalization of the gain of the system, the source is brought close to the antanna so that it fills the beam. For measurement at large angles from the axis, a baffle intercepts the direct radiation from the source while a cylindrical reflector produces a ring-shaped image of the source. This image is located at an angle $\theta = \arctan(2r/R)$, where r is the radius of the reflector and R is the distance from the source to the antenna. The width of the image is the angle $\Delta\theta = D\cos\theta/R$, where D is the diameter of the beaker. The solid angle of the ring image is now

$$\Omega = 2\pi\sin\theta\Delta\theta = 2\pi \frac{D}{R} \sin^2\theta \quad . \tag{39}$$

An additional factor of $\cos\theta$ is used to estimate the effect of the chopper drum, since it has a different effective phase angle for rays that do

Reproduced with permission of the copyright owner. Further reproduction prohibited without permission.

not travel along the optical axis. Then

$$\Omega_{eff} = 2\pi(D/R)\ \sin^2\theta\ \cos\theta \quad . \tag{40}$$

For our case, we have D/R = 1/7, so that at $\theta = 60°$, $\Omega_{eff} = 0.34$ sr.

The large solid angle of this source permits rapid measurements at large angles. The results it gives are upper limits to the desired response curve because there is another path for the radiation that is important. Energy which is rejected by the antenna or reflected from its surroundings returns to strike the baffle, and a small fraction of this returns to the antenna at angles where it is sensitive. At angles of 60° and larger, the choice of material for blackening the baffle is very important. Our choice is a soft, multicolored polyurethane foam used as a packing material.

The results of our measurements are given in Fig. 22. The curve NEW shows the present state of the antenna. The curve OLD shows the performance of its predecesor, which had no long cone and collimator, but only a straight 6 cm pipe running from the horn down to the diagonal mirror and spectrometer. The mean wavelength used for the observations is about 0.07 cm. The function plotted is labeled I, which is not to be confused with the interferogram function I(x). As previously mentioned, the normalization integral $\int I d\Omega$ is found by simply filling the antenna with the source. The meaning of the plotted quantity is very simple. If an object in the field of view is at an angle θ off axis and subtends a solid angle Ω, then it fills an effective fraction of the beam $f = \Omega I(\theta)$. The pattern at small angles agrees well with the geometric optics calculations described below, with beam

Reproduced with permission of the copyright owner. Further reproduction prohibited without permission.

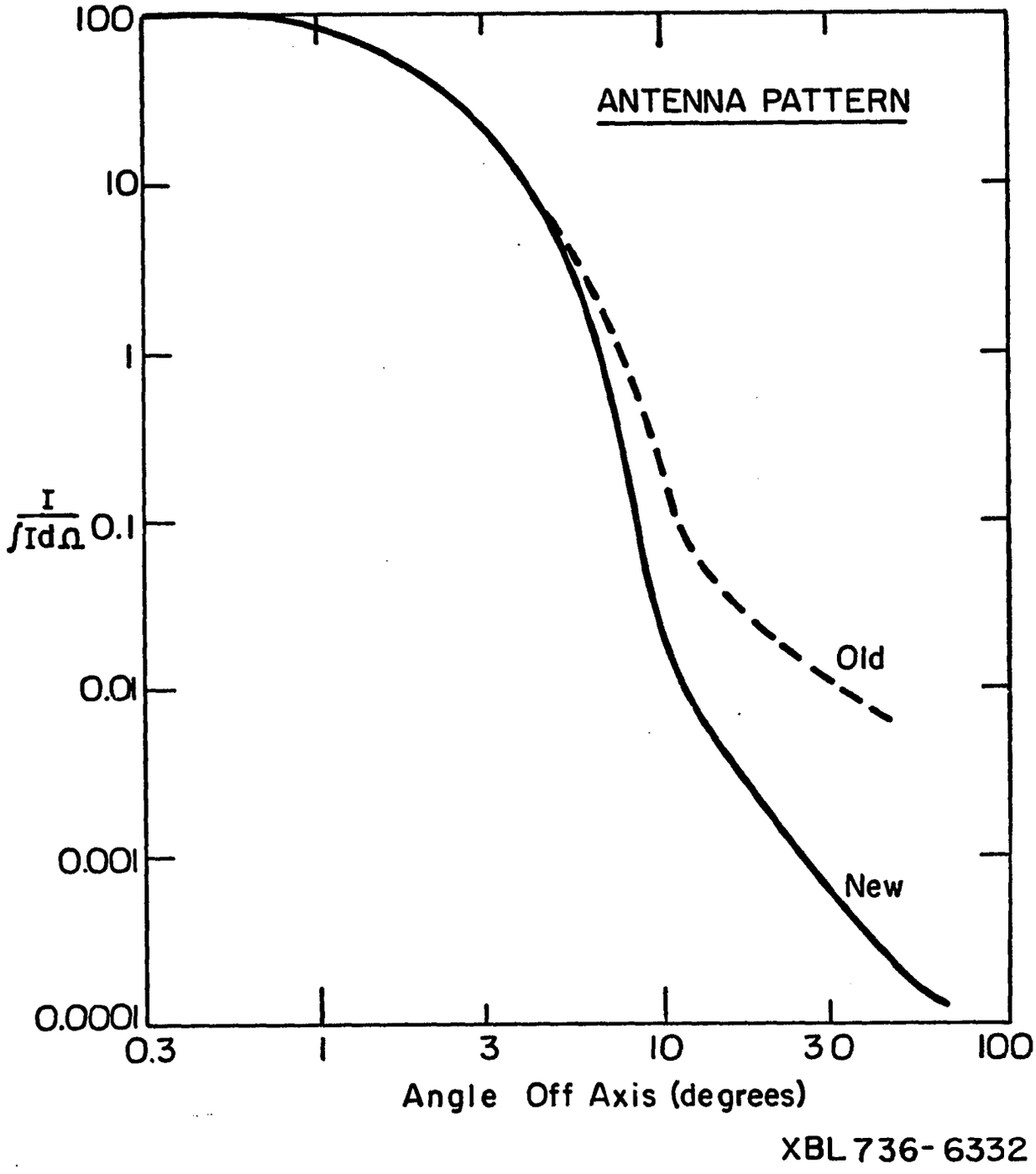

Fig. 22. Antenna pattern.

Reproduced with permission of the copyright owner. Further reproduction prohibited without permission.

divergence 7.6°, together with diffraction through a 6 cm hole. At 30° the pattern is similar to that caused by diffraction through a 30 cm aperture, showing the effect of the horn in improving the pattern.

We did not measure the general frequency dependence of this response pattern. For a plane wave diffracting once through a hole at a large angles, theoretical diffracted intensities are proportional to wavelength under rather general conditions. In the absence of direct data we use this hypothesis. For frequencies lower than about 3 cm^{-1}, we expect this approximation to break down, as the antenna transmits only a few eigenmodes. At 2.5 cm^{-1}, the pattern measured with the klystron was actually better at 30° than the pattern measured at 16 cm^{-1}, the mean frequency for the black body source and detector combination.

3. Diffraction Calculations

Approximate agreement has been found between the antenna pattern measurements just described and the diffraction calculations described below. The calculations must be made because some important questions are not accessible to direct measurements.

As previously mentioned, we consider theoretically the time-reversed case. A source of radiation is located at the bottom of the long conical antenna. A spherical wave travels up the cone and out the horn. As the radiation passes by the junction between cone and horn, it is diffracted. The horn redirects this diffracted radiation in the forward direction. A small fraction of the beam diffracts again at the top edge of the horn, and is responsible for the radiation diffracted at angles greater than 38°.

Reproduced with permission of the copyright owner. Further reproduction prohibited without permission.

The geometrical optics of the cone are simple. It is 70 cm long, 6 cm in diameter at the top end, and 0.3 cm in diameter at the bottom. The cone half angle is then 0.041 radians = 2.3°. The image ball is constructed as described in Section II-B-7 to describe the effect of multiple reflections in the cone. The image ball is 7.4 cm in diameter, giving a beam divergence at a point at the top of the cone of 0.105 radians = 6°, and a solid angle of 0.0083 sr, for an $A\Omega$ product of 0.23 cm^2sr. At the bottom the effective solid angle is π sr, so that $A\Omega$ is 0.22 cm^2sr, confirming the construction of the image ball.

The far-field beam divergence is larger than 6° because each point on the image ball emits a spherical wave with a divergence set by the cone angle of 4.6°. The antenna is not in focus for infinity. The r.m.s. beam divergences add quadratically so the effective beam diameter is 7.6°, although the extreme ray allowed by the geometry is 5.8° off axis.

The horn has a similar construction. It is 25 cm long and goes from 15 cm to 6 cm in diameter. Its image ball is larger than its aperture, being 34 cm in diameter. The resulting extremal ray is about 37° off axis. This means that radiation diffracted at the cone mouth is reflected in the horn so that none of it can escape at more than 37° from the axis.

a. Theoretical Approaches to Diffraction. There are many methods available to study diffraction, ranging from brute force exact solutions through variational techniques to methods based on Huygen's principle. For low frequencies the exact solution may be obtainable in terms of the separated wave functions for spherical coordinates with appropriate

Reproduced with permission of the copyright owner. Further reproduction prohibited without permission.

boundary conditions, and with separate expansions in the several regions of the antenna. For higher frequencies I will describe methods based on Huygen's principle and based on an exact solution to diffraction by an edge. Huygen's principle is described in many texts and handbooks: Handbook of Physics (1967), p. 6-80; Menzel (1960, p. 341; Born and Wolf (1969), p. 370; Jackson (1962), p. 281; Sommerfeld (1964), p. 195. The Khirchhoff formulas are a correct formulation of Huygen's principle based on an exact solution of the scalar wave equation. Jackson (p. 283) proves a vector formulation of Khirchhoff's equation. To use any of these formulas one must assume knowledge of the wave function and its gradient on a boundary surface. The usual diffraction calculations assume that these take on the values which they would have in the absence of the diffracting object, except where a point is shadowed by the object.

Rigorous solutions to certain problems are given by Sommerfeld (p. 249), and by Born and Wolf (Chapter XI). Sommerfeld was the first to obtain a rigorous solution to any problem of diffraction. J. B. Keller (1962) has made successful generalizations of the known exact solutions. He considers diffraction at edges, points, and surfaces as governed by certain scattering coefficients, whose forms are derived from the exact solutions for special cases. Away from such boundaries, radiation propagates in the manner described by geometric optics. I developed my own method for diffraction calculations which turns out to be conceptually equivalent to Keller's, but described in terms of intensities and scattering cross sections, rather than amplitudes. Within factors of the order of two, my results agree with his.

Reproduced with permission of the copyright owner. Further reproduction prohibited without permission.

I will now sketch the development of my formulations. First I will write down the standard Fraunhofer diffraction pattern for a circular aperture, then average over wavelengths to smooth out the oscillations and obtain convenient approximations, integrate the results with respect to solid angle, and interpret the formulas in terms of cross sections. Following this discussion, I do a parallel development from Sommerfeld's exact solution near an edge and show that there is good agreement.

From Born and Wolf (p. 396), the diffracted intensity from a plane wave incident on a circular aperture is

$$I(\theta) = \frac{D}{\lambda^2}\left[\frac{2J_1(kaw)}{kaw}\right]^2 \quad , \tag{41}$$

where D is the area of the aperture, λ is the wavelength, k is $2\pi/\lambda$, a is the radius of the aperture, and w is $\sin\theta$, where θ is the angle by which the ray is deflected. This result holds for small angles and wavelengths. This intensity is normalized to unit flux through the hole, and its units are sr^{-1}.

This formula is simplified by averaging over wavelength and putting in an asymptotic form for J_1. The limiting form for large x is

$$J_1(x) = \sqrt{2/\pi x}\cos(x - 3\pi/4) \quad . \tag{42}$$

Putting this in and setting $\cos^2(x - 3\pi/4) = 1/2$ gives us the desired average:

$$I(\theta) = (\lambda/\pi^3 d)(1/\sin^3\theta) \quad , \tag{43}$$

where d = 2a is the diameter of the hole. For larger angles, a correction is made by putting in the cosine factors which are in the Khirchhoff

Reproduced with permission of the copyright owner. Further reproduction prohibited without permission.

formula (Born and Wolf, p. 382) and which have been ignored in the above formulas. The result is simply to multiply the diffracted intensity by $\cos^4(\theta/2)$. This factor eliminates the back-scattered light which is predicted by the simplest form of Huygen's principle. It is important that it does not become zero for an angle of $\pi/2$, but is only reduced by a factor of $1/2^2$.

This form with the correction factor can be integrated with respect to angle. The result is that the amount of radiation which is scattered by an angle greater than θ is given by

$$P_>(\theta) = (2\lambda/\pi^2 d)[\cos^4(\theta/2)/\sin\theta - (\pi - \theta)/4]$$
$$\simeq (2\lambda/\pi^2 d)(1/\theta) \text{ for small } \theta \quad . \tag{44}$$

To obtain this result I allowed backscattered light to be counted. Whether this is permissible is somewhat questionable. However, it seems applicable to a case similar to ours, in which the incident plane wave is confined to a pipe which is simply cut off.

To interpret these results in terms of cross sections, I suppose that radiation passing within a distance δ of the edge of the screen is diffracted by an angle greater than θ. For a circle, the area of such a zone near the edge is $2\pi a\delta$, while the total area is πa^2. Setting the ratio of these equal to $P_>(\theta)$ I find that

$$\delta = (2\lambda/\pi^2)[\cos^4(\theta/2)/\sin\theta - (\pi - \theta)/4] \quad . \tag{45}$$

For small angles this result should be approximately correct. For example, radiation which passes within one wavelength of the edge is diffracted by more than 0.2 radians. To be diffracted into the back

Reproduced with permission of the copyright owner. Further reproduction prohibited without permission.

lobe, that is to be diffracted by an angle greater than $\pi/2$, the radiation must come within $\delta = (2\lambda/\pi^2)(1/2 - \pi/8)$ of the edge. This result will be roughly confirmed by calculations from Sommerfeld's exact solution near an edge.

Sommerfeld's solution at a straight edge was published in 1896. An exposition in English is given by Sommerfeld (1964, p. 249 ff). The two remarkable features of this solution are that it (a) is simple, being constructed by the method of images, and (b) has almost the same asymptotic form as the Huygen's principle calculation. His solution for the asymptotic form of the diffracted wave amplitude is

$$u = \frac{1+i}{4\sqrt{\pi kr}} e^{ikr} \left[\sec \frac{1}{2}(\phi - \alpha) \pm \sec \frac{1}{2}(\phi + \alpha)\right] \qquad (46)$$

where the incident plane wave has unit intensity, and α and ϕ are angles defined in Fig. [23], k is $2\pi/\lambda$, and r is the distance of the observing point from the edge. The first term in parentheses becomes infinite for $\phi = \pi + \alpha$, which is the boundary of the shadow, and the second is infinite for $\phi = \pi - \alpha$, which is the edge of the reflected wave. The two signs on this term refer to the two possible polarizations of the electric field.

In order to calculate the energy flow per unit length of edge and per unit diffraction angle, I formed the intensity

$$I(\theta) = r|u|^2 = (\lambda/16\pi^2)\left[\sec^2 \frac{1}{2}(\phi - \alpha) + \sec^2 \frac{1}{2}(\phi + \alpha)\right] , \qquad (47)$$

where I have averaged the two polarizations.

It is possible to integrate this intensity I with respect to angle to obtain the quantity of radiation diffracted by an angle larger than θ.

Reproduced with permission of the copyright owner. Further reproduction prohibited without permission.

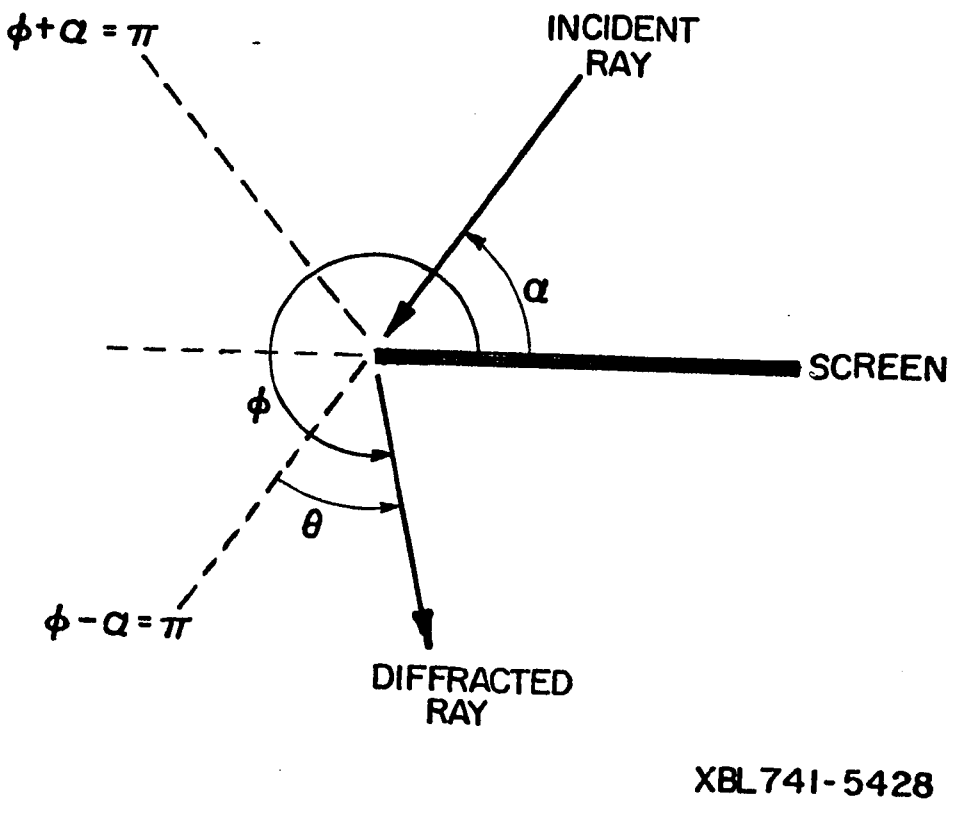

Fig. 23. Diffraction at an edge.

Reproduced with permission of the copyright owner. Further reproduction prohibited without permission.

By θ I mean $\phi - \pi - \alpha$, which is the angle by which the ray is deflected, and I carry out the integration around to the angle of the screen. The result is

$$P_{>}(\theta) = (\lambda/8\pi^2)[\cot\tfrac{1}{2}\theta + \cot\tfrac{1}{2}(\theta + 2\alpha)] \quad . \qquad (48)$$

In these units, the above quantity is simply the distance δ calculated previously for the case of the circle. Evaluating for $\theta = \pi/2$ and $\alpha = 0$ gives $\delta = \lambda/4\pi^2$. This is the amount which diffracts all the way around behind the screen. It is very nearly equal to the value calculated for the circle before. An equal amount is predicted by this formula to be diffracted backwards on the side of the incident ray, so that in all an amount $\lambda/2\pi^2$ is diffracted by an angle greater than $\pi/2$.

b. Application to Our Antenna. The foregoing analysis can be applied to our antenna for three purposes: to estimate the antenna pattern at large angles from the axis, to estimate the back lobe of the antenna, and to find out how much radiation strikes the horn itself, so that we may estimate its emission into the beam.

To estimate the antenna pattern at large angles, we consider the double diffraction problem. Light leaving the antenna is diffracted first at the cone-horn boundary, bounces perhaps on the horn, and is diffracted again to even larger angles at the top of the horn. A simple estimate given below yields results considerably lower than the experimental values, and corrections are estimated which achieve agreement with observations.

The first step is to find the intensity for the singly diffracted wave produced by the cone aperture. If we ignore the influence of the

Reproduced with permission of the copyright owner. Further reproduction prohibited without permission.

horn, this is very similar to the problem of a plane wave incident on a circular aperture in a screen. As seen from the cone mouth, the edge of the horn is 0.3 radians off axis. With a wavelength of 0.06 cm and a cone diameter of 6 cm, the formula for a circular aperture gives $I(\theta) = \lambda/(\pi^3 d \sin^3) = 0.01$ sr^{-1}. By comparison, if the whole large horn aperture were evenly illuminated and carried the same total energy, then $I(\theta)$ would be about 3 sr^{-1} over the entire surface. Our edge is thus illuminated only 1/300 as much as it would be for uniform illumination.

It is, therefore, expected that the large angle diffraction which it produces will be only 1/300 as strong as that from a 15 cm aperture evenly illuminated. At an angle of 60° from the axis, formula (43) would then give $I(\theta) = 4\times10^{-6}$ sr^{-1}. Our observations at this angle gave 10^{-4} sr^{-1}. This discrepancy by a factor of 25 is not understood in detail but the following two obvious factors have so far been neglected.

(a) The beam coming up the cone is actually a set of diverging spherical waves. The geometrical optics sets the r.m.s. deviation of a ray from the axis at 0.05 radians and the maximum deviation at 0.1 rad. Thus a ray does not need to be diffracted as far in order to reach the edge of the horn. If a ray need be deflected by only 0.22 radians instead of 0.3, the intensity is increased by a factor of 3.5.

(b) The rays reaching the edge of the horn are a diverging set, with angles from the axis lying between 0.3 and 0.67 radians, allowing for the reflections of diffracted rays from the horn. These numbers are simply geometrical optics numbers. In order to be diffracted out to 1 radian from the axis, these rays need only 0.7 to 0.33 radians more deflection. If the mean diffraction required is only 0.5 radians instead

Reproduced with permission of the copyright owner. Further reproduction prohibited without permission.

of the value 1 which was previously assumed, the correction required is a factor of 8.

The net result of these two corrections is to bring the estimated diffraction at 60° off axis up to 10^{-4} sr^{-1}, the measured value.

It is important to us to know the antenna response pattern at even larger angles. Adopting the above approach for 90° off axis gives an estimate that $I(90°) = 10^{-5}$ sr^{-1}.

4. Emission Estimates

We have achieved rough agreement between theory and observation for the antenna response function $I(\theta)$. We can, therefore, proceed to estimate the emissions from warm objects into the antenna. The quantity which we calculate here is the effective fraction of the beam which is filled by the object. The theoretical and experimental estimates described above were all made for a mean wavelength of about 0.06 cm, corresponding to a frequency of 16.7 cm^{-1}. The theory shows that at large angles from the axis, all the radiation must be diffracted twice. The scattered intensities are, therefore, proportional to the square of the wavelength, and are ten times larger at a frequency of 5 cm^{-1} than the numbers which we calculate.

The first estimate I make is the response of the antenna to the earth. At observing altitude the horizon is actually depressed by 0.1 radian, due to the curvature of the earth, but we will neglect this effect. Then if the apparatus is tilted by an angle of Ψ from the zenith, the earth occupies a solid angle of 2Ψ in the forward lobe of the antenna. If we consider the typical observing angle of 30° (0.5 rad) and we choose a mean value of $I(\theta)$ as 3×10^{-5}, then we estimate that the

Reproduced with permission of the copyright owner. Further reproduction prohibited without permission.

earth fills a fraction $f_{earth} = 3\times10^{-5}$ of the beam. Because the theoretical response of the antenna falls rapidly between 60° and 90°, the response to the earth will be a steep function of the tilt Ψ.

The second thing I can calculate is the response of the antenna to objects which are behind it. I take a slightly different approach to this problem. Here I calculate the intensity of the light diffracted by the cone and reaching the edge of the horn, and multiply by the cross section of the edge for backscattering. In the previous Section I obtained the angular intensity $I(\theta) = 0.01\ sr^{-1}$ as seen from the mouth of the cone, and then I found a correction factor of 3.5. Sommerfeld's result implies that to diffract around behind the edge of a screen, a ray must pass within a distance $\delta = \lambda/4\pi^2$ of the edge of the screen. For our case this distance is very small, only 0.0015 cm. At the cone mouth, this narrow space around the mouth of the horn subtends a solid angle of only 6×10^{-5} sr. The net result is finally that the back lobe of this antenna is only 2×10^{-6} of the beam.

The other warm objects in the beam are all at angles where the response function $I(\theta)$ has been measured. For instance, there is an aluminum block about 20 cm square located about 150 cm above the balloon gondola, which attaches the gondola cables to the ladder line running to the parachute. When our spectrometer is tilted 30° from the zenith, this block is about 50° off its axis and subtends a solid angle of about 0.01 sr. As a worst case one can suppose it black. Reading from the graph, we find that at 50° from the axis, the normalized antenna response is $2\times10^{-4}\ sr^{-1}$. Then it is as though this object is filling a fraction $f_{block} = (0.01\ sr)(2\times10^{-4}\ sr^{-1}) = 2\times10^{-6}$ of the beam.

Reproduced with permission of the copyright owner. Further reproduction prohibited without permission.

Similarly, the folded parachute is about 40 cm in diameter and is located about 15 m above the payload. It subtends an angle of 6×10^{-4} sr and the normalized response 30° off axis is 6×10^{-4} sr^{-1}, so this object fills a fraction $f_{chute} = 4\times10^{-7}$ of the beam. The balloon is 600 m away and 100 m in diameter, subtending an angle of 2×10^{-2} sr, so it fills a fraction 10^{-5} of the beam. However, the balloon is nearly transparent, being made of 18 μ polyethylene. This material neither emits nor absorbs nor reflects more than 0.01 of the radiation falling on it. Allowing for the conservative upper estimate that 0.05 of the balloon is opaque due to reinforcing tapes and seams, it fills a fraction $f_{balloon} = 5\times10^{-7}$ of the beam.

5. Window Emissions

The helium dewar has two windows which may be removed during flight. The outer window is of Mylar, 0.0127 cm thick. Its function is to protect the spectrometer during ascent, not just from air but also from ballast powder. Present day balloon technique requires that about 10% of the total weight of the balloon be ballast which is dropped during ascent through the tropopause. The reason for this is that above the tropopause, the atmosphere has a nonadiabatic temperature gradient and the helium gas in the balloon is colder than the air around it. It therefore loses lift. Because of weight limitations, we must fly our ballast powder on the rope reel, which is 600 m above the payload. The ballast is fine iron shot so that our Mylar window is made strong to withstand the impacts of the particles as they fall onto the apparatus.

Reproduced with permission of the copyright owner. Further reproduction prohibited without permission.

The Mylar window is so thick that its emission is much larger than the signal we are trying to measure. The absorption coefficient is roughly $\nu/2$ where ν is the spatial frequency, as extrapolated from Loewenstein and Smith (1972, p. 6-302). With our window at 16 cm^{-1} the absorption is then about 0.1. Since it fills the beam it produces an antenna temperature of 20K to 30K. In addition, the refractive index is 1.75, high enough that for some frequencies the coherent two surface reflectivity can be as high as 0.25. These complications should not prevent observing atmospheric line emissions, although it is clearly impossible to measure the 2.7K black body spectrum through this window.

The second window is of Teflon, 0.0003 cm thick, obtained from Dilectrix Corporation. Its purpose is to prevent air from condensing into the antenna, which is at the temperature of liquid helium. This window is thin enough that useful measurements can be made through it. Teflon does not become brittle when cold, and in this thickness it is remarkably elastic.

The Teflon window is almost good enough to permit measuring the 2.7K flux in its presence. The absorption coefficient of Teflon is also roughly proportional to frequency between 10 and 30 cm^{-1}, being about 0.2 cm^{-1} + $\nu/50$, according to the data of Brändli and Sievers (1972). At a frequency of 16 cm^{-1}, our window than has an emissivity of 1.5×10^{-4}, for an antenna temperature of about 4×10^{-2}K. This is roughly an order of magnitude larger than any of the diffraction effects calculated above. In principle it can be distinguished from other effects by its

Reproduced with permission of the copyright owner. Further reproduction prohibited without permission.

spectrum, since the emissivity increases with frequency, while the diffraction goes as the wavelength or the square of the wavelength. However, as Brändli and Sievers showed, the emissivity changes with temperature.

Fortunately it seems to be possible to remove the window completely when the balloon is at float altitude, providing that the gaseous helium outflow from the cryostat is directed through the opening. This idea becomes more plausible when it is pointed out that several important factors change when the gas pressure is reduced to 0.003 atm. Buoyancy forces per unit volume are reduced in proportion to the pressure, but the viscosity of the gases does not change. Taylor instabilities, in which the air falls into the cryostat and the helium is forced out, therefore grow at much slower rates. Simultaneously, the flow velocity of the upwelling helium gas increases in proportion to the reciprocal of the pressure. At float altitude, the flow velocity is about 5 m/sec through the 15 cm hole. It seems that these two effects together are sufficient to prevent air from condensing into the optics.

We have verified this result by a flight simulation in a large vacuum chamber. The capacity of the vacuum pump was so large that we were able to maintain a substantial flow of moist air past the cryostat even at a pressure of 2 mm Hg. Nevertheless, visual observations using a small telescope and a mirror showed no signs of condensation into the antenna.

Reproduced with permission of the copyright owner. Further reproduction prohibited without permission.

6. Horn Emissions

The horn part of our antenna joins the warm cryostat top plate to the copper cone which is at a temperature <10K. As previously discussed, it is heated by conduction through itself and through the helium gas in and around it. The horn is cooled by conduction to the copper cone and by the cold helium gas which flows either through it or around it. The temperature gradient within it is approximately linear, as measured by our attached thermometers and by observations of the levels at which air introduced at the top will freeze.

In order to minimize the thermal conductance of the horn, it is made from stainless steel. To minimize the emissions from this surface, a coating of copper about 0.0013 cm thick was applied to the inner surface by electroplating. Thinner layers did not appear shiny, nor have the expected electrical conductivity. The copper has more thermal conductance than the steel despite its small thickness. The resistance of the copper film decreases by a factor of 15 when it is cooled in liquid helium, as expected for moderately pure copper.

The copper was polished with a chemical polish and coated with a layer of polyethylene 0.005 cm thick. The purpose of this coating is to reduce the emissivity of the metal surface. For metals, there is an analogue to the Brewster's angle phenomenon, in which at a certain angle of metal is completely absorptive for one polarization of incident light. This angle is near grazing incidence. Lest this phenomenon be overemphasized, remember that the flux which can be carried through a surface at grazing incidence is small. However, the situation can still be vastly improved by the use of a dielectric

Reproduced with permission of the copyright owner. Further reproduction prohibited without permission.

overcoating. The dielectric has a very high reflectance for grazing incidence rays and prevents them from ever reaching the metal surface. For angles near normal, the film has little effect and the emissivity is near that for clean bare copper. This emissivity is about 0.001 at room temperature and a frequency of 10 cm^{-1}, and diminishes by a factor of about three or four when it is cooled to liquid helium temperature, due to the increased electrical conductivity. These numbers come from the ordinary skin depth formula and are proportional to $\sqrt{\nu\sigma}$ where ν is the frequency and σ is the d.c. conductivity. The anomalous skin effect is not important for the horn because the conductivity of the copper is not high enough. The effect of the dielectric is to make the emissivity about the same as the normal incidence value for all incidence angles. Detailed calculations were made by David Woody showing the effects of the thickness of the film, and the variations of the emissivity with incidence angle.

A basic estimate of the fraction of the radiation which strikes the horn can be made. Consider as before the time-reversed state with radiation emanating from the detector. Then a nearly-plane wave is incident on the small end of the horn. If we replace the small end by a circular hole in a screen and eliminate the horn altogether, then a fraction $f_1 = 0.01$ of the radiation is diffracted by more than 0.3 radians, using a mean wavelength of about 0.07 cm. In the approximation that the diffracted radiation originates at the center of the hole, this fraction strikes the surface where the horn would be.

Accounting for these factors, the horn emits as though it were an ambient temperature object filling $(0.01)(0.001)(1/3) = 3\times10^{-6}$ of

Reproduced with permission of the copyright owner. Further reproduction prohibited without permission.

the beam. The last factor of 1/3 accounts for an estimate of the mean temperature of the horn. Most of the horn is in the Rayleigh-Jeans limit and its emission is proportional to temperature.

More complex estimates of the problem were also made. The diffracted wave amplitudes for the above model were evaluated from Huygen's principle, both as an integral over area, and in a line integral form quoted by Sommerfeld (p. 316). Fluxes were calculated by differentiating the amplitudes. The amplitudes and fluxes at a point in space can be separated into three distinct parts, one coming direct from the source if the point is not in the shadow, one coming from the near edge of the hole, and one coming from the far edge. This is expected from Sommerfeld's physical description. The surprise was that the part coming from from the near edge has very little flux through the surface occupied by the horn, because the source point of diffraction is already on that surface. Hence there is the suggestion that we were unnecessarily concerned about grazing-incidence rays.

An attempt was made to study the diffraction pattern experimentally, as shown in Fig. 24. The 2.5 cm^{-1} klystron and the diode harmonic generator were used as sources. Measurements were made with and without the horn in place. In order to simulate emission from the horn surface, three holes were then cut in the side of a second horn. As shown in the figure, the waveguide from the klystron was brought up to these holes and the amount of radiation transmitted into the antenna was measured. The diffraction was strongly dependent on polarization, with a factor of ten difference between the two perpendicular states.

Reproduced with permission of the copyright owner. Further reproduction prohibited without permission.

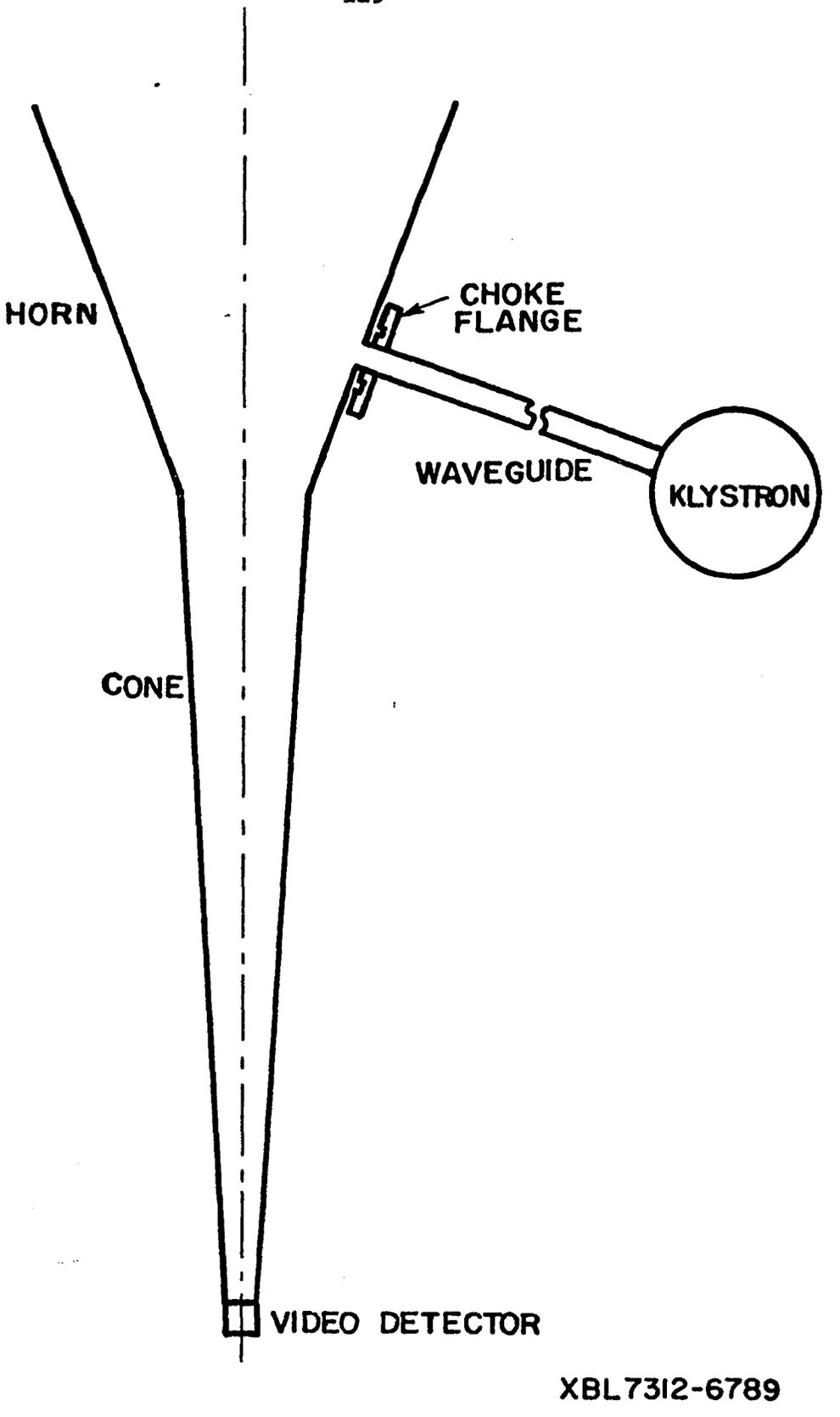

Fig. 24. Horn emission simulator.

Reproduced with permission of the copyright owner. Further reproduction prohibited without permission.

There were two important results of this measurement. First, it was shown that the presence of the perforated horn did not have much effect on the diffracted radiation from the waveguide. When it was removed, leaving only the bare waveguide at the same point in space, no change (within the factor of 2 measurement precision) was observed. The calculation of amplitudes as though the horn is not present is thus justified for the interior of the horn.

Second, the intensity of the diffracted radiation falls off as the waveguide is moved away from the cone mouth in approximately the expected fashion. The results show that the most important part of the horn is adjacent to the cone. Figure 25 is a graph of these results. The curve shows what is expected from a point source of diffraction on the opposite side of the horn.

An experimental measurement of the actual emission from the horn is difficult. In the laboratory it emits only about 10^{-5} as much as the room temperature bodies in the view of the apparatus. We attempted to design a liquid-helium cooled black body that could cover the entire 15 cm aperture to simulate our experiment. We could not find a design which seemed sufficiently good. The requirement of blackness together with accurately known temperature and reasonably long helium hold time could not be met. The problem is that heat fluxes are large, with radiation, conduction, and convection all important. The black materials available are dielectrics, with low thermal conductances. In the thicknesses needed for a black body, they would support a temperature gradient sufficient to invalidate our measurements.

Reproduced with permission of the copyright owner. Further reproduction prohibited without permission.

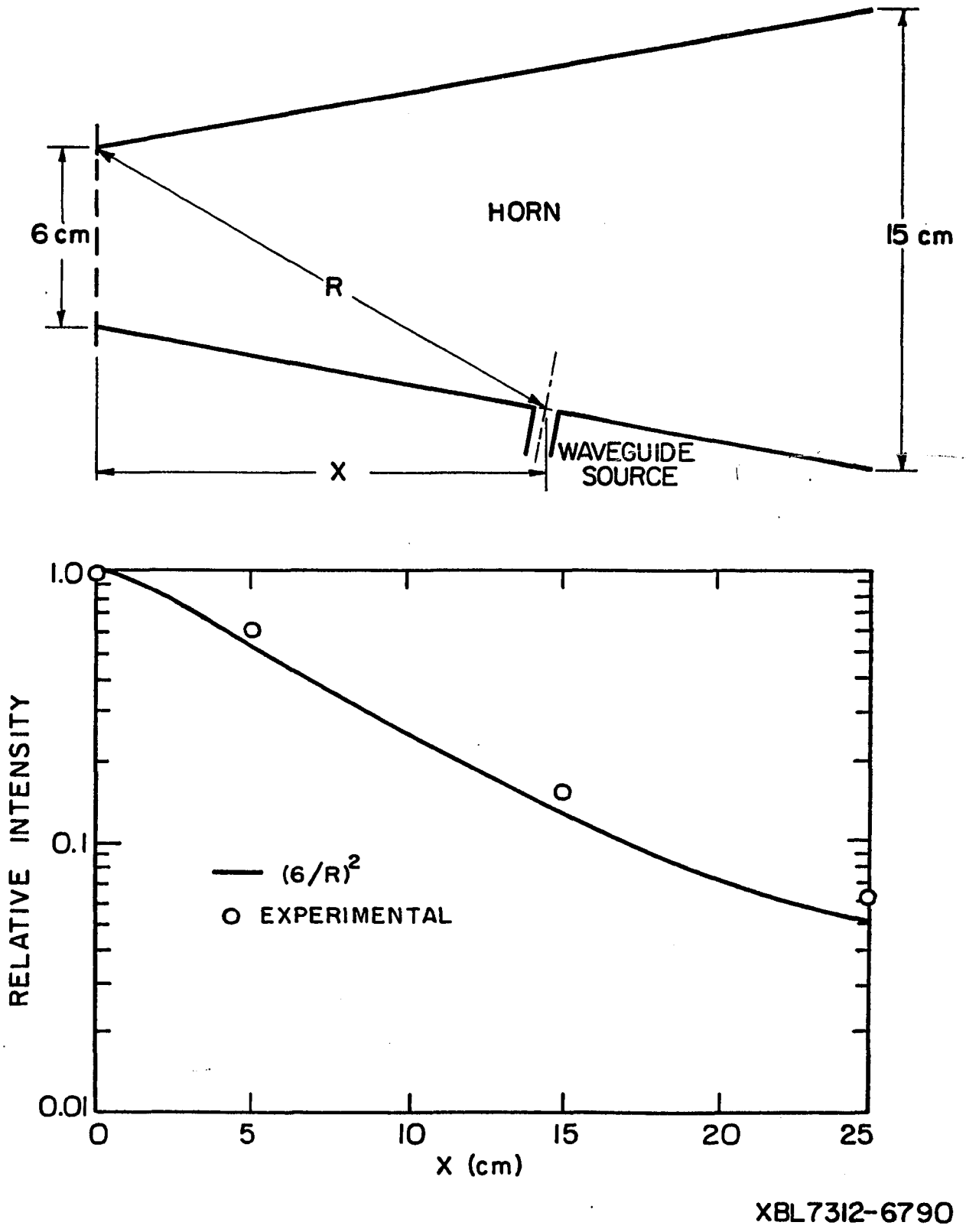

Fig. 25. Horn emission simulation results.

Reproduced with permission of the copyright owner. Further reproduction prohibited without permission.

Therefore, we attempt to measure the emission from this horn during flight. The horn cannot be moved but its temperature can be changed. If the radiation is not negligible, we should see immediate changes in the level of signal when the temperature is varied. This will be measured with the interferometer set at x = 0.

7. Cone Optics and Emissions

The geometrical beam of the antenna is determined by a hollow copper cone. The cone was made of high-conductivity material to reduce its emission. It was electroformed from copper on an aluminum mandrel which was cut to shape and polished on a lathe. The mandrel was dissolved by boiling alkali (Oakite$^{T.M.}$), which required about 15 days. The copper surface was then polished in a special acid polishing solution and then rinsed. The surface appeared very shiny and free of blemishes acept for some grooves near the small end of the cone. The cone was installed in the cryostat and protected from moisture, but it tarnished to a uniform gray color within a few weeks, without spots or corrosion.

Emissions from the cone have been calculated in two ways, which were found to agree. The first method was by ray tracing, with emissivity calculated at each bounce from the angle of incidence and the assumed conductivity of the metal. Hundreds of allowed rays were traced. The lower half of the cone was assumed isothermal at 1.5K and the upper half had a linear temperature profile from 1.5K to 10K at the top. Bryan Andrews, an undergraduate assistant, performed the calculations

Reproduced with permission of the copyright owner. Further reproduction prohibited without permission.

for this geometry and several others. Corrections to the effective conductivity were calculated by David Woody using Pippard's formulas for the anomalous skin effect (Pippard, 1954). The measured conductivity of our electroformed bulk copper ranges from 100 to 300 times the room temperature value when it is in liquid helium. For the former value, and for a frequency of 10 cm^{-1}, the electron collision time is long ($\omega\tau = 4.5$), and the mean free path is very long compared to the skin depth (300 times the classical skin depth). The result of the calculation is that the effective conductivity is greatly reduced. At this frequency, the effective conductivity is only 8 times the room temperature value, rather than 100 times. The emission which results from this calculation is shown in Fig. 20.

Calculations were also made for a cone covered with a 0.005 cm layer of polyethylene. Estimates showed the improvement from using the polyethylene would be a factor of 3 at 2 cm^{-1}, 7 at 5 cm^{-1}, 25 at 10 cm^{-1}, and 90 at 20 cm^{-1}. If we were able to coat our cone with polyethylene, we would be permitted to raise its temperature to 25K without interfering with our measurement.

The other method of calculating cone emission is based on Jackson's treatment of waveguide losses (Jackson, 1962, p. 248 ff). His discussion is a correct version of the following handwaving argument. In an electromagnetic field, the Poynting vector is defined in m.k.s. units as $\vec{E} \times \vec{H}$. In our long thin cone, the fields approximate those of a plane wave in which $|\vec{E}|/|\vec{H}| = Z_o$, the impedance of free space. Then the net power flow in the waveguide is of the order of $P = \langle \vec{H}^2 \rangle Z_o A$,

Reproduced with permission of the copyright owner. Further reproduction prohibited without permission.

where A is the area of the cross section of the pipe. The fields $\vec{H}$ induce currents in the waveguide walls in the amount of $\vec{K} = \vec{n} \times \vec{H}$, in the approximation of perfect conductivity, where $\vec{n}$ is a unit normal to the surface. The first order correction for finite conductivity gives a power loss per unit area of wall of $\vec{K}^2 R_s$, where R_s is the surface resistance of the metal wall. Per unit length of guide this is $dP/dx = \langle K^2 \rangle R_s C$, where C is the circumference of the guide. In this order of approximation, $\langle H^2 \rangle = \langle K^2 \rangle$, so that $(1/P)(dP/dx) = (R_s/Z_o)(C/A)$. Then for our cone, at a distance of r from the apex, $C = 2\pi r\theta$, $A = \pi r^2\theta^2$, and $x = r$, where θ is the half-angle of the cone, and thus

$$\frac{1}{P}\frac{dP}{dr} = \frac{2}{\theta r}\frac{R_s}{Z_o} \quad . \tag{49}$$

For comparison, Jackson's formula 8.63 may be rearranged to give

$$\frac{1}{P}\frac{dP}{dx} = \frac{R_s}{Z_o}\frac{C}{A}(\sec\phi)\left[\xi_m + \eta_m\left(\frac{\omega_m}{\omega}\right)^2\right] \tag{50}$$

In this formula, ξ_m and η_m are dimensionless numbers of the order of unity depending on the mode index m, ω_m is the cutoff frequency for the mode m, and ω is the actual frequency.

The number

$$\sec\phi \equiv \left(1 - \frac{\omega_m^2}{\omega^2}\right)^{-1/2}$$

is equal to the ratio c/v_g, where c is the speed of light and v_g is the group velocity of the waves. In the short wavelength limit, ϕ is the inclination of the wavevector to the axis of the guide. The factor $\sec\phi$ appears rather than $\tan\phi$, which is proportional to the number of

Reproduced with permission of the copyright owner. Further reproduction prohibited without permission.

bounces the ray makes, because the metal absorbs more for grazing incidence reflections.

This model makes possible calculations for an arbitrary temperature distribution in the cone. The apparent antenna temperature from the cone is now

$$T_A = \int_{r_1}^{r_2} \frac{dr}{r} \frac{2}{\theta} \frac{R_s}{Z_o} \cdot T(r) \cdot \frac{h\nu c/kT(r)}{\exp(h\nu c/kT(r)) - 1} \cdot \quad (51)$$

This integral was evaluated numerically for the same temperature distribution used in the tracing of rays, and it agrees within 5% at 10 cm^{-1}.

E. Flight and Results

In this section I will describe first the mechanics of flying a balloon and connecting it to the payload, then the actual flight of our balloon on October 26, 1973, and finally the scientific and engineering results of the tests.

1. Balloon and Rigging

On its first flight our apparatus was carried by a Raven Industries balloon of about 3×10^5 m^3. It was made of polyethylene 0.0018 cm thick, and its mass was about 600 kg. It carried 200 kg of equipment and ballast supplied by the National Center for Atmospheric Research (N. C. A. R.) Scientific Balloon Facility in Palestine, Texas. The balloon was filled, launched, tracked and retrieved by the men of the Balloon Base, and we are much indebted to their skill for the success of our flight.

Reproduced with permission of the copyright owner. Further reproduction prohibited without permission.

The payload itself was 250 kg. It was attached by four wire cables to a spreader bar just above it, which was attached by two more cables to a square aluminum plate about 20 cm square and 150 cm above the spectrometer. The plate has a hole in the center which slips over a stout peg on the launch vehicle. The launch vehicle carried the payload by means of this peg. Above the square plate was a ladder line about 15 m long, composed of two steel cables separated about 30 cm by aluminum rungs. Above the ladder line was the parachute, a nominal 11.5 m size, which when folded is a cylinder about 30 to 60 cm in diameter. The parachute was a part of the suspension. Attached to the top of the parachute was a 600 m rope of 0.95 cm braided nylon. This rope was attached at the top to a special reel which unrolled it in flight, a few minutes after the payload left the ground. The reel was suspended from its own parachute which in turn was suspended from the balloon. As previously mentioned, 10% of the weight of the balloon was carried as ballast and dropped at the tropopause. In our case, there was 113 kg of fine iron powder suspended in a hopper attached to the rope reel.

The system was intended to come down in four parts: the payload on its parachute, the rope with none, the rope reel on its parachute, and the balloon, which is burst and floats down on its own. The rope and balloon are not usually recovered. The rope reel carried a 1.68 MHz beacon which was keyed on and off by a barocoder. A barocoder is a barometer whose output is in Morse code. The barometer is a primary means of watching the ascent of a balloon. Our beacon was known to be partially defective before launch, and it became silent a few minutes

Reproduced with permission of the copyright owner. Further reproduction prohibited without permission.

after launch. It nevertheless was an aid to the recovery as it was not completely silent at short range.

No beacon or locating device was provided for the payload itself. This was an oversight which could have made recovery difficult. However, this time the mechanism which should have separated the payload from the rope did not work, and neither did the device which separates the rope from the reel. The combination of these two failures meant that the payload was still attached to the beacon and recovery was easy. The cause for the failure of the first of these mechanisms was seen on landing. The insulation on power wires leading along the parachute shrouds had broken off. The insulation failed when the leads were flexed while very cold, presumably during the initial stage of the descent from the balloon. Teflon insulation would not have broken.

2. Launch and Trajectory of the Balloon

The launch of the balloon required about 4 hours and the energy of about seven men and several special vehicles. Four hours before launch the launch truck picked up the payload with its special peg and drove to the launch pad, a large flat paved area. The launch train was then laid out across the top of the launch truck and on the ground, leading across the pad to the balloon. The balloon was initially a cigar-shaped piece of folded plastic about 150 m long. It was inflated through plastic tubes leading to what would be the top of the balloon. Only 1/300 of the volume of the balloon was filled, to allow for expansion of the helium during ascent. This small volume formed a bubble about 25 m high at the top of the balloon. This bubble was held down by a second special truck. The rest of the balloon lay mostly

Reproduced with permission of the copyright owner. Further reproduction prohibited without permission.

on the ground, under tension because of the pull of the helium bubble. When the truck released the balloon, the bubble rose over the payload under the combined forces of the tension of the ropes and the wind, which was about 5 knots. As the bubble came over the payload truck, the truck moved along the ground until the balloon and rigging were precisely vertical and taut, and then released the payload.

The launch time was 6:50 p.m. CDT, October 26, 1973. The balloon accelerated slowly, as the free lift was only 10% of the total weight. It ascended at a roughly uniform velocity until it reached float altitude about 3 hours later, 10:00 p.m. The altitude reached was about 39 km, and the barometric pressure was about 2.2 mm Hg. At that altitude and season, the winds were about 45 m/sec from the west. Four and one half hours later, the payload was about to reach Georgia. At that time the radar in Atlanta, which was our only accurate tracking method, went off the air from equipment failure. We were therefore requested to end the flight immediately. The descent was commanded by a tracking airplane and occurred as described above, with none of the separation mechanisms working. The payload was recovered the next morning in excellent condition from a tree near a creek at Anniston, Alabama. There were no apparent ill effects caused by the failure of the separation devices.

3. Instrumental Performance During Flight

Data analysis from the flight has not yet been completed, but the major features are reported here. The interferometer stepper motor froze up during the ascent and spectra were not obtained of the cosmic background radiation. Spectra were observed during the

Reproduced with permission of the copyright owner. Further reproduction prohibited without permission.

early ascent, through the Mylar window and much water and ozone, but are expected to have only engineering importance to us.

This series of spectra was abruptly halted about 40 minutes after launch when the cryostat broke into acoustic oscillation at a frequency very close to the chopping frequency, within 5%. This oscillation was seen as a large sinusoidal signal from the bolometer, much larger than the optical signal. Infrared data could not be observed in the presence of this signal, so the interferometer motor was eventually commanded to cease stepping. The acoustic oscillation was not a surprise as it has been observed in laboratory simulations, but the frequency was different. It is presumed to be an ordinary organ-pipe oscillation excited by the rapid gas flow out the small (2.5 cm) valve and pipe.

The oscillations ceased 45 minutes before the balloon came to its float altitude. The interferometer was again commanded to sweep through the interferogram. It was noticed some time later that although the stepper motor was stepping along, it was not taking large enough steps, and the step length was gradually getting smaller and smaller. When this was discovered, attempts were made to command the motor to move differently, and it was found that turning it more slowly gave it more power. It still could turn, but it could not turn fast enough to reach the zero path difference point ($x = 0$) before the stepper became too weak to turn at all.

There are two possible kinds of explanations: either the ballast powder got into the gears of the motor, or else the low temperature of

Reproduced with permission of the copyright owner. Further reproduction prohibited without permission.

the payload adversely affected it. The second explanation seems more plausible, since the payload became much colder than anticipated or designed for, reaching a temperature of -60°C, barely on scale on our thermometers. It is not known yet where the fault lay, but the four likely possibilities are that the motor itself froze up, the auxiliary position readouts froze, the sliding O-ring seal where the shaft enters the cryostat froze, or the electronic power supply became weaker when cold.

In default of measuring interferograms, we attempted to use zenith-angle scanning data and to verify that the rest of the instrument worked. Because of the way the chopper wheel is made, with opaque spokes between the polarizers, it produces a chopped signal at twice the fundamental frequency which is proportional to the total amount of radiation incident on the chopper. It is independent of the path difference in the interferometer. We were thus able to verify the effects of windows, calibrator, and zenith angle scans on the total signal level.

The results have not yet been fully interpreted. They do show that the windows both opened, that the first one emitted about as much as expected, and that the second window did not open all the way. This failure was merely a procedural error, since the window caught on the mirror which allowed photography of the cryostat. Before this was understood, the payload went out of commanding range, and we were not able to open the window fully. The effects of air condensing into the antenna were seen, due to another procedural error. When the second window was opened, the valve which controls the gas flow should have

Reproduced with permission of the copyright owner. Further reproduction prohibited without permission.

been rotated so that all the gas was forced out through the cone and horn. When this situation was corrected, emissions from the horn were reduced as cold helium has cooled the surfaces on which the air had condensed, and the signal returned to its former level.

Except for the stepper motor and one superfluid pump which failed, and a few procedural errors, most of the flight went as planned. Only a few changes are needed to repeat the experiment, although the experience gained was sufficient to suggest dozens of further changes for convenience and certainty.

Reproduced with permission of the copyright owner. Further reproduction prohibited without permission.

IV. FOURIER TRANSFORMATIONS

In this section I describe the mathematics of Fourier transformations as they apply to our instrument. Two good references on the subject are the books by R. J. Bell (1972) and R. Bracewell (1965). In Section A I give the basic definitions and inversion formula. In Section B I discuss the effects of sampling and finite resolution. In Section C I discuss phase correction procedures and my own investigations. In Section D I calculate the effect of noise on the Fourier transformation.

A. Definitions and Inversion Formulas

A summary of the formulas of this and following theoretical sections is given in Table VII. The basic input is the expression for the transmission of the interferometer, integrated over frequency,

$$I(x) = I(\infty) + \int_0^\infty S(\nu) \cos(2\pi\nu x + \phi(\nu)) \, d\nu \quad , \qquad (52)$$

where $I(x)$ is the measured interferogram as a function of path difference (which is twice the mirror displacement), and $I(\infty)$ is a constant conveying no spectral information. The beams in our instrument are balanced so $|I(\infty)| < 0.03\ I(0)$. The function $S(\nu)$ is the spectrum to be measured. It is the product of the input spectral brightness F_ν(W/cm^{2}sr cm^{-1}) times the instrumental frequency response $T(\nu)$, the throughput $A\Omega$, and the gains of detectors, amplifiers, digitizers, etc.

The function ϕ is called the phase error. For the ideal spectrometer, it is zero for all frequencies. For our spectrometer it is nonzero for two reasons. First, it is difficult to arrange to know correctly where the origin of the coordinate system is. This error produces a phase

Reproduced with permission of the copyright owner. Further reproduction prohibited without permission.

Table VII. Fourier transforms, phase correction, and noise.

1. $I(x) = I(\infty) + \int_0^\infty S(\nu) \cos(2\pi\nu x + \phi(\nu))\, d\nu$ relates interferogram, spectrum and phase function.
2. Assume $I(\infty) = 0$ below.
3. $G = \tilde{I} \Leftrightarrow G(\nu) = \int_{-\infty}^{\infty} I(x)\, e^{-2\pi i\nu x}\, dx$ defines Fourier transform symbol ~ and the function G, and expresses $\tilde{I}$ interms of I.
4. The Fourier inversion theorem, $\tilde{I} = G \Leftrightarrow I(x) = \int_{-\infty}^{\infty} G(\nu)\, e^{+2\pi i\nu x}\, dx$ expresses I in terms of $\tilde{I}$.
5. $S(\nu) = 2e^{-i\phi(\nu)}\, G(\nu) = 2|G(\nu)|$ recovers $S(\nu)$ from $G(\nu)$.
6. $\phi(\nu) = \arg(G(\nu))$ recovers $\phi(\nu)$.
7. $III(x) = \sum_{j=-\infty}^{\infty} \delta(x - j)$ defines Shah or comb function.
8. $I_{sa}(x) = I(x)\, III(x/\Delta x)\, A(x)$ defines sampled and apodized interferogram.
9. $\bar{G}(\nu) = (\Delta x) \sum_{j=-M}^{M} I(j\Delta x)\, A(j\Delta x)\, e^{-2\pi i\nu j\Delta x}$ is the computer approximation to $G(\nu)$.
10. $B = C \circledast D \Leftrightarrow B(x) = \int_{-\infty}^{\infty} C(x')\, D(x - x')\, dx'$ defines the convolution symbol $\circledast$.
11. $B = C \circledast D \Leftrightarrow \tilde{B} = \tilde{C} \cdot \tilde{D}$ is a form of the Convolution Theorem.
12. $B' = C'D' \Leftrightarrow \tilde{B}' = \tilde{C}' \circledast \tilde{D}'$ is another form of the Convolution Theorem.
13. $\Delta x = \frac{1}{2\nu_{max}}$ and $\Delta\nu = \frac{1}{2x_{max}}$ are the sampling intervals needed to represent correctly functions with known maximum frequency or path difference. $\Delta\nu$ is the nominal resolution of an interferogram.
14. $C(x) = \int_{-\infty}^{\infty} e^{2\pi i\nu x}\, e^{-i\phi(\nu)}\, d\nu \Leftrightarrow \tilde{C} = e^{-i\phi}$ defines convolution function.
15. $I_c = C \circledast I$; $I_{sac} = C \circledast I_{sa}$ defines phase-corrected interferograms.

Reproduced with permission of the copyright owner. Further reproduction prohibited without permission.

Table VII. Continued.

16. $C(x) = \frac{1}{\Delta x} \operatorname{sinc}\left(\frac{\pi(x - \alpha)}{\Delta x}\right)$ is the convolution function for a simple x origin shift by α.

17. $I_{sac}(j\Delta x) = (\Delta x) \sum_{k=-\infty}^{\infty} I_{sa}((j - k)\,\Delta x) \cdot C(k\Delta x)$ is computational form of I_{sac}.

18. $\langle \bar{N}^2(\nu) \rangle = n^2 \int_{-\infty}^{\infty} |A(x)|^2 V(x)\, dx$ gives the noise $\bar{N}$ on a spectrum point, given the noise $n/\sqrt{Hz}$ on the interferogram and $V(x) = dx/dt$.

19. $\sqrt{\langle N^2(\nu) \rangle} = (n/\sqrt{T})(1/\Delta\nu)$ gives noise on an "unapodized" spectrum with nominal resolution $\Delta\nu$ and total time T.

20. $V(x)\, A(x) =$ some constant gives optimum use of observing time.

Reproduced with permission of the copyright owner. Further reproduction prohibited without permission.

function proportional to frequency. Second, dispersive effects arise in dielectrics, in gratings such as our beamsplitter, and by unwanted reflections from nominally black surfaces around the optical surfaces. Beam misalignment produces phase errors as a second order effect.

Even with the phase error, the spectrum $S(\nu)$ can be recovered. The inversion formula is

$$S(\nu) = 2e^{-i\phi(\nu)}\, G(\nu) \quad , \tag{53}$$

where $G(\nu)$ is defined for all complex numbers ν by the formula

$$G(\nu) = \int_{-\infty}^{\infty} e^{-2\pi i \nu x}\, I(x)\, dx \quad . \tag{54}$$

The value of $S(\nu)$ may be obtained from $G(\nu)$ by taking the absolute value, or if $e^{i\phi}$ is a tabulated or otherwise known function, it may be divided out.

Another method is to create a new interferogram $I_c(x)$, which has no phase error. This can be done with a convolution, as discussed in a separate section below.

The function $G(\nu)$ is a complex function for complex ν. Because $I(x)$ is real, $G(\nu)$ has the symmetry property $G(-\nu^*) = G^*(\nu)$. For real ν this is even simpler, $G(-\nu) = G^*(\nu)$. The function $I(x)$ can be determined from $G(\nu)$ by a Fourier transformation also:

$$I(x) = \int_{-\infty}^{\infty} G(\nu)\, e^{+2\pi i \nu x}\, d\nu \quad , \tag{55}$$

$$G(\nu) = \int_{-\infty}^{\infty} I(x)\, e^{-2\pi i \nu x}\, dx \quad . \tag{56}$$

Reproduced with permission of the copyright owner. Further reproduction prohibited without permission.

B. Sampling and Resolution

To perform a numerical approximation to the integral for $G(\nu)$, we sample $I(x)$ at certain equally spaced values $j\Delta x$, for integer j. This operation is represented mathematically by multiplying the interferogram by the shah or comb function

$$III(x/\Delta x) = \sum_{j=-\infty}^{\infty} \delta(x/\Delta x - j) \quad , \tag{57}$$

where δ is the Dirac distribution.

We also multiply $I(x)$ by another function $A(x)$ called the apodizing function. This function is chosen so that $A(0) = 1$, and $A(x) = 0$ for $|x| > L$, where L is the maximum path difference at which observations are made. In terms of the index j, this means the resulting sums will be carried out for $|j| < M$. The result of these two multiplications is the sampled and apodized interferogram

$$I_{SA}(x) = I(x)\ III(x/\Delta x)\ A(x) \quad . \tag{58}$$

Our computed spectrum is now

$$\bar{G}(v) = (\Delta x) \sum_{j=-M}^{M} I(j\Delta x)\ A(j\Delta x)\ e^{-2\pi i j \nu \Delta x} \quad . \tag{59}$$

The convolution (fältung) theorem may be used to cast this into another useful form. If the function B is the convolution of the functions C and D, defined by

$$B(x) = \int_{-\infty}^{\infty} C(x')\ D(x - x')\ dx' \quad , \tag{60}$$

Reproduced with permission of the copyright owner. Further reproduction prohibited without permission.

then the Fourier transform of B is the product of the transforms of C and D. Similarly, if it is known that B' is the product of the functions C' and D', then the Fourier transform of B' is the convolution of the transforms of C' and D'. The algebraic manipulations involved in this theorem are simply changing variables and rearranging the order of integration steps.

Using the convolution theorem twice then allows us to state that the function $\bar{G}(\nu)$ (note the bar), which is our computed approximation to $G(\nu)$, is now the convolution of the Fourier transforms of three functions: $I(x)$, $III(x/\Delta x)$, and $A(x)$. The transform of $I(x)$ has already been named $G(\nu)$. The transform of $III(x/\nu x)$ is itself, in that

$$\int_{-\infty}^{\infty} e^{-2\pi i \nu x} \, III(x/\Delta x) \, dx = \Delta x III(\nu \Delta x) \quad . \tag{61}$$

The transform of $A(x)$ is defined to be the experimental resolution function $R(\nu)$.

The result of these two convolutions is that the information contained in $G(\nu)$ is partly lost in $\bar{G}(\nu)$. No mathematical transformations can tell us about the unsampled part of the interferogram unless we have a priori knowledge of the forms of the functions involved. The first such knowledge is easy to obtain. We usually know that $S(\nu)$ is zero for ν larger than a certain maximum frequency ν_{max}. This can be arranged at the convenience of the experimenter with lowpass filters. If $S(\nu)$ is zero, then so is $G(\nu)$ and $G(-\nu)$. Now Δx can be chosen so that $\nu_{max} = \frac{1}{2\Delta x}$. If this is so, then convolution of $G(\nu)$ with

Reproduced with permission of the copyright owner. Further reproduction prohibited without permission.

$\Delta x III(\nu\Delta x)$ does not affect at all the values of $G(\nu)$ for $|\nu| < \nu_{max}$. The sampling produces then no error whatever.

The other case is more serious. Convolution of the true G with the resolution function $R(\nu)$ causes a loss of resolution. The computed $\bar{G}(\nu)$ would be same regardless of the form of the interferogram for $|x| > L$. The choice of apodizing function is a matter of convenience for the experimenter. Except where $A(x) = 0$, the operation of multiplying $I(x)$ by $A(x)$ does not lose information, if it is borne in mind what exact $A(x)$ is used. The original interferogram as sampled and apodized $I_{sa}(x)$ can be reconstructed easily from $\bar{G}(\nu)$, and with $A(x)$ known, the effect of apodizing can be undone.

A table of apodizing functions and their Fourier transforms is given in Table VIII. The functions have different effects on the computed spectra. The best apparent resolution width defined by the width of the function R at half maximum is obtained with the constant apodization $A_o(x) = 1$ for $|x| \leq L$. This resolution is approximately the number $\Delta\nu = 1/(2L) = 2\nu_{max}/(2M + 1)$. The interesting feature of this number is that it is the resolution one is "allowed" by information theory. If $\bar{G}(\nu)$ is computed at intervals of $\Delta\nu$ from $-\nu_{max}$ to $+\nu_{max}$ for a total of $2M + 1$ points, then these values suffice to reconstruct the sampled and apodized interferogram for its total of $2M + 1$ points. The interferogram $I_{sa}(x)$ is real, and the function $\bar{G}(\nu)$ is complex but redundant. The symmetry $\bar{G}(-\nu^*) = \bar{G}^*(\nu)$ corresponds to the fact that I is real, which is sufficient to reduce $\bar{G}(\nu)$ to $2M + 1$ independent real numbers.

Reproduced with permission of the copyright owner. Further reproduction prohibited without permission.

Table VIII. Apodizing functions and corresponding resolution functions.

	Apodizing Function A(x)	Resolution Function R(ν)
1.	$A(x) = \int_{-\infty}^{\infty} R(\nu)\, e^{+2\pi i \nu x}\, d\nu$	$R(\nu) = \int_{-\infty}^{\infty} A(x)\, e^{-2\pi i \nu x}\, dx$
2.	$A_o(x) = 1$ for $\lvert x\rvert \leq L$ $= 0$ for $\lvert x\rvert > L$	$R_o(\nu) = 2L\, \frac{\sin(2\pi\nu L)}{2\pi\nu L}$ $= 2L\, \mathrm{sinc}(2\pi\nu L)$
3.	$A_1(x) = 1 - \left\lvert\frac{x}{L}\right\rvert$ for $\lvert x\rvert \leq L$ $= 0$ for $\lvert x\rvert > L$	$R_1(\nu) = L\, \mathrm{sinc}^2(\pi\nu L)$
4.	$A_2^{(n)}(x) = \left(1 - \frac{x^2}{L^2}\right)^n$ for $\lvert x\rvert \leq L$ $= 0$ for $\lvert x\rvert > L$	$R_2^{(n)} = \frac{n!\sqrt{\pi} L 2^{n+1/2} J_{n+1/2}(2\pi\nu L)}{(2\pi\nu L)^{n+1/2}}$ $= L 2n! \left(\frac{-2d}{dZ}\right)^n \left(\frac{\sin Z}{Z}\right)$ where $Z = 2\pi\nu L$
5.	$A_3^{(\sigma)}(x) = e^{-x^2/2\sigma^2}$ for all x	$R_3^{(\sigma)}(\nu) = \sqrt{2\pi}\sigma\, e^{-\nu^2/2b^2}$, where $b = 1/(2\pi\sigma)$

Reproduced with permission of the copyright owner. Further reproduction prohibited without permission.

The resolution function R_o has, as mentioned, the narrowest peak of typically used functions with a given L. It has disadvantages for some purposes in that its wings extend far from the peak, falling off only as $1/\nu$, and oscillate in sign. The function $A_1(x)$ is easily computed, and its transform $R_1(\nu)$ has the properties that it falls off as $1/\nu^2$ and that it is everywhere positive or zero. The polynomial apodizations $A_2^{(n)}(x)$ produce resolution functions which fall off as $1/\nu^{n+1}$, so that for large n the wings can be suppressed very well, although the central peak gets wider as n increases. These polynomial apodizations approach Gaussian functions as n increases. The Gaussian apodization function $A_3^{(\sigma)}(x)$ is a convenient function for interpretation, as its transform is of the same form and the wings are very well suppressed.

At the end of all the computation it is of course necessary that $\bar{S}(\nu)$ be recovered from $\bar{G}(\nu)$, since we only use positive real frequencies in our classical discussion of interferometers.

C. Phase Correction

As mentioned previously it is not usually the case that the phase function $\phi(\nu)$ is zero. The brute-force method of calculating $\bar{S}(\nu) = 2|\bar{G}(\nu)|$ has four disadvantages. First, it requires measuring I(x) on the entire range (-L, +L), although half of this information is redundant if the phase function is known or is specifically zero. Second, it requires for computation the use of four times as many real number storage locations in the computer as there are output values. This factor can be reduced to two if the computations judiciously use the knowledge that I(x) is real. Third, finding the modulus of $\bar{G}(\nu)$ is a nonlinear operation which produces a biased result in

Reproduced with permission of the copyright owner. Further reproduction prohibited without permission.

the presence of noise. Fourth, the noise in the absence of signal is larger than necessary by a factor of $\sqrt{2}$ because both modulus and phase are being determined from the experimental data, while in fact a great deal can be known about the phase function.

The third and fourth objections are both met by any method which uses external knowledge of the phase function to write

$$\bar{S}(\nu) = 2\mathrm{Re}\left[e^{-i\phi(\nu)}\ \bar{G}(\nu)\right] \quad ,$$

where $\phi(\nu)$ is assumed known. This operation is a linear operation which does not bias the result in the presence of noise, nor increase it in the absence of signal.

The first and second objections are met by Connes' method of Convolutional Phase Correction (R. J. Bell, Chapter 12; Forman, Steel, and Vanasse (1966); Sakai, Vanasse and Forman (1968); J. Connes (1970)). The equivalent multiplicative method of Mertz (1965) has been critized by Walmsley, et al. (1972) and their objections met by Sanderson and Bell (1973).

We have discovered problems with the Convolution method, as described below. The theorem states that multiplication of two functions corresponds directly to convolution of their transforms. Therefore, we can compute the product $\bar{G}(\nu)\ e^{-i\phi(\nu)}$ by computing the convolution of $I_{sa}(x)$ with the transform of $e^{-i\phi(\nu)}$, obtaining a "phase-corrected interferogram" denoted by a subscript c: $\bar{I}_{sac}(x)$. We then retransform $\bar{I}_{sac}(x)$ to get a phase-corrected $\bar{G}_c(\nu)$, and then $\bar{S}(\nu) = 2\mathrm{Re}\bar{G}_c(\nu)$.

Now this operation does not look simpler and in general it is not. However, for typical experimental devices, the convolution function, which is

Reproduced with permission of the copyright owner. Further reproduction prohibited without permission.

$$C(x) = \int_{-\infty}^{\infty} e^{2\pi i \nu x} e^{-i\phi(\nu)} \, d\nu \, , \qquad (62)$$

has very desirable properties. The phase function is usually a very smooth and slowly varying function, and its transform C(x) is therefore small for large $|x|$. No great harm is done to the function C(x) if it is apodized with one of the functions A(x) from the table, but with its own $L' \ll L$. Thus C(x) is a function whose values need not be known for many points. A few numbers suffice to specify the phase function for all frequencies.

This property of C(x) permits us to determine the phase-corrected interferogram $\bar{I}_{sac}(x)$ for positive x without having to measure I(x) for $x < -L'$. Since $L' \ll L$, the number of points of the interferogram which must be observed is reduced almost by half. We need the phase-corrected interferogram for positive x only, since by hypothesis we have corrected with phase error and the corrected interferogram is symmetric, $I_c(-x) = I_c(x)$.

The root question is, of course, how are we to evaluate C(x)? Ordinarily we do not know what it should be from a priori information. The exception is the simple case where there is a simple displacement of origin, so that $\phi(\nu) = 2\pi\nu\alpha$. If the displacement α is known then we can find that $C(x) = 2\nu_m \cdot \frac{\sin(\pi \cdot (x-\alpha)/\Delta x)}{(x-\alpha)/\Delta}$. If α is zero and this formula is evaluated for $x = j\Delta x$, the result is zero except for $j = 0$, when it is $2\nu_m$. When the integral convolution is replaced by a sum, we get a factor Δx which cancels this.

In deriving this result I implicitly have truncated the function $e^{-i\phi(\nu)}$ at $|\nu| = \nu_{max}$. To see the justification for this, consider

Reproduced with permission of the copyright owner. Further reproduction prohibited without permission.

that we only care about frequencies less than ν_{max}. For frequencies higher than this we have no information coming in, and we are perfectly permitted to ignore $e^{-i\phi(\nu)}$ for frequencies higher than ν_{max}. So then

$$C(x) = \int_{-\infty}^{\infty} e^{2\pi i\nu x - i\phi(\nu)} \, d\nu \quad .$$

Because we are concerned only with low frequencies, we need not evaluate C(x) at all points x, but only at those x which are multiples of Δx.

Now the second question arises, which is how well we must approximate this integral form for C(x). We will usually find it from some kind of experimental data, either from some calibration run standardizing the instrument, or else from the interferogram at hand. We measure an interferogram from $x = -L'$ to $+L$, with $L' << L$. We then take the data from the section near $x = 0$, with x between $-L'$ and $+L'$. We transform this section to obtain a computed $\bar{G}(\nu)$, and then find the quantities $e^{-i\bar{\phi}(\nu)}$, where as usual the bar indicates a computed quantity. We use this function to evaluate $\bar{C}(x)$. Hopefully our computed $e^{-i\bar{\phi}(\nu)}$ bears some resemblance to the true $e^{-i\phi(\nu)}$, which is a smooth function which is equal to unity at $\nu = 0$. At frequencies where the spectrum contains energy, the phase function is well determined and has the correct smooth behavior. At frequencies where there is no energy to be measured, the phase function cannot be measured either. The results are therefore noisy and any value for the phase can result. However, if there is any signal at all, the fact that L' is small maximizes the signal-to-noise ratio, smoothes over places in the spectrum where there is no signal, etc. It is important that the incoming spectrum be everywhere positive in order that the computer does not give confusing results, for it has

Reproduced with permission of the copyright owner. Further reproduction prohibited without permission.

no way of knowing that a negative signal does not simply mean that the phase has been shifted by 180°.

Now the integral over frequency must be evaluated by a discrete sum as usual. Our usual procedure is simply to use the same values of the frequency at which the phase function was first computed. These were set by the value of L'. The result is that the values of $\bar{C}(x)$ are computed over the same range, $|x| \leq L'$. The correct C(x) is small near the ends of this range as indicated before. The computed $\bar{C}(x)$ often is not, because of noise in some regions of the spectrum.

In order to use these experimental $\bar{C}(x)$ measurements, we apodize them too. To do nothing to the computed values is to truncate them, using the apodizing function $A_o(x)$. It is preferable to use one of the other functions, as will be shown here. Multiplying $\bar{C}(x)$ by an apodizing function A(x) is equivalent by the convolution theorem to convolving $e^{-i\bar{\phi}(\nu)}$ with the resolution function $R(\nu)$. Any apodizing function works well if the function $e^{-i\bar{\phi}(\nu)}$ is well behaved, but if not, the behavior is quite different. Convolution with the function R_o, with its long wings and oscillatory behavior, can increase the modulus of a noisy $e^{-i\bar{\phi}(\nu)}$ to around two or three at some frequencies, while diminishing it at others. Using such a truncated convolution function $\bar{C}(x)$, therefore, simulates signal energy at frequencies where there is none. All the other apodizing functions in the table are better than the first one in this regard. They can not increase the modulus of even a noisy $e^{-i\bar{\phi}(\nu)}$ much past unity, since the resolution functions are positive at most frequencies. The result in these cases is limited to producing a spurious decrease of signal and noise at certain

Reproduced with permission of the copyright owner. Further reproduction prohibited without permission.

frequencies where the experimental phase function is noisy. These conclusions were all derived from studies of computational results.

The above considerations of noise apply most directly to our experiment. They show that it is necessary to derive the convolution function from a spectrum with good signal-to-noise ratio at the frequency of interest, say a standard calibration spectrum with a long observation time on a bright source.

The convolutional method does not make explicit use of the fact that the phase function is smoothly varying. However, it does the equivalent by taking the phase function from only a short section of interferogram, corresponding to low resolution. The method would be improved if the experimenter were able to supply a physically reasonable extrapolation of the phase function to those frequencies where the signal level is zero. Then the questions discussed above about apodization would be much less relevant.

D. Noise on Interferograms and Optimal Observing

I will now show that under ideal conditions, the noise on the recovered spectrum depends only on a certain mean mirror velocity and on the apodizing function used. It does not depend on the sampling interval if the total observing time is held fixed. I will show that the noise may be minimized by making the observing time at each point proportional to the value of the apodizing function at that point.

Let the root-mean-square noise from the detector, lock-in amplifier, digitizer, etc. be given as n units/$\sqrt{\text{Hz}}$. Then the rms noise on a measurement of I(x) is $n/\sqrt{2t(x)}$, where t(x) is the averaging

Reproduced with permission of the copyright owner. Further reproduction prohibited without permission.

time used to observe the value of I(x). This is true because the equivalent noise bandwidth of an averager is B = 1/2t, where t is the averaging time. We assume that the noises for successive samples of I(x) are completely uncorrelated.

Let the true interferogram I(x) be sampled at the points $x = j\Delta x$, and let the added noise be $N(j\Delta x)$. Then because the Fourier transformation is a linear operator, the noise on the spectrum $\bar{N}(\nu)$ is the Fourier transform of the noise on the interferogram. Note that the bar signifies Fourier transform here. Then our assumption of non-correlation means

$$\langle N(j\Delta x)\ N(k\Delta x)\rangle = \frac{n^2}{2t(x)}\ \delta(j,k) \quad , \tag{63}$$

where $\delta(j,k) = 1$ if $j = k$; zero otherwise. The noise on the spectrum is now

$$\bar{N}(\nu) = \sum_{j=-M}^{M} (2\Delta x)\ \cos(2\pi\nu j\Delta x)\ N(j\Delta x)\ A(j\Delta x) \quad . \tag{64}$$

Note that for this discussion I am assuming no phase error. From this formula we can immediately write the correlation of $\bar{N}(\nu)$, $\bar{N}(\nu')$ as

$$\begin{aligned}\langle \bar{N}(\nu)\ \bar{N}(\nu')\rangle = \Big\langle \sum_{j=-M}^{M} \sum_{k=-M}^{M} & (2\Delta x)\ A(j\Delta x)\ \cos(2\pi\nu j\Delta x)\ N(j\Delta x) \\ & \cdot (2\Delta x)\ A(k\Delta x)\ \cos(2\pi\nu' k\Delta x)\ N(k\Delta x)\Big\rangle \end{aligned} \tag{65}$$

$$= \sum_{j=-M}^{M} (A(j\Delta x))^2 \cdot \frac{n^2\cdot(\Delta x)^2}{t(j\Delta x)}\ \{\cos(2\pi(\nu-\nu')\ j\Delta x) + \cos(2\pi(\nu+\nu')\ j\Delta x)\} \ .$$

Reproduced with permission of the copyright owner. Further reproduction prohibited without permission.

For $\nu = \nu'$ we ignore the second cosine and obtain

$$\langle \bar{N}^2(\nu) \rangle = n^2 \sum_{j=-M}^{M} |A(j\Delta x)|^2 \cdot \frac{(\Delta x)^2}{t(x)} \simeq n^2 \int_{-L}^{L} |A(x)|^2 \, V(x) \, dx \quad , \tag{66}$$

where $V(x) = \Delta x/t(x)$ is the velocity at x. In the simplest case $A = 1$, and $V = 2L/T$, where T is the total time used. The nominal resolution is then $\Delta\nu = 1/2L$, so

$$\sqrt{\langle N^2(\nu) \rangle} = (1/\Delta\nu) \cdot (n/\sqrt{T}) \quad . \tag{67}$$

This result shows the very simple and important result that the observed noise increases in proportion to the number of resolution elements per wavenumber, decreases in proportion to the square root of the observing time, and is independent of the total frequency range observed.

To optimize the function V(x), I set up a variational calculus problem. Following the prescription of L. P. Smith (1953, p. 404), I found immediately that the best function V(x) is proportional to the reciprocal of A(x). That is to say, the observing time at each point is proportional to the apodizing function at that point, so that $A(x)\ V(x) = \text{const}$.

If this kind of velocity function is chosen, then the correlation function $\langle \bar{N}(\nu)\ \bar{N}(\nu') \rangle$ simplifies to become

$$n^2 \cdot (A(x)\ V(x)) \cdot [R(\nu - \nu') + R(\nu + \nu')] \tag{68}$$

There is one case of special interest, the one with $A_o(x) = 1$. When this is the case, $R_o(\nu \pm \nu') = 0$ if $\nu \pm \nu' = m/2L$, where m is an

Reproduced with permission of the copyright owner. Further reproduction prohibited without permission.

integer. We usually compute our spectra for just such a set of frequencies, so that the noises on the output spectrum points are uncorrelated.

Reproduced with permission of the copyright owner. Further reproduction prohibited without permission.

V. SUBMILLIMETER BOLOMETERS

This chapter reports on the methods we have developed for making and testing bolometers for the far infrared and submillimeter regions. Bolometers made of germanium, silicon and indium antimonide are compared with a Golay cell, and efficiencies are determined by calibration of an infrared source. Our development of immersion optics for illuminating bolometers is described. Attempts to make InSb detectors and to blacken silicon bolometers with conducting films are discussed.

The subject of submillimeter detectors has been reviewed in an excellent reprint volume by Arams (1973). Papers included cover the period from 1949, when Golay published a description of this pneumatic detector, up to 1970. A reference list is given for detectors, spectrometers, and for optical materials.

The submillimeter region is still miserably instrumented by comparison to other spectral regions. The frequency is too high for the use of coherent detectors, because of the lack of tunable sources as well as the difficult materials and fabrication problems. On the other hand, the frequency is too low to permit the use of photon detectors. Photon energies are not large compared to thermal energies at convenient temperatures, and physical systems with the appropriate energy gaps are superconductors or very highly doped semiconductors. Indium antimonide is a free electron photoconductor in the submillimeter region, but has not yet been made in pure enough form to be an impurity photoconductor.

In default of other methods we therefore degrade our radiation to heat and measure that. The frequency of the radiation is small

Reproduced with permission of the copyright owner. Further reproduction prohibited without permission.

(20 cm^{-1}) compared to typical thermal radiation to which we are accustomed (1000 cm^{-1} for thermal infrared and 20,000 cm^{-1} for visible light). The radiation power available from thermal sources with constant fractional bandwidth is therefore smaller by five to nine orders of magnitude.

Far infrared physics did not progress until sensitive thermometers were developed. Golay's room temperature pneumatic detector comes close to fundamental sensitivity limits (Golay, 1949). It minimizes heat capacities by the use of very thin heat absorbing materials, and uses a gas thermometer with a very sensitive optical amplifier. Cryogenic detectors have the potential of vastly improved performance because heat capacities are diminished while temperature sensitivities are increased.

Early cryogenic detectors were already a great improvement over the Golay cell. Boyle and Rodgers (1959) describe a carbon bolometer. Germanium bolometers developed by F. Low (1961) are much less noisy. Silicon bolometers have also been made, and are faster than germanium because of lower heat capacities. InSb detectors are electron photoconductors which behave like fast bolometers.

More recently several workers have made composite bolometers which separate the temperature sensing function from the radiation absorption function. These bolometers have lower heat capacities, which permit higher responsivities at reasonable chopping frequencies. Germanium thermometers have been coupled to radiation collectors by F. Low (pers. commun.) and by N. Coron, G. Dambier and J. Leblanc, who are making them for sale.

Reproduced with permission of the copyright owner. Further reproduction prohibited without permission.

Superconducting junction thermometers for bolometers have been described by Clarke, Hoffer and Richards (1973) and by M. Hauser (pers. commun.).

A. Detector Calibration Methods

We have developed calibration procedures for testing our detectors. While it is easy to determine the response of a detector to absorbed power, merely by measuring its electrical properties, it is not as easy to measure its absorptivity. We had neither calibrated sources nor calibrated detectors when we started our program. Estimates of source brightness and detector sensitivity predicted signals more than an order of magnitude larger than observed. The results of our calibrations are that the sources and the detector systems are each about 1/4 as good as previously thought.

The methods which we used to obtain these results are detailed in the sections below. In Section 1 I describe the calibration of the light sources. In Section 2 I discuss the transmissions of light pipes, windows, and filters. In Section 3 I define effective throughput. In Section 4 I give the formulas I used for determining bolometer properties.

1. Calibrating Light Sources

Our calibrated light source is the Michelson Fourier spectrometer described by R. R. Joyce (1970). A spectrometer is very helpful because almost all of the detectors we study have important frequency dependences in the submillimeter region. These dependences are clues to the loss mechanisms which reduce sensitivity. Moreover, the spectrometer makes possible monochromatic measurements, so that filters

Reproduced with permission of the copyright owner. Further reproduction prohibited without permission.

which are incidental to the operation of the detectors do not need to be precisely measured.

This spectrometer has an internal quartz mercury arc lamp source (G. E. number UA-3), 15 cm diameter optics, a choice of Mylar beam-splitters, an f/1.0 output beam into a brass light pipe of 1.1 cm inside diameter, a variable frequency light chopper, and a set of low-pass filters on a filter wheel.

Since we did not initially have a calibrated detector, we could not calibrate the standard spectrometer. However, when we built a second spectrometer for the balloon flight we were able to calibrate both spectrometers and the detector. First, we use the second spectrometer and the detector to observe a black body source of known temperature. The source is connected to the second spectrometer by a light pipe and collimator. Measurement of the spectrum of this black body source calibrates the system comprised of the second spectrometer and detector.

This calibrated system is then used as a detector for the original spectrometer which is to be calibrated. For any setting of the first spectrometer, a spectrum can be made with the second spectrometer. However, if the first one is an ideal Fourier transform device, only one spectrum is necessary to describe its performance, since all the energy transmitted is modulated in a known way as the path difference is varied. The first spectrometer is a conventional Michelson interferometer having an ideal transmission of the form

$$t_2(x,\nu) = \frac{1}{2}(1 + \cos(2\pi\nu x))\ 2t_1(\nu)$$

Reproduced with permission of the copyright owner. Further reproduction prohibited without permission.

as a function of frequency and path difference. Here $2t_1(\nu)$ is the transmission of the device when set at $x = 0$, in whatever units the input and output of this black box are measured in. For frequencies below 50 cm^{-1} our device appears to have this ideal behavior, as evidenced by the form of the interferograms.

The result of a calibration with a black body is conveniently expressed in terms of the antenna temperature of the radiation coming from the standard source, as described in Section III-D-1. The calibration has been made several times using different configurations of the second spectrometer and detector. The results for the standard case (0.0127 cm Mylar beamsplitter, source set to zero path difference, frequency 12 cm^{-1}, no low pass filter) have ranged from 350K to 600K above the ambient temperature. The low value was obtained only a few days before the arc light source wore out and was replaced.

A sample brightness spectrum is shown in Fig. 26. This spectrum was obtained with a 0.0127 cm beamsplitter, and the auxiliary spectrometer was the polarizing Michelson interferometer built for the balloon, operated in air with an InSb cryogenic detector. The spectrum has been smoothed by hand to show the major features. The modulation with period 25 cm^{-1} is due to interference effects in the beamsplitter. A nonuniform beamsplitter thickness would reduce the signal at 12 cm^{-1} and increase it at 25 cm^{-1}. Since the signal is zero at 25 cm^{-1}, we conclude that the beamsplitter is uniform. The modulation with period 2.5 cm^{-1} is due to interference in the transparent arc lamp envelope. The gradual drop at high frequency is presumed due to absorption in the Mylar beamsplitter and in the brass light pipe, and to overlapping water vapor lines, while

Reproduced with permission of the copyright owner. Further reproduction prohibited without permission.

Reproduced with permission of the copyright owner. Further reproduction prohibited without permission.

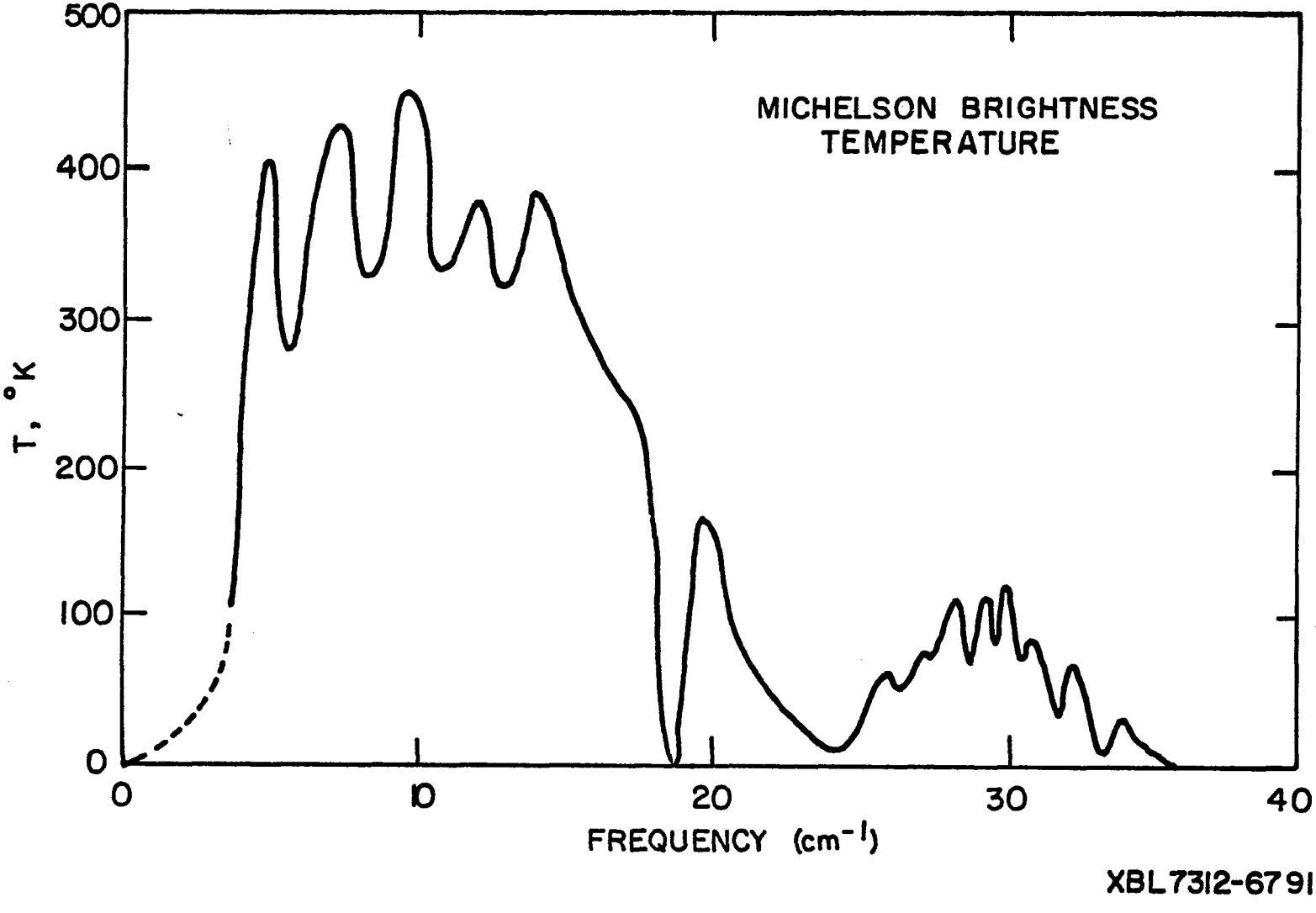

Fig. 26. Brightness of laboratory Michelson interferometer.

the sharp absorption at 18 cm^{-1} is a single water vapor line.

The existence of detectors with uniform frequency response makes it possible to transfer this calibration curve to other frequencies, beamsplitters, and filter combinations. Our working standard is a Golay cell, described below in the test results section. Its design is inherently independent of frequency, and it has been compared with several other detectors also thought to have uniform response. In addition, its factory calibration made in the thermal infrared appears to agree with our own made at 12 cm^{-1}.

The output beam temperature may be interpreted in terms of the arc lamp physical temperature and the efficiency of the Michelson interferometer. The interferometer is estimated to have losses through shadowing (t = 0.8), absorption in the beamsplitter (t = 0.8 at 12 cm^{-1}), and calculated beamsplitter efficiency due to reflectance (t = 0.66 at 12 cm^{-1}). Our highest output beam temperature was 600K hotter than room temperature, which would result from a lamp temperature of 1700K. This number is only 1/4 to 1/2 of the values reported elsewhere for arc lamps (Robinson, 1973, p. 14). The remaining discrepancy may be due to the length of light pipe on the output, to discontinuities in the pipe where chopper blades and filter wheels pass through, to operating the lamp in air with its envelope removed rather than in high vacuum, or to the age of the lamp.

Our computer program computes the function $S(\nu)/4\Delta x$ from an interferogram, where $S(\nu)$ is the desired spectral power data, and x is the interferogram path difference sampling interval. This question is

Reproduced with permission of the copyright owner. Further reproduction prohibited without permission.

discussed in more detail in Chapter IV. Our interferograms are always measured in counts from a digitizer, which correspond to certain r.m.s. signal values at the detector. To find the power absorbed by the detector in watts per cm^{-1}, I use the following formula:

$$P_\nu\left(\frac{W}{cm^{-1}}\right) =$$

$$\frac{\left[\frac{S(\nu)}{4\Delta x}\left(\begin{matrix}\text{counts from}\\ \text{computer}\end{matrix}\right)\right] \cdot [4\Delta x] \cdot [\text{lockin amplifier scale, volts}]}{[\text{digitizer gain, counts for full scale lockin}] \cdot [\text{Responsivity, V/W}]}$$

In this formula, I need to know the detector power responsivity, which is calculated as described below in the section devoted to it.

The effective brightness temperature of the Michelson interferometer will be taken for subsequent computations to be 400K, relative to room temperature, measured at 12 cm^{-1}, set to zero path, with no filter, and the chopper open. However, to know how to use this number to compute what the detector will measure, we have to allow for the modulations by the Michelson interferometer and the chopper. The first correction is a division by 2, since only half of the radiation transmitted by the interferometer is multiplied by $\cos(2\pi\nu x)$. This is purely definitional and is chosen to agree with Chapter IV. There is another factor which is also about 1/2, which is due to the chopper. The chopper interrupts the beam and we therefore look at the source for only 1/2 of the time. Moreover we detect only the fundamental component of the resulting waveform with our lock-in amplifier. The result of this is that, for square-wave chopping, the peak-to-peak to r.m.s. conversion factor

Reproduced with permission of the copyright owner. Further reproduction prohibited without permission.

is $\sqrt{2}/\pi$, or 0.45. The net output beam temperature of the spectrometer is then only 90K, r.m.s., modulated. At 12 cm^{-1}, this corresponds to a spectral intensity $F_\nu = 2kTc\nu^2 = 1.07\times10^{-10}$ $W/cm^2sr\ cm^{-1}$. This is the quantity which we will compare with the power which we detect with the detector.

2. Filters, Pipes and Windows

In order to transport light to our detector we generally use oversize waveguide of polished brass. Performance of such light pipe was reported by P. L. Richards (1964). A length of brass tubing 1.1 cm in diameter and 1 m long transmits about 0.8 of the radiation at 20 cm^{-1}.

We also use windows between sections of our pipe. We typically use black polyethylene 0.0127 cm thick. This is so thin that it transmits about 0.94 at 12 cm^{-1}, according to our measures. Bolometers (except for InSb detectors) operate in vacuum spaces and we use sapphire and Mylar vacuum windows. Sapphire has a high refractive index (3.2) and therefore has a loss of 28% per surface due to reflection. With a two-surface window the transmission is 0.52. Our windows are wedge shaped to eliminate coherent effects of interference between the two surfaces. The prismatic effect deviates the beam slightly. Mylar windows are nearly transparent, especially when thin and cold.

Cold low-pass filters are also necessary, especially for sensitive and intrinsically broadband detectors. In the absence of such filters, incident room temperature radiation raises the detector above its optimum operating temperature. Our InSb detectors work well enough with only black polyethylene, since they do not detect radiation

Reproduced with permission of the copyright owner. Further reproduction prohibited without permission.

between 50 and 2000 cm^{-1}. Other detectors are protected with "Yoshinaga" filters (powder reststrahl filters, described by Yamada, et al., 1962), or with Fluorogold (Muehlner and Weiss, January 1973). The transmissions of these filters are both high, about 0.8 at 12 cm^{-1}, and both cut off completely at about 50 cm^{-1}.

3. Effective Throughput

In order to determine the absolute efficiency of an infrared detector system, we must know how much radiation it detects and how much is falling on it. The first part is easily determined from the observed signal and an electrically measured responsivity, or from a factory calibration. The second part requires knowing the source brightness, the efficiency of the transfer optics, and the size and angular response of the detector. This subject is called photometry, and a brief introduction is given by Born and Wolf (1970), p. 181.

I will start by writing down the answer. The power P_{inc} incident on the detector is

$$P_{inc} = \int B\cos\theta d\Omega dA \quad ,$$

where the integration is carried across the surface A of the detector and the solid angle Ω at each point of the detector, where B is the incident radiation brightness in W/cm^2 sr as a function of position and angle, and where θ is the angle of incidence, measured from the normal. If B is a constant over the detector area and angles, then we can unambiguously define the throughput

$$A\Omega = \int \cos\theta d\Omega dA$$

Reproduced with permission of the copyright owner. Further reproduction prohibited without permission.

so that $P_{inc} = BA\Omega$. In an even more special case, the range of angles illuminated is independent of the position on the detector. Then we can factor the integral further and separately define A and Ω. The ultimate simplicity is the plane detector illuminated from all angles on one side only. Then $A\Omega = \pi A$.

The throughput concept has great usefulness. If a small bundle of rays with brightness B is traced through a lossless optical system, then the quantity B/n^2 is an invariant along the trajectory, where n is the refractive index. This may be shown separately for reflections and refractions. To see that the factor $1/n^2$ is needed, one may consider a bundle of rays passing through a point on a surface of a dielectric. Snell's law $n_1 \sin\theta_1 = n_2 \sin\theta_2$ connects the incident and refracted angles. For normal incidence, the divergence of the ray bundle is proportional to $1/n$ and the solid angle to $1/n^2$. Conservation of energy implies that the brightness B increases in proportion to n^2. For non-normal incidence, more exact application of the law proves the same result.

In consequence, the quantity $\int n^2 \cos\theta d\Omega dA$ is also an invariant of the bundle of rays. It may be evaluated for any convenient surface which intersects the entire bundle just once. As a trivial example, consider two small surfaces A_1 and A_2, say a source and a detector, separated by a distance r and perpendicular to the line joining them. Let the ray bundle consist of all rays which join points on A_1 with points on A_2. If the throughput is evaluated at A_1, then the solid angle of the rays striking each point on A_1 is given by $\Omega = A_2/r^2$. Then the

Reproduced with permission of the copyright owner. Further reproduction prohibited without permission.

throughput is $A\Omega = A_1A_2/r^2$. The same result is obtained when the evaluation is made at the surface A_2, as is evident from the symmetry of the answer in the indices 1 and 2.

The throughput also has significance in wave optics. The effective number of spatial and polarization modes received by a detector is $2\nu^2A\Omega$, where ν is the spatial frequency in the medium, $\nu = nf/c$, and f is the frequency in Hz. To illustrate this, consider black body radiation in a cavity, and compare it with Johnson noise in resistors. These are essentially identical physical processes in different geometries. In a black cavity at temperature T, the spectral power crossing a surface of area A in a solid angle Ω is

$$\frac{dP}{df} = (kT)(2\nu^2A\Omega) \quad ,$$

in the Rayleigh-Jeans limit. For comparison, consider two resistors connected by a transmission line to which they are both matched. In other words they are black, reflecting none of the power incident on them. Each resistor emits and absorbs a spectral power $\frac{dP}{df} = kT$, in the low-frequency limit. Comparison of these two formulas shows that the surface exposed to radiation receives $2\nu^2A\Omega$ as much as the resistor. The factor 2 arises from the two possible polarizations in space, while there is only one propagated in a transmission line.

The transmission line can be terminated with a matched antenna enclosed within the black body cavity. Then the resistor still emits and absorbs the same amounts of power as before. This result is independent of the size, shape, and construction details of the antenna, as long as it is matched to the load by some network. It has a

Reproduced with permission of the copyright owner. Further reproduction prohibited without permission.

throughput of one square wavelength, and receives only one polarization.

What we are concerned with, of course, is the question of detector efficiency ϵ_{det}. In general, this efficiency is a function of position and incidence angle. When we measure an efficiency, we form the average quantity $\bar{\epsilon}_{det} = P_{abs}/P_{inc}$. P_{inc} has already been defined as $\int B\cos\theta d\Omega dA$, while P_{abs} is $\int B\epsilon_{det}\cos\theta d\Omega dA$. It is generally the case that B is also a function of position and angle, so we get a weighted average efficiency.

In our work we rarely know these details. Light from the source spectrometer passes down a light pipe into a cryostat, through filters, windows, condensing cones, and sometimes lenses or mirrors, before finally reaching the detector. Sometimes the detector is enclosed in a metal integrating chamber. The properties of these elements are amenable to approximate computation.

On a microscopic scale, an ideal pipe preserves the throughput of a sufficiently small ray bundle. On the macroscopic scale, it scrambles the ray bundles. A ray in a round pipe has two invariants of the motion, the angular momentum L_z about the axis of the pipe, and the angle θ which the ray makes with a line parallel to the pipe. This angle is related to the transverse component of the momentum which is also invariant. Therefore, those brightness distributions B which are functions of these invariants alone will be propagated unchanged in the pipe. For a lossy pipe, the loss per unit length of pipe is also a function of these invariants only. Under most circumstances, our brightness distributions are functions only of θ.

Reproduced with permission of the copyright owner. Further reproduction prohibited without permission.

Similar considerations apply to condensing cones. A long thin cone preserves a brightness distribution B which is a function of the invariants L_z and L^2, where L_z is the angular momentum about the axis and L^2 is the square of the angular momentum about the center of the image ball, as discussed in Section II-B-7. The effect of the cone can be more intuitively evaluated by simply drawing the image ball and removing the cone. We often operate these cones in such a way that the incident brightness is a constant over the appropriate range of variables. In other words, we overfill the detector. Then the throughput is simply πA, where A is the area of the small end of the cone.

In most of our detector studies we simply assume that B is not dependent on position or angle on the detector. We know that this is not true, but we desire to include the failure of the approximation in the efficiency of the detector. We take the brightness to be the measured output brightness of the source, multiplied by the transmissions of the lightpipes, window, and filters. By the same token, we take the throughput to be just $n^2 A\pi$, where A is the illuminated area of the detector and n is the index of refraction of the medium in which the detector is immersed. In those cases where a large detector is enclosed in an integrating cavity with a smaller aperture, the area of the opening has been used.

There are some detectors for which we have actually measured the throughput. The Golay cell, which we use as a standard, is not illuminated from a full hemisphere, but we do know its geometric size. We calibrate it in the configuration shown in Fig. 27a, where we know the solid angle Ω by construction. This calibration is then transferred to the usual operating configuration in (a'). The increased signal

Reproduced with permission of the copyright owner. Further reproduction prohibited without permission.

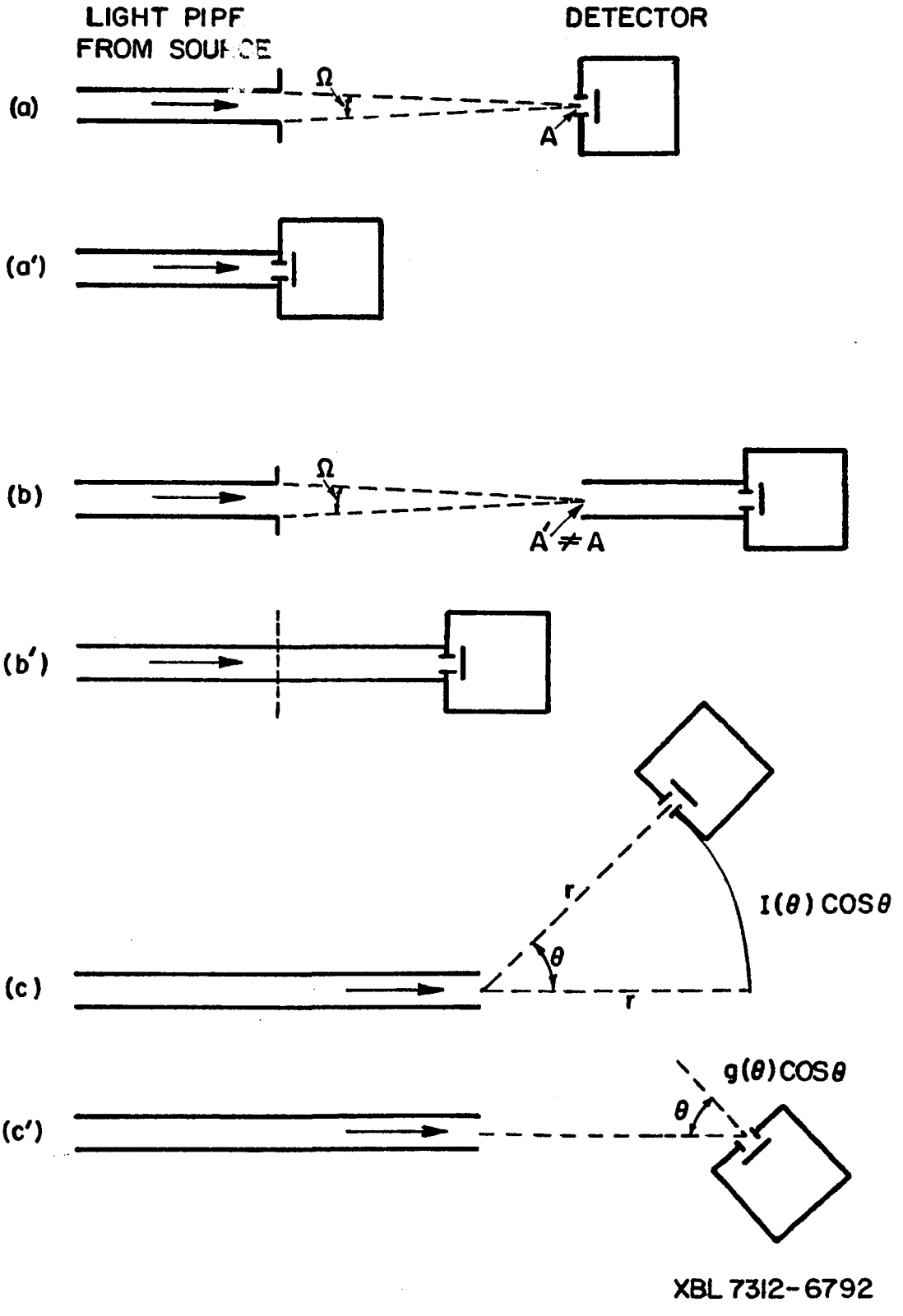

Fig. 27. Detector throughput calibration.

Reproduced with permission of the copyright owner. Further reproduction prohibited without permission.

level is attributed to an increase in effective solid angle.

As an example of the scrambling effect of a light pipe, consider the case shown in (b). Here we calibrate an entire detector system, consisting in this case of a Golay cell together with a length of light pipe. In calibrating this system we must take the area of the pipe as the effective area of the system. The pipe prevents forming an image of a source directly on the detector, and scrambles the light until it is uniformly distributed across the aperture. When we observe this detector system in configurations (b) and (b'), the responses are the same as in cases (a) and (a') respectively. However, we interpret the system in (b) as having larger throughput by the ratio A'/A, and by the same token lower responsivity or efficiency. The practical significance is that the bare Golay cell is better for those sources which are not large enough to illuminate the full area of a light pipe.

The method described above for finding the effective solid angle is simple. A method which is equivalent in principle and gives more detail is shown in Fig. 27, (c) and (c'). The incident brightness distribution $I(\theta)$ is measured as shown in (c). In our systems I is a function only of θ. The detector system responsivity is $g(\theta)$ which is also a function only of θ. The direct results of the scans shown must be corrected for the area projection factor $\cos\theta$. Typical uncorrected results are shown in Fig. 28 for the source, the Golay cell, and the detectors used with germanium cones.

Using the brightness and responsivity curves, one constructs the integral for effective solid angle

Reproduced with permission of the copyright owner. Further reproduction prohibited without permission.

Reproduced with permission of the copyright owner. Further reproduction prohibited without permission.

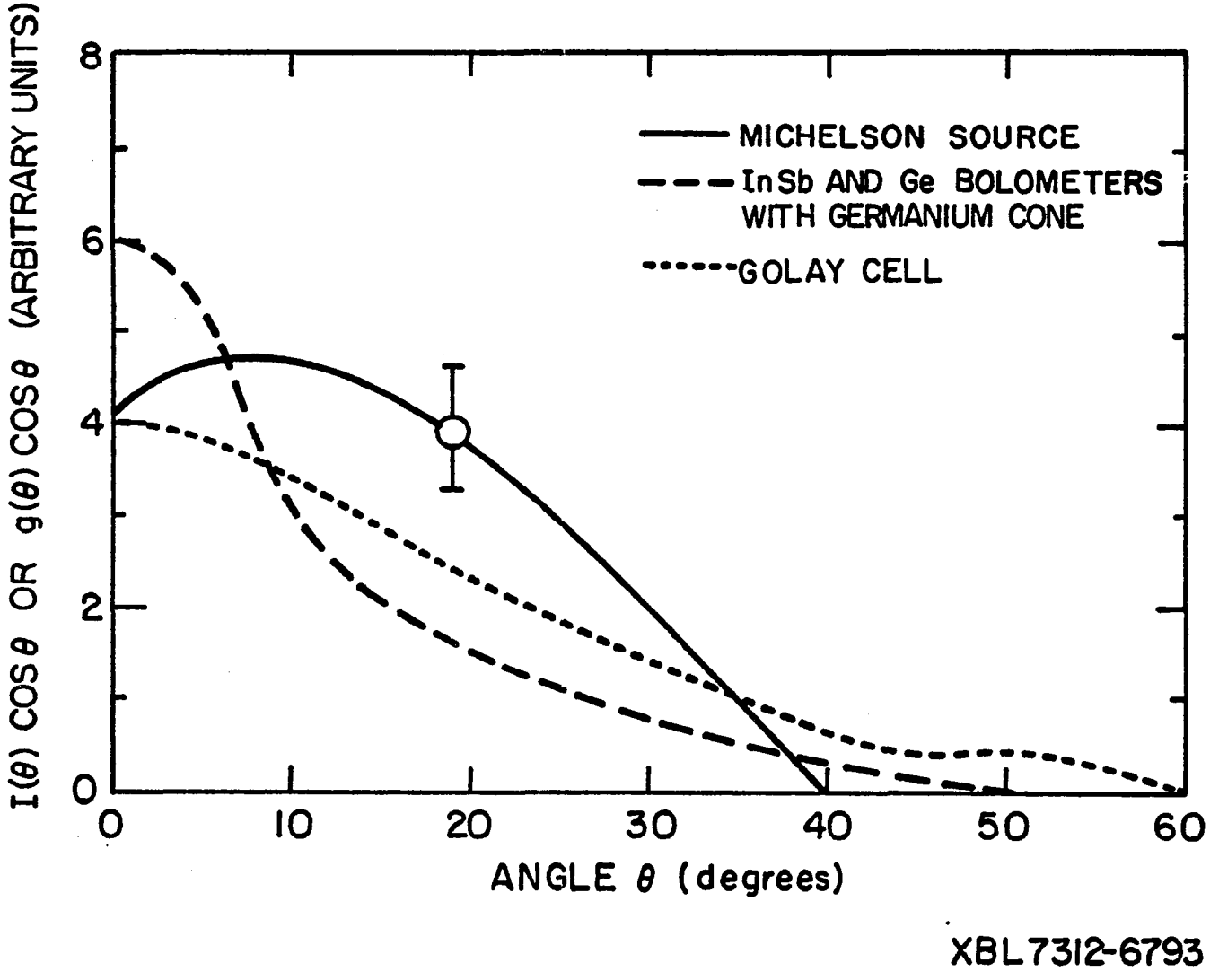

Fig. 28. Angular response of source and detectors.

$$\Omega_{eff} = 1/(g(0)\ I(0)) \int g(\theta)\ I(\theta)\ \cos\theta d\Omega$$

where $d\Omega = 2\pi \sin\theta d\theta$. This integral can be numerically evaluated for the curves shown in Fig. 28. If the measurements are correct the effective solid angle should be the same as determined from (a), (a'). For the Golay cell, the numerical integral gave 0.4 sr, while the direct measure gave 0.7 sr. For the detectors with germanium cones, the integrated solid angle was 0.25 sr, which is in agreement with the theoretical value, but it was not measured directly.

It is implicit in this pair of methods that the efficiency and effective responsivity of the detector system is determined for axial rays. When off-axis rays are to be detected, the curves in Fig. 28 must be used to estimate corrections to the efficiency. The practical significance becomes clear when the detector used in the balloon-borne spectrometer is considered. It is illuminated by an f/2 lens, which illuminates it evenly out to 15° from the axis and no farther. Only one third of the solid angle integral is contained within this limit.

4. Measurement of Bolometer Characteristics

Our cryogenic bolometers are all temperature sensitive resistors, characterized by a resistance R(T). For germanium and silicon bolometers the temperature of importance is the crystal lattice temperature, while for InSb bolometers it is the electron temperature, which can be very different. In the ideal case, each is also characterized by a single heat capacity C(T) of the bolometer and a definite thermal link to a heat sink at temperature T_{bath}.

Reproduced with permission of the copyright owner. Further reproduction prohibited without permission.

Fortunately for the experimenter, these details do not need to be understood to measure the sensitivity of the detector. An extended discussion of these matters is given by R. C. Jones (1953). Jones gives two methods, one based on the I-V plot and one based on a special bridge circuit. I have simplified both methods and present the results below.

We make the assumptions that power delivered electrically to the detector has the same effect as power delivered by incident radiation, that the detector chip is isothermal, and that the resistance is characterized by a temperature, independent of electrical bias. The third assumption can be questioned, especially with InSb detectors, where noisy contacts are nonohmic (R. Weiss, personal communication).

On the basis of these assumptions I derive the electrical power sensitivity from two measurements. First, I measure the DC voltage vs current dependence of the bolometer (the I-V plot). The low-frequency responsivity of the bolometer can be determined from the shape of this curve, as shown below. Second, I measure the effective time constant of the bolometer by using an optical input power which can be chopped at a variety of frequencies. I can then calculate the responsivity at any chopping frequency. The alternative method is presented later.

To find the following formulas, I solved the heat balance equations with time-dependent quantities. The equations are derived from the electrical and thermal circuits shown in Fig. 29 (a,b). The equations are just the electrical laws $E_s = IZ_s + E$, with $E = R(T) \cdot I$, and the heat balance equation

Reproduced with permission of the copyright owner. Further reproduction prohibited without permission.

$$C \frac{dT}{dt} = -Q(T,T_{bath}) + EI + P_{in} \quad .$$

The quantities E, I, R, T and C are respectively the voltage, current, resistance, temperature and heat capacity of the bolometer element. The DC bias source voltage and impedance are E_s and Z_s. The optical input power to the bolometer is P_{in}, and $Q(T,T_{bath})$ is the power conducted from the bolometer to the thermal sink at temperature T_{bath}. The angular frequency ω is $2\pi f$, where f is the chopping frequency. The bolometer presents an apparent impedance to the outside world which is called $Z_B(\omega)$, abbreviated to Z_B when $\omega = 0$. Z_B is the slope of the I-V plot.

The results of my calculations, cast in terms of easily measurable quantities, are that the power responsivity $\mathcal{R}(\omega)$ measured in volts/watt and the effective time constant $\bar{\tau}$ (sec) are given by

$$\mathcal{R}(\omega) = \frac{dE}{dP_{in}} = \mathcal{R}_o/(1 + i\omega\bar{\tau}) \quad ,$$

where

$$\mathcal{R}_o = \frac{1}{2I_o} \frac{\frac{Z_B}{R} - 1}{\frac{Z_B}{Z_s} + 1} \quad ,$$

and

$$\bar{\tau} = \frac{C}{2G} \frac{\left(\frac{Z_B}{R} + 1\right)\left(\frac{R}{Z_s} + 1\right)}{\left(\frac{Z_B}{Z_s} + 1\right)} \quad .$$

Reproduced with permission of the copyright owner. Further reproduction prohibited without permission.

We usually operate our bolometers with $Z_s >> Z_b$, R, and we adjust the bias so that the responsivity is near maximum. For curves similar to Fig. 29(c), this occurs at a point where Z_B/R is of the order of 1/2. At this point the responsivity is $\mathcal{R}_o = 1/4I$.

Note that the effective time constant of the bolometer is not C/G as might have been expected, but is changed by electrical-thermal feedback effects. For large Z_s and with $Z_B = 0$, which is possible with our bolometers, the time constant is reduced by a factor of two. I have seen this effect with a germanium bolometer, in which increasing the bias current reduced the time constant. This occurred despite the temperature dependence of C/G, which predicts a change in the opposite direction. C/G is proportional to T^2 for typical devices.

The equivalent circuit in part (d) of the figure is given by Jones. This circuit has the property of having the same electrical impedance as the bolometer at all frequencies, and moreover, it gives the correct output signal level where the voltage e is given simply by $P_{in}/2I$.

I calculated the value of this electrical impedance and of the equivalent circuit parameters R_N and L as functions of measured parameters. They are

$$Z_B(\omega) = Z_B \frac{1 + i\omega\frac{C}{G}\,\frac{Z_B + R}{2Z_B}}{1 + i\omega\frac{C}{G}\,\frac{Z_B + R}{2R}} \quad ,$$

$$R_N = Z_B R/(R - Z_B) \quad ,$$

Reproduced with permission of the copyright owner. Further reproduction prohibited without permission.

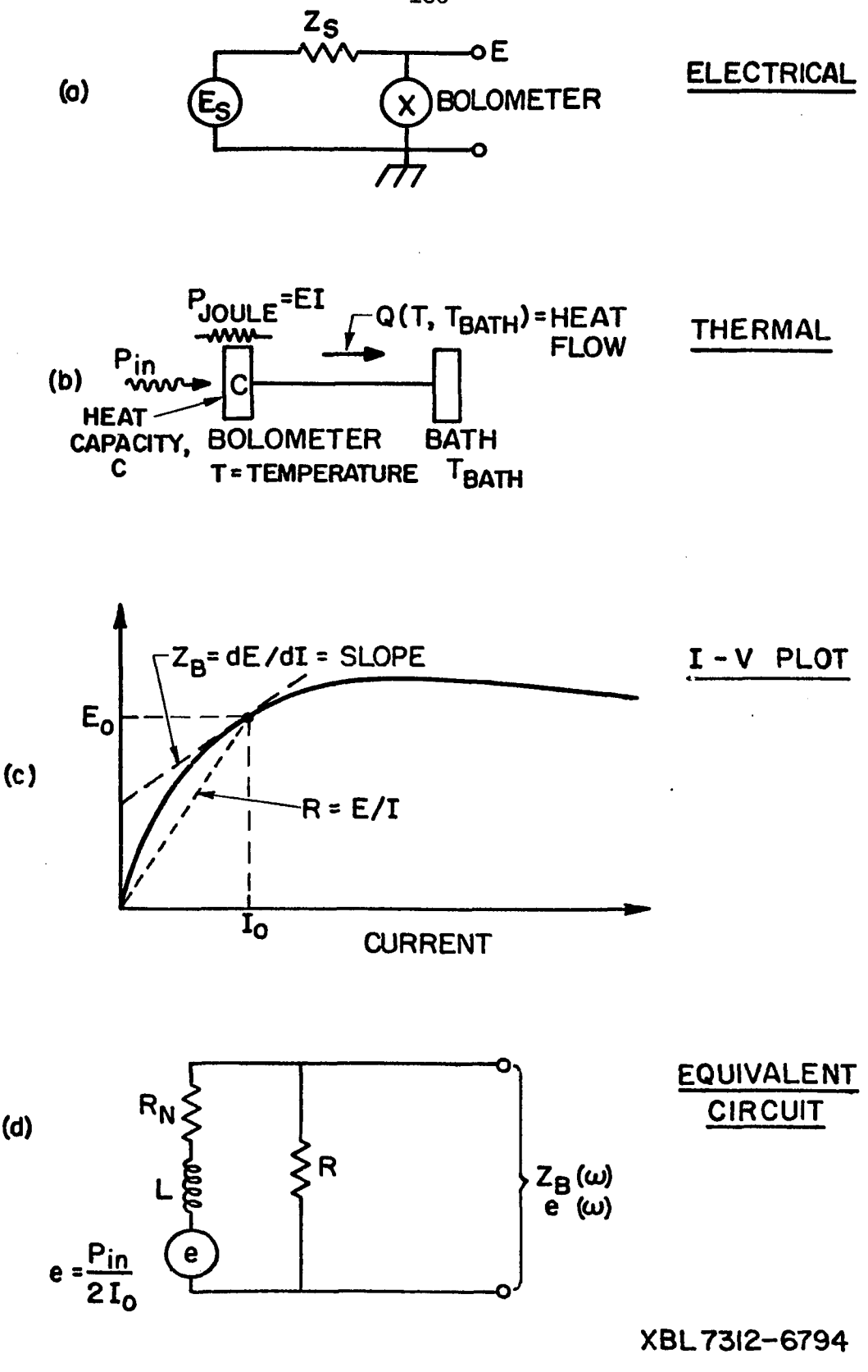

Fig. 29. Bolometer definitions.

Reproduced with permission of the copyright owner. Further reproduction prohibited without permission.

and

$$L = R \cdot \frac{C}{2G} \cdot \frac{R + Z_B}{R - Z_B} \quad .$$

In the case of $Z_s >> Z_B$, R we find

$$\frac{L}{R} = \bar{\tau} \cdot \frac{1}{1 - \frac{Z_B}{R}} \quad .$$

I will simply quote here Jones' result for a purely electrical means of determining the responsivity. Figure 30 shows the bridge circuit used. The resistor R_L is the load resistance called Z_s above. A new symbol is used to emphasize that R_L is a pure resistance, which was not previously assumed. The resistors R_1, R_2 are chosen to balance the bridge for DC. The result is that

$$\mathcal{R}(\omega) = \frac{1}{2I}\left(1 + \frac{R_L}{R}\right) \frac{e_B(\omega)}{e_A(\omega)}$$

I simplified Jones' result by introducing the quantity e_2, the AC voltage across R_2, and found that

$$\mathcal{R}(\omega) = \frac{1}{2I} \frac{e_B(\omega)}{e_2(\omega)} \quad .$$

This method can be used even at those frequencies where $\omega\bar{\tau}$ is large and hard to determine well by varying an optical chopping frequency.

To use this method, R_1 and R_2 do not need to be known. First, the DC voltage e_3 is set to zero by adjusting R_1 and R_2. Then the DC voltage e_1 determines the current I since R_L is known. Then the

Reproduced with permission of the copyright owner. Further reproduction prohibited without permission.

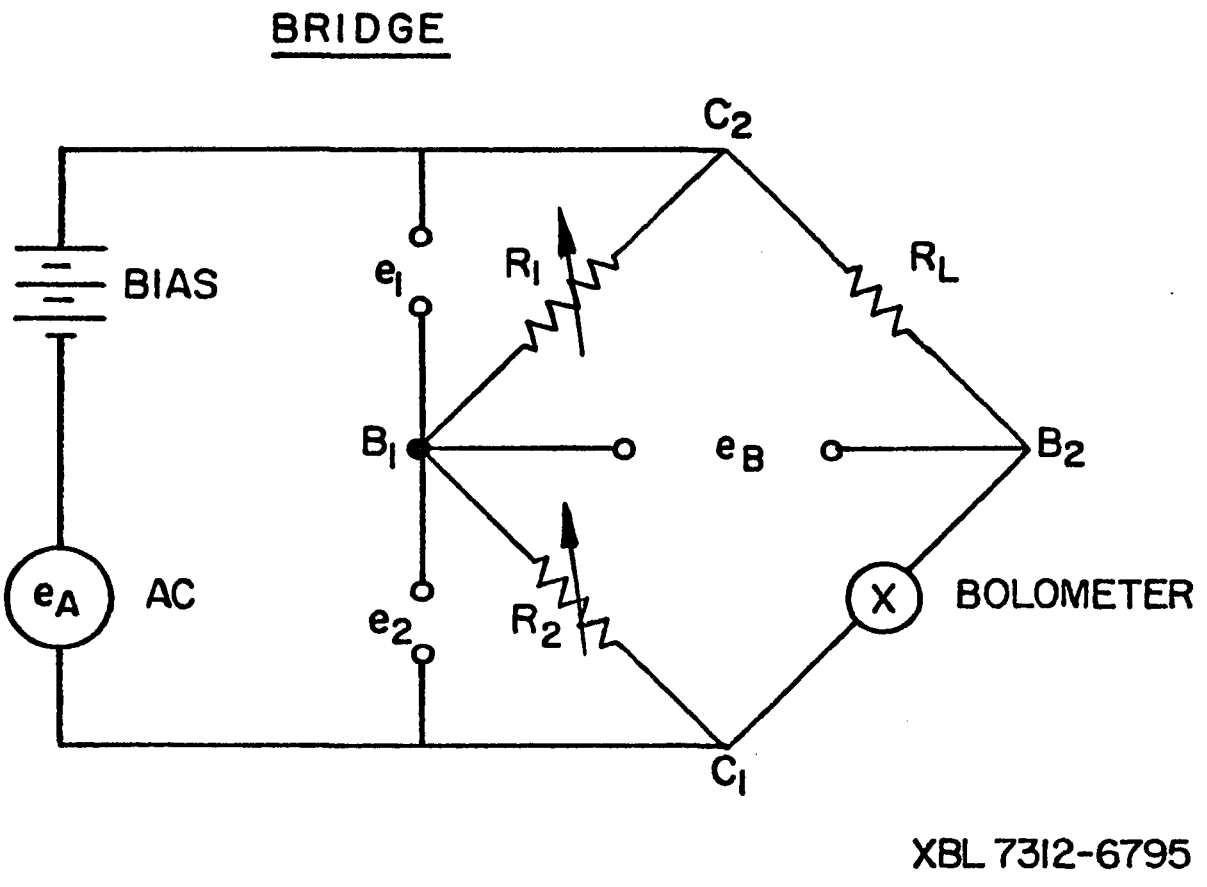

Fig. 30. Jones' bolometer bridge.

Reproduced with permission of the copyright owner. Further reproduction prohibited without permission.

responsivity is found from measuring the AC voltages e_2 and e_B. The point B1 is a common point for all the measurements and could be grounded for experimental convenience.

While it is not necessary to know either C or G to find out the responsivity, they are of interest in designing bolometers. The ratio C/G, which is related to the effective time constant, can be determined from measurement of three quantities, since the equivalent circuit for the bolometer has three independent parameters.

To determine C and G separately, a temperature dependence must be measured. The easiest to measure is the R(T) function. This is done with a ohmmeter and a varying helium bath temperature. The ohmmeter must have sufficient sensitivity that it does not heat the bolometer significantly. If gas or liquid helium is admitted to the chamber of the detector, larger powers are permitted. If the temperature derivative of R(T) is called R', then

$$G = I_o^2 R' \left(\frac{Z_B}{R} + 1\right) / \left(\frac{Z_B}{R} - 1\right)$$

may be used to compute G. The quantity $Q(T,T_{bath})$ may also be computed directly from the I-V plot and R(T), and then differentiated to find G.

For typical metallic thermal links made of wire, the variation of G has a simple form. The Wiedemann-Franz law says that the thermal conductivity of metal is a constant times the temperature times the electrical conductivity: $k = L'\sigma T$ (Kittel, 1966, p. 222). For a wire thermal conductor connecting the bolometer at T to the bath at T_{bath}, the solution to the heat flow equations turns out to be simple: the

Reproduced with permission of the copyright owner. Further reproduction prohibited without permission.

mean thermal conductivity is found from the above formula with the temperature $\bar{T} = (T + T_{bath})/2$. Then $Q(T,T_{bath}) = (T^2 - T_{bath}^2)(L'/2r)$, where r is the electrical resistance of the wire and L' is the Lorenz constant, 2.45×10^{-8} W-ohm/deg^2. Then the derivative of Q is G, which is just $G = L'T/r$, and the bath temperature drops out of the equations. It is thus seen that there are two factors which make the bolometer faster than it might have been, the feedback effect and this fact that G is larger than might be expected.

The heat capacity of a helium-temperature detector element also has a simple temperature dependence, the Debye T^3 law (Kittel, p. 178). The lattice heat capacity of a substance is $C = 234\ Nk\ (T/\theta_D)^3$, where N is the number of atoms, and θ_D is the Debye temperature. For engineering purposes it is useful to have this formula in terms of unit volume and express it in terms of v_s, the effective velocity of sound. Then

$$C = \left\{k \cdot \frac{234}{6\pi^2}\left(\frac{k}{\hbar}\right)^3\right\}\left(\frac{T}{v_s}\right)^3$$

per unit volume, where

$$v_s = (k\theta_D/\hbar)(6\pi^2 n)^{-1/3} \quad ,$$

and n is the number of atoms per unit volume. The constant in parentheses has the value 1.24×10^{11} j/deg^{4}sec^3, and sound velocities range from 10^5 to 10^6 cm/sec. In an isotropic medium the correct average sound velocity is $1/v_s^3 = 2/(3v_t^3) + 1/(3v_\ell^3)$, where v_t is the velocity of the shear waves and v_ℓ of the longitudinal.

Reproduced with permission of the copyright owner. Further reproduction prohibited without permission.

Table IX lists approximate values for heat capacities per unit volume at 1°K. These are included for perspective on the problems of bolometer manufacture. They are calculated from θ_D except for fused silica and sapphire.

In nonsuperconducting metals, electrons also have heat capacity. Kittel shows (p. 211) that their effective heat capacity is $C_{el} = (\pi^2/2)(Nk)(T/T_F)$, where N is the number of electrons involved, usually one per atom, and T_F is their Fermi temperature, which for copper is 82000K.

B. Bolometers Tested

In this Section I describe test results. Tables X, XI present data for a Golay cell, three InSb detectors, four germanium detectors, and a silicon detector. I will first describe the detectors, then the construction of the tabulated quantities, and then the implications of the results for our development effort.

1. Detectors

The Golay cell was obtained from Pye-Unicam. It has a vacuum-tube amplifier and a 3 mm diameter diamond window, protected by two layers of black polyethylene.

The InSb detectors were all operated in the same circuit, shown in Fig. 7. Detector 2 was given to us by Dr. Judy Pipher in 1970, and was made by the methods described by her in her thesis (1971). This is the detector described in greater detail in connection with the Fabry-Perot interferometer, Section II-B-8. It is operated behind a germanium condensing cone but is much larger than the output end of the cone, so that it is not as small and sensitive as it could be. Its NEP improves

Reproduced with permission of the copyright owner. Further reproduction prohibited without permission.

Table IX. Bolometer material heat capacities at 1°K.

Material	Mol. Wt	θ_D(K)	ρ(g/cm^3)	C (j/cm^3 deg)
In (Lattice)	115	111	7.28	9×10^{-5}
Ge	73	370	5.3	3×10^{-6}
SiO_2 (Fused)	60		2.2	1.8×10^{-6}
SiO_2 (Xtal)	60	470	2.2	6.9×10^{-7}
Si	28	640	2.33	6×10^{-7}
Al_2O_3	102	600	3.97	3.5×10^{-7}
TiO_2	80	760	4.26	2.4×10^{-7}
Fe_2O_3	160	660	5.24	2.2×10^{-7}
C (Diamond)	12	2230	3.52	5.2×10^{-8}

References: AIP Handbook, 3rd ed., p. 4-115 for θ_D.
For fused silica, sound velocities on p. 3-104 were used.
For Al_2O_3, see NBS Journal of Research 75A, p. 401 (1971).

Reproduced with permission of the copyright owner. Further reproduction prohibited without permission.

Reproduced with permission of the copyright owner. Further reproduction prohibited without permission.

Table XI. Detector efficiency estimates.

Detector, Conditions	System Efficiency	Approximate Transmissions					Effective Absorption
		Pipe	Window	Filter	Cone	Reflection	
1. Golay Cell	0.8	---	---	---	---	---	0.8
InSb Detectors							
2. Pipher's	0.1	0.8 (gaps)	---	0.7	0.7	0.6	0.4
3. Small Experimental	0.05	0.8	---	0.7	0.7?	0.6	0.2
4. Large Experimental	0.045	0.8	---	0.7	---	Cavity	0.08
Germanium Detectors							
5. Joyce's	0.045	0.5	0.5	---	---	Cavity	0.2
6. Lab Detectors	0.075	0.8	0.5	0.95	0.7?	Cavity	0.3
7. IR Labs F-42 4.2°	0.11	0.8	---	0.8	---	0.6	0.3
Metal Cone 1.5°	0.08	0.8	---	0.8	0.4	0.6	0.3
7'. Ditto, GeCone 4.2°	0.045	0.8	---	0.8	0.4	0.6	0.3
1.5°	0.026	0.8	---	0.8	0.4	0.6	0.2
8. IR Labs 228 4.2°	0.09	0.8	---	0.8	---	0.6	0.24
Metal Cone 1.5°	0.08	0.8	---	0.8	---	0.6	0.2
8'. Ditto, GeCone, 1.5°	0.056	0.8	---	0.8	0.7	0.6	0.2
8". Ditto, Antireflection, 1.50	0.074	0.8	---	0.8	0.7	---	0.17
9. Silicon Bolometer	0.06?	0.8	0.5	0.8	---	0.7	0.27?

Reproduced with permission of the copyright owner. Further reproduction prohibited without permission.

Table X. Detector test results.

Detector, Conditions	Responsivity V/W	Noise per $\sqrt{Hz}$	NEP$_e$ W/$\sqrt{Hz}$	P_{abs} 10^{-10} W/cm^{-1}	S/N	AΩ	Efficiency
1. Golay Cell, 13 Hz	8×10^5	40 μV	5×10^{-11}	4.5	10	0.05	0.8
InSb Detectors:*							
2. Pipher's, GeCone, 4.2°K, 300 Hz,	10^5	50 nV	5×10^{-13}	2.6	500	0.25	0.1
1200 Hz	10^5	15 nV	$1.5\ 10^{13}$	2.6	2000	0.25	0.1
3. Small Experimental, 4.2°K, 300 Hz	10^6	400 nV	4×10^{-13}	1	250	0.2	0.05
4. Large Experimental, 4.2°K, 300 Hz	5.5×10^4	100 nV	2×10^{-12}	1.6	80	0.35	0.045
Germanium Detectors:							
5. Joyce's Thesis, 1.1°K, 83Hz	8.7×10^4	20 nV	2.3×10^{-13}	1.2	500	0.25	0.045
6. Large Lab Detector, 1.3°K,	variable	---	2×10^{-13}?	1.2	500	0.15	0.075
7. IR Labs F-42 4.2°K	2×10^4	<10 nV	5×10^{-13}	0.7	150	0.06	0.11
Metal Cone, 17 Hz 1.5°K	6×10^5	30 nV	5×10^{-14}	0.5	1000	0.06	0.08
7'. Ditto, GeCone 4.2°K	2×10^4	<10 nV	5×10^{-13}	1.2	240	0.25	0.045
1.5°K	6×10^5	30 nV	5×10^{-14}	0.7	1400	0.25	0.026
8. IR Labs 228 4.2°K	2×10^4	<10 nV	5×10^{-13}	0.6	120	0.06	0.09
Metal Cone, 17 Hz 1.5°K	7×10^5	40 nV	6×10^{-14}	0.5	800	0.06	0.08
8'. Ditto, GeCone 1.5°K	7×10^5	40 nV	6×10^{-14}	1.5	2500	0.25	0.056
8". Ditto, Antireflection 1.5°K	7×10^5	40 nV	6×10^{-14}	2.0	3300	0.25	0.074
9. Silicon Bolometer 1.5°K	10^5?	40 nV?	4×10^{-3}?	1.2?	300?	0.2	0.06?

*InSb detectors include 1:50 stepup transformer.

a factor of 2 over the tabulated value when it is cooled to 1.6K.

Detectors number 3 and 4 were made from a graded boule of highly compensated InSb supplied to us by Caminco, Inc. Detector 3 was made from a high resistivity portion of the boule and has a DC resistance of about 15KΩ at 4.2°K. It is small, about 1/2 mm^3, just large enough to cover the end of a germanium condensing cone. A larger bar of InSb was cut from the boule with a wire saw and ground with abrasive on glass and paper. The bar was polished on a rotating paper wheel with a chemical polish of iodine dissolved in methanol. Two surfaces of the bar were tinned with indium solder using an ultrasonic soldering iron. Then the bar was diced with the wire saw to make a series of detectors.

Detector 4 was made in a similar fashion except that it is much larger, 5 mm×5 mm×1 mm. Its resistance at 4.2°K is about 1600Ω.

The germanium bolometers were obtained from two sources. Detectors 5 and 6 were made in this laboratory by R. R. Joyce. Number 5 is described in his thesis (1970) and number 6 is similar. Both are large with a volume of about 11 mm^3, and both are mounted in integrating cavities, with sapphire windows. They were made from material of high measured absorptivity.

Detectors 7 and 8 are bolometers number F-42 and number 228 from Infrared Laboratories. The former was loaned to us for development work with immersion optics, and the latter was purchased for use in the balloon-borne spectrometer. They are nearly identical. They are 0.8×0.8×0.3 mm in size, and are mounted with brass leads to sapphire heat sinks on a brass mounting plate. Each was tested at 4.2K and 1.5K bath

Reproduced with permission of the copyright owner. Further reproduction prohibited without permission.

temperatures, and each was used with a metal cone and a germanium condensing cone, to determine the gain of the germanium cone. Detector number 8 was also used with a Mylar antireflection coating on the front of the germanium condensing cone.

The silicon bolometer was purchased from Molectron, Inc. It is about 5 mm square and 0.3 mm thick, and is supplied with long gold leads. Because its leads are so long it is supported with nylon threads. It is positioned squarely across the end of a metal condensing cone, so that the integrating cavity behind it does not function fully. It was coated by the manufacturer with a thin layer of chromium to attempt to improve absorption. More recent experiments indicate that this film may have been simply a mirror. The film was on the back of the bolometer. This kind of bolometer is manufactured by diffusing phosphorus into a silicon surface. The surface is then etched away until the desired electrical properties are achieved.

2. Methods of Observation

Responsivities of the bolometers were determined from the I-V plots and the optically determined time constants, except for the Golay cell, which was calibrated by the manufacturer. Noises were measured with a lock-in amplifier (PAR HR-8) tuned to the chopping frequency. The output time constant was set to 1 sec, 6 db/oct, and the peak-to-peak noise was measured for about 1 minute. The noise in volts/$\sqrt{\text{Hz}}$ was found by multiplying this number by 0.4. Electrical NEP is the noise voltage divided by the responsivity at the chopping frequency.

Reproduced with permission of the copyright owner. Further reproduction prohibited without permission.

The column showing S/N ratio gives the ratio P_ν(abs)/NEP. This is the signal to noise ratio at 12 cm^{-1} for an unapodized spectrum made with 1 cm^{-1} nominal resolution (maximum path difference 1/2 cm) and 1 sec of total integration time. If the signal amplifying systems have not introduced excess noise, this signal to noise is actually seen on our spectra.

The powers incident on the detector are calculated from the black body formula, using the measured Michelson interferometer source brightness and an estimated $A\Omega$ product. The $A\Omega$ values for the Golay cell was measured as previously described. The $A\Omega$ values for the other detectors are all theoretical numbers, calculated from the geometrical sizes of the detectors. In the case of large detectors mounted in metal cavities the area of the coupling hole in the cavity is taken as the detector size. The cavity helps the detector to absorb the radiation and these detectors are therefore expected to be efficient. If the actual area of the detector chip were used the efficiency would appear much lower.

The column showing efficiency gives the ratio of calculated absorbed power to incident power. This is given for the detector system as a whole, including light pipes, windows, cold filters, condensing cones, and detector reflectance. The transmission factors are separately estimated and tabulated in Table XI. All the relevant factors are calculable from external evidence, either from measurement or theory, although most have not been individually verified for each system.

Detector reflectance is a major loss mechanism. At normal incidence on a dielectric, the reflectance is $(n - 1)^2/(n + 1)^2$, or

Reproduced with permission of the copyright owner. Further reproduction prohibited without permission.

0.36 for germanium. When the two polarizations are averaged, the reflectance is approximately constant with incidence angle out to the Brewster's angle, which for germanium is $\tan^{-1}(4) = 76°$. Between this angle and 90°, the mean reflectivity rises approximately linearly to 1. On this approximation, the solid angle average reflectance is 0.44 for Ge.

The efficiency of the immersion optics system is estimated from substitution experiments. A detector is first measured without the germanium condensing cone but with a metal cone instead. Then the germanium cone is installed. The gain which it produces is frequency dependent, due to imperfect optical contact between the cone and the bolometer. In the case of perfect contact to an opaque detector, the gain should be 16, which is the dielectric constant, times the ratio of areas illuminated, since the immersion optics illuminates only one of the six surfaces of the detector. The transmission across the gap between the two surfaces was calculated by David Woody from the electromagnetic wave equations with boundary conditions. It turns out that the surfaces must be very close together to avoid substantial losses, especially for rays which are far from normal to the surfaces. A graph of the results of these calculations is presented in Fig. 31. These results have been approximately averaged over all incidence angles.

The transmission across the gap can now be estimated from the frequency dependence of the gain of the cone. A fit to the observed spectrum tells us how far apart the two pieces of germanium are, and what the actual transmission across the gap is. With careful adjustment, it appears possible to bring the two surfaces together within a few

Reproduced with permission of the copyright owner. Further reproduction prohibited without permission.

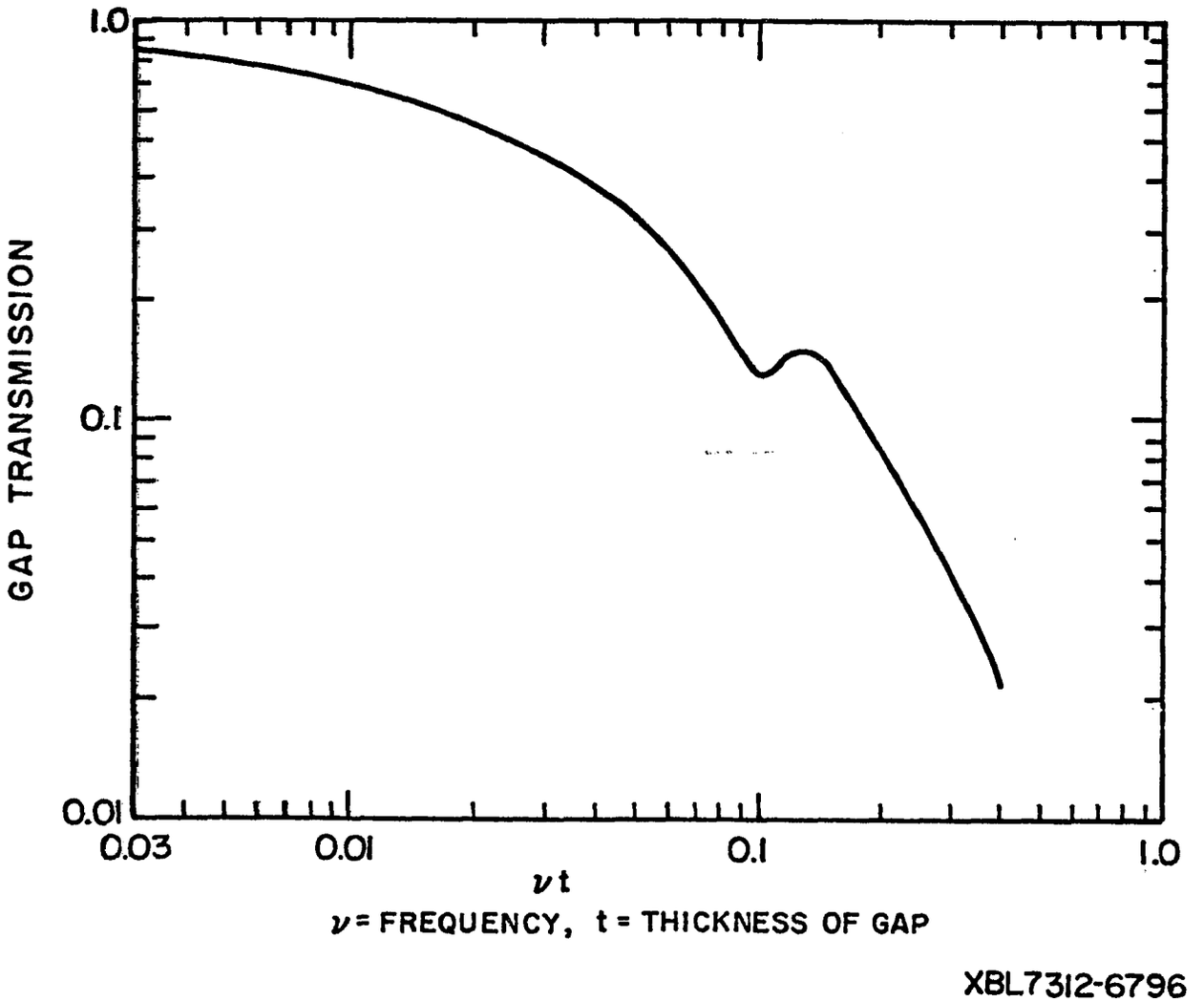

Fig. 31. Immersion optics efficiency.

Reproduced with permission of the copyright owner. Further reproduction prohibited without permission.

microns, and the transmission then exceeds 0.70.

3. Discussion of Results

a. Absorption. The bolometer absorptivity is of the greatest significance to our optimization of bolometers. Since it is determined as a residual after many corrections it is not expected to be very precise.

In most cases the absorption by the bolometer is expected to be near unity, if the design is correct. For example, R. R. Joyce built his bolometers of material known to absorb, and he put them in cavities to improve their absorption. The InSb bolometer given us by Pipher is also expected to be highly absorbing, especially at 4.2K. At the operating point, the DC resistance of the square bolometer is 250 ohms, smaller than the impedance of the vacuum. Free carrier absorption processes are then expected to give nearly complete absorption of millimeter radiation, at least at frequencies below the electron collision frequency.

In other cases the absorption is expected to be much smaller than unity, as in the case of the small InSb detector, which was made of material later measured to be nearly transparent. Moreover, its high DC resistance predicts low absorption by carriers.

Another very important case is the pair of bolometers from Infrared Laboratories. Their absorption depends strongly on bolometer temperature. At 12 cm^{-1}, the absorbed power falls by an order of magnitude when the detector chip is cooled from 2.2K to 1.5K. This is most important and unfortunate for us, since the best electrical sensitivity is obtained at the lowest temperatures. When the detectors are warmed up from

Reproduced with permission of the copyright owner. Further reproduction prohibited without permission.

2.2K to 5K, they absorb about 1.5 times as much radiation, but further heating produced by additional bias current causes no further increase. This holds true even at such high bias currents that the detector has a dc resistance of the order of 200 ohms. This resistance is so low that the electrons in the bolometer should absorb strongly at all frequencies. It is therefore surprising that the apparent absorption of these bolometers is only 0.3. Probably there is a loss mechanism elsewhere in the system, and the bolometer really does absorb.

None of the detectors except the Golay cell has an apparent absorptivity larger than 0.4. Some of the detectors should be much better than this. The only explanations apparent to me are geometrical optics effects. While all the detectors are different, each has at least one imperfection in its illumination system.

Detector 1, the Golay cell, has interference effects at low frequency. When tested with a klystron and harmonic generator at 5 cm^{-1}, it had a response as a function of angle which had a minimum on axis, where it was only half as sensitive as at other angles. Moreover, it has a large acceptance angle which has not been unambiguously measured, as previously described.

Detectors 2, 3, 7' and 8' all use germanium focusing cones. There are many ways in which we can miscalculate the transmission of the gap between cone and detector. For instance, if the detector or cone tip is not flat, then good contact is achieved in some areas and not in others. Spectral information is then deceptive. Another loss mechanism for these cones is the failure of total internal reflection on the walls of the cone. Rays within 14° of normal to the surface can

Reproduced with permission of the copyright owner. Further reproduction prohibited without permission.

escape the cone, but there should be few rays to which this applies.

Clues to these problems may be seen in Fig. 28. If there were perfect transmission across the gap, then the function $g(\theta)$ should be uniform out to $\theta = 18°$ and then fall abruptly to zero, according to the image-ball construction. What we see is that the response has fallen to 1/3 of its axial value at 18°, but more important, response extends all the way out to 45°. Indeed, 2/3 of the solid angle integral is outside 15°. This wide angle response is not understood, but is an obvious indication that our design is not working perfectly. Diffraction calculations similar to those described in Chapter III do not explain such a large response.

Detectors 4, 5, 6, 7, 8 and 9 all use metal condensing cones, leading either to a cavity or directly to the detector. The efficiencies of these cones have not been measured directly for the wide angle ray bundles which concern us. Moreover, some of them are too short to be ideal. We have not yet measured the solid angles appropriate to these systems.

Detectors 2, 5 and 6 are measured in systems containing sample holders or gaps in the light pipe. These losses are thought small but are not measured.

Detectors 7, 8 and 9 are mounted in such a way that their back surfaces are not fully illuminated. These corrections should also be small but are not directly known.

Detectors 4, 5, 6 and 9 are mounted in metal cavities. It is not known directly how effective these cavities are. Losses exist out the coupling hole, the vacuum tube and lead wire hole, and through

Reproduced with permission of the copyright owner. Further reproduction prohibited without permission.

absorption in the walls and in the varnish on the lead wires.

b. Noise. Our best detector is the germanium bolometer operated with a germanium condensing cone and an antireflection coating on the front surface of the cone. It is small, highly responsive, and has a moderate amount of noise. The next best detector is the InSb detector, operated at a chopping frequency greater than 1 kHz. This detector is the only one which is Johnson noise limited. All the others have noise considerably in excess of Johnson noise at the optimum chopping frequency. They are operated as resistors of about 1 megohm at a temperature of 2K, which produces a Johnson noise of only 10 nv/$\sqrt{\text{Hz}}$. These detectors appear to have spontaneous resistance fluctuations, which give rise to 1/f noise powers when D.C. bias is applied. These spontaneous resistance fluctuations are roughly proportional to the total resistance, so that the noise voltage produced is proportional to the D.C. bias voltage. While it has often been thought that this 1/f noise is due to contact barrier problems, John Clarke (personal communication, 1973) has suggested that it may be a bulk process, due to internal phonon noise in the detector. Different parts of the detector element exchange heat by the random walks of phonons, and spontaneous local temperature fluctuations exist. The conservation of energy implies that the mean temperature of an isolated detector chip cannot change due to these fluctuations. Therefore, to lowest order, the mean resistivity does not change, even in the presence of fluctuations. However, in our detectors, current distributions are nonuniform, so that the temperature fluctuations of some parts cause more change in net resistance than do other parts. In other words, we do not actually measure the mean

Reproduced with permission of the copyright owner. Further reproduction prohibited without permission.

resistivity of the detector chip. An internal spontaneous temperature fluctuation can therefore produce a first-order change in the observed resistance. A related effect is that due to temperature and doping gradients, the resistivity is non-uniform.

The implication of this idea for detectors is that to avoid excess noise, a bolometer should have a uniform volume current distribution and uniform doping. Consideration should also be given to the exchange of phonons between solder blobs used to attach leads and the detector element.

c. Blackening Films. Future improvements in bolometers for the far infrared probably lie with composite bolometers, with separate thermometers and radiation absorbers. Heat collectors can be made by blackening transparent dielectric materials with resistive films. The general properties of such films are described by Hadley and Dennison (1947), and many further references are given by Arams (1973). Films have been used for many years, in particular to blacken the heat absorber in the Golay cell.

Transmission line analogies are useful, especially for normal incidence radiation. In such a case, the transmission lines have impedance Z_o/n, where Z_o is the impedance of free space, 377 ohms, and n is the refractive index of the medium (assumed nonmagnetic). A conducting film of resistance R ohms/square is represented by a resistance R shunting the transmission line.

Our direct measurements of bolometer blackening were inconclusive. The Molectron silicon bolometer was coated by the manufacturer with chromium. Later measures with d.c. probes showed that these films

Reproduced with permission of the copyright owner. Further reproduction prohibited without permission.

were essentially short circuits. The films are very thin, of the order of 5 nm thick, and presumably form as islands of metal separated by gaps. Films made on glass slides under the same conditions had the desired resistances and were not mirrors. The discrepancy may lie in the different tunneling processes in glass and silicon, or perhaps the islands form differently on silicon.

Gary Hoffer has made and tested bismuth films for infrared transmission. He evaporated films from 25 nm to 400 nm thick on quartz, and measured d.c. and far infrared impedances. These impedances were comparable within a factor of 2, and no spectral variation was seen. The tests were made at liquid helium temperatures. These films are probably ideal for bolometer blackening.

Reproduced with permission of the copyright owner. Further reproduction prohibited without permission.

VI. CONCLUSIONS

The Cosmic Background Radiation is still poorly known in the millimeter wavelength region. Our first experiment helped dispel thoughts that there was substantial line emission superposed on the background. Our second experiment has not yet worked, but in developing our instrument we have advanced our understanding of the problems involved. We have discussed spectrometer design and operation, detector calibration and optimization, and antenna diffraction and emission. When minor problems with the instrument are repaired, we may be the first to measure the short wavelength spectrum of the Cosmic Background Radiation.

Reproduced with permission of the copyright owner. Further reproduction prohibited without permission.

ACKNOWLEDGEMENTS

I want to thank especially my thesis advisor, Prof. Paul L. Richards. His unflagging enthusiasm, faith, and clarity of mind have carried me through many discouraging moments. In his laboratory I learned experimental physics. With Dr. Michael W. Werner I shared the excitement, joys, and frustrations of learning a new field of physics, as we built the Fabry-Perot interferometer and made it work. His energy and determination were great. David P. Woody is my partner in building the balloon-borne spectrometer. His calm and patient approach, and his careful judgement in times of crisis, have often saved the day. He makes things work. And we both owe the greatest of thanks to J. Henry Primbsch, who designed the electronics for our balloon payload and made them work. His experience with ballooning, his expertise with electronics, and his generous nature made our experiment both possible and enjoyable. Richard Aurbach, Norman Nishioka, and Bryan Andrews have contributed their skill at computer programming. Gloria Pelatowski drew the figures and Jean Wolslegel typed the thesis, and they have been a comfort to me as they gave of their time and energy.

This work was done under the auspices of the Atomic Energy Commission. My fellowship was granted by the Fannie and John Hertz Foundation. Parts of this work were supported by NASA grants NGL 05-003-272, NGR 05-003-432 and NGL 05-003-497.

Reproduced with permission of the copyright owner. Further reproduction prohibited without permission.

REFERENCES

Arams, F. R., Infrared-to-Millimeter Wavelength Detectors (Artech House, Dedham, Massachusetts, 1973).

Beckman, J. E., Ade, P. A. R., Huizinga, J. S., Robson, E. I., Vickers, D. G., Harries, J. E., Nature 237, 154 (1972).

Beery, J. G., Martin, T. Z., Nolt, I. G., Wood, C. W., Nature Phys. Sci. 230, 36 (1971).

Bell, R. J., Introductory Fourier Transform Spectroscopy (Academic Press, 1972).

Blair, A. G., et al., Phys. Rev. Letts. 27, 1154 (1971).

Born, M. and Wolf, E., Principles of Optics (Pergamon Press, 1970).

Boyle, W. and Rodgers, K., J. Opt. Soc. Am. 49, 66 (1959).

Bracewell, R., The Fourier Transform and Its Applications (McGraw-Hill, 1965).

Brändli, G. and Sievers, A. J., Phys. Rev. B 5, 3550 (1972).

Burch, D. E., J. Opt. Soc. Am. 58, 1383 (1968).

Caroff, L. J. and Petrosian, V., Nature 231, 378 (1971).

Caroff, L. J., Petrosian, V and Werner, M. W., The Submillimeter Background Radiation, preprint, 1972.

Chantry, G. W., Submillimetre Spectroscopy (Academic Press, 1971).

Chelton, D. B. and Mann, D. B., Cryogenic Data Book, N. B. S., Boulder, Colo., May 16, 1956. Lawrence Berkeley Lab UCRL-3421.

Clarke, J. Hoffer, G. and Richards, P. L., Superconducting Tunnel Junction Bolometers, Lawrence Berkeley Laboratory Report 2222, 1973.

Reproduced with permission of the copyright owner. Further reproduction prohibited without permission.

Conklin, E. K., Nature 222, 971 (1969).

Connes, J., Computing Problems in Fourier Spectroscopy in Aspen Int. Conf. on Fourier Spectroscopy, 1970. See Vanasse, Stair and Baker, 1970.

Cowsik, R., Nature Phys. Sci. 239, 41 (1972).

Dalgarno, A. and McCray, R., Ann. Rev. of Astron. and Astrophys. 10, 375 (1972).

Dicke, R. H., Peebles, P. J. E., Roll, P. G. and Wilkinson, D. T., Ap. J. 142, 414 (1965).

Donnelly, R. J., Experimental Superfluidity (University of Chicago, 1967), p. 22.

Evans, N. J. Cheung, A. C., and Sloanaker, R. M., Ap. J. (Lett.) 159, L9 (1970).

Forman, M. L., Steel, W. H., Vanasse, G. A., J. Opt. Soc. Am. 56, 59 (1966).

Françon, M., Optical Interferometry (Academic Press, 1966).

Gamow, G, Phys. Rev. 74, 505 (1948).

Gebbie, H. A., Bohlander, G. W. and Pardue, G. W. F., Nature 230, 521 (1971).

Golay, M. J. E., Rev. Sci. Inst. 20, 816 (1949).

Grenier, P., Langlet, A., Talureau, B. and Coron, N., Applied Optics 12, 2863 (1973).

Hadley, L. N. and Dennison, D. M., J. Opt. Soc. Am. 37, 451 (1947).

Handbook of Military Infrared Technology, W. L. Wolfe, ed., ONR (G. P. O.) 1965.

Handbook of Physics, Condon and Odishaw, eds. (McGraw-Hill, 1967).

Harries, J. E., and Burroughs, W. J., Infrared Physics 10, 165 (1970).

Reproduced with permission of the copyright owner. Further reproduction prohibited without permission.

Harrison, E. R., and Kapitzky, J. E., A Theory of the Sub-Millimetre Background Radiation, 1972. Contribution No. 134 of the Five College Observatories, Univ. of Mass., Amherst, Mass.

Hegyi, D., Traub, W., Carleton, N., Phys. Rev. Lett. 28, 1541 (1972).

Henry, P. S., Nature 231, 516 (1971).

Houck, J. R. and Harwit, M. O., Ap. J. (Lett.) 157, L45 (1969).

Houck, J. R., Soifer, B. T. and Harwit, M., Ap. J. Lett. 178, L29 (1972).

Ipavich, F. M. and Lenchek, A. M., Phys. Rev. D 2, 266 (1970).

Jackson, J. D., Classical Electrodynamics (Wiley, 1962).

Jones, R. C., J. Opt. Soc. Am. 43, 1 (1953).

Joyce, R. R., Far Infrared Properties of Solids: I. Electronic Levels of d^1 Ions in Al_2O_3. II. Phonon Contribution to Electromagnetic Absorption in Lead (Ph. D. Thesis), UCRL-19666, August 1970.

Keller, J. B., J. Opt. Soc. Am. 52, 116 (1962).

Kittel, C., Introduction to Solid State Physics (Wiley, 1966).

Loewenstein, E. V. and Smith, D. R. , A. I. P. Handbook (McGraw-Hill, 1972), section 6r.

Low, F. J., Opt. Soc. Am. 51, 1300 (1961).

McClatchey, et al., AFCRL Atmospheric Absorption Line Parameters Compilation, AFCRL-TR-73-0096, Environmental Research Papers No. 434, National Technical Information Center.

McKellar, A., Publ. Dominion Astrophys. Observ., Victoria, B. C. 7, 251 (1941).

Martin, D. H., ed., Spectroscopic Techniques for Far Infrared, Submillimeter and Millimeter Waves (North-Holland Publ., Amsterdam, 1967).

Reproduced with permission of the copyright owner. Further reproduction prohibited without permission.

Martin, D. H. and Puplett, E., Infrared Phys. 10, 57 (1970).

Mather, J. C., Werner, M. W. and Richards, P. L., Ap. J. (Lett.) 170, L59 (1971).

Meeks, M. L. and Lilley, A. E., Geophys. Research 68, 1683 (1963).

Menzel, D. H., Fundamental Formulas of Physics (Dover Publications, 1960).

Mertz, L., Transformations in Optics (Wiley, N. Y., 1965).

Misner, C. W., Thorne, K. S. and Wheeler, J. A., Gravitation (W. H. Freeman, 1973).

Möller, K. D. and Rothschild, W. G., Far Infrared Spectroscopy (Wiley, 1971).

Muehlner, D. and Weiss, R., Phys. Rev. Lett. 24, 742 (1970).

Muehlner, D. and Weiss, R., Phys. Rev. D 7, 326 (January 1973).

Muehlner, D. and Weiss, R., Phys. Rev. Lett. 30, 757 (April 1973).

Nolt, L., Martin, J. Z., Wood, C. W. and Sinton, W. M., J. Atm. Sci. 28, 238 (1971).

Nolt, I. G., Radostitz, J. V. and Donnelly, R. J., Nature 236, 444 (1972).

O'Connor, J. T., Welch, W. J. and Tayeb, A. M., Berkeley Space Science Laboratory Internal Report, 1968.

Peebles, P. J. E., Physical Cosmology (Princeton University Press, 1971).

Penzias, A. A., Jefferts, K. B. and Wilson, R. W., Phys. Rev. Lett. 28, 772 (1972).

Phillips, P. G., Harwit, M. and Sloane, N. J. A., A New Multiplexing Spectrometer with Large Throughput in Aspen Int'l Conf. on Fourier Spectroscopy, 1970, Vanasse, Stair and Baker, eds.

Pipher, J., Rocket Submillimeter Observations of the Galaxy and Back-Ground (Ph. D. Thesis), Cornell University CRSR 461 (1971).

Reproduced with permission of the copyright owner. Further reproduction prohibited without permission.

Pipher, J. L., Houck, J. R., Jones, B. W. and Harwit, M., Nature 231, 375 (1971).

Pippard, A. B., Metallic Conduction at High Frequencies and Low Temperatures, in Advances in Electronics and Electron Physics L. Marton, ed. (Academic Press, 1954), Vol. 6.

Richards, P. L., J. Opt. Soc. Am. 54, 1474 (1964).

Robinson, L. C., Physical Principles of Far-Infrared Radiation (Academic Press, 1973).

Sakai, H., Vanasse, G. A., Forman, M. L., J. Opt. Soc. Am. 58, 84 (1968).

Sanderson, R. B., and Bell, E. E., Appl. Opt. 12, 266 (1973).

Sciama, D. W., Modern Cosmology (Cambridge University Press, 1971).

Setti, G. and Woltjer, J., Nature 227, 586 (1970).

Shivanandan, K., Houck, J. R. and Harwit, M. O., Phys. Rev. Lett. 21, 1460 (1968).

Smith, L. P., Mathematical Methods for Scientists and Engineers (Dover Publications, 1953).

Sommerfeld, A., Optics, (Academic Press, 1964).

Steel, W. H., Interferometry (Cambridge University Press, N. Y., 1967).

Thaddeus, P., Annual Review of Astron. and Astrophys. 10, 305 (1972).

Ulrich, R., Infrared Physics 7, 37 (1967).

Ulrich, R., Renk, K. R. and Genzel, L., IEEE Trans. on Microwave Theory and Techniques, M. I. T. 11, 363 (1963).

Vanasse, G. A., Stair, A. T., Jr. and Baker, D. J., eds., Aspen International Conference on Fourier Spectroscopy, 1970, AFCRL-71-0019, Special Report 114, National Technical Information Center.

Reproduced with permission of the copyright owner. Further reproduction prohibited without permission.

Viktorova, A. A. and Zhevakin, S. A., Sov. Phys.-Doklady 11, 1065 (1967).

Vystavkin, A. N., Gobenkov, A. N., Listvin, V. N. and Migulin, V. V. in Submillimeter Waves, Polytechnic Institute of Brooklyn Conference, Jerome Fox, ed. (Wiley-Interscience, 1971).

Wagoner, R. V., Nature 224, 481 (1969).

Walmsley, D. A., Clark, T. A. and Jennings, R. E., Appl. Opt. 11, 1148 (1972).

Williamson, K. D., Catlin, L. L., Romero, M. V., Blair, A. G., Heibert, R. D. and Loyd, E. G., Nature Phys. Sci. 241, 79 (1973).

Yamada, Y., Mitsuishi, A. and Yoshinaga, H., J. Opt. Soc. Am. 52, 17 (1962).

Reproduced with permission of the copyright owner. Further reproduction prohibited without permission.